May 2014

# The Rice Bay and Northeast Bay Gneiss Domes: a Kinematic Study of Competent Rock Bodies in the Rainy Lake Region of Ontario, Canada

Jane Block
*University of Wisconsin-Milwaukee*

# THE RICE BAY AND NORTHEAST BAY GNEISS DOMES: A KINEMATIC STUDY OF COMPETENT ROCK BODIES IN THE RAINY LAKE REGION OF ONTARIO, CANADA

by

Jane Block

A Thesis Submitted in

Partial Fulfillment of the

Requirements for the Degree of

Master of Science

in Geosciences

at

The University of Wisconsin-Milwaukee

May 2014

# ABSTRACT

THE RICE BAY AND NORTHEAST BAY GNEISS DOMES: A KINEMATIC STUDY OF COMPETENT ROCK BODIES IN THE RAINY LAKE REGION OF ONTARIO, CANADA

by

Jane Block

The University of Wisconsin-Milwaukee, 2014
Under the supervision of Dr. Dyanna Czeck

The Rice Bay and Northeast Bay gneiss domes (RBD and NEBD) are two tonalitic rock units located in the Archean Rainy Lake zone of the Superior Province. The Rainy Lake zone acts as a boundary between two subprovinces, accommodating transpression, significant shortening and dextral motion in its lithologic assemblage. This study contributes to understanding how deformation is partitioned in heterogeneous terranes, and also demonstrates a practical method of kinematic analysis. Foliations, lineations, shear zones, tension gashes, quartz veins, mafic enclaves, and folded and boudined veins were all utilized in the kinematic analysis. Foliation orientations in both domes are consistent with the overall foliation of the region, but the lineation orientations are less steeply plunging than most of the surrounding area. Shear zones in the RBD indicate shortening through sets of sinistral and dextral shears, while in the NEBD only dextral shear zones are observed. Strain analysis of mafic enclaves in the RBD indicate plane strain at lower magnitudes, while folded and boudined veins in the NEBD indicate slightly higher plane strain. Tension gashes related to late stage exhumation exhibit some sense of rotation, indicating that transpression was still occurring during the final stages

of deformation. Models of triclinic transpression with oblique simple shear and extrusion directions were fit to the lineation and strain data observed in both units. The shear obliquity angle is similar for both units (approximately 20° E) and the angle of extrusion is subvertical for both. The kinematic vorticity estimates differ between the two units indicating that the bulk rock in the RBD was accommodating mostly dextral shear whereas the bulk rock in the NEBD was accommodating mostly shortening. The set of triclinic models previously determined for the rest of the Rainy Lake area are similar, but the amount of partitioning between pure shear and simple shear and the extrusion angle differ in other rock units.

# TABLE OF CONTENTS

# LIST OF FIGURES

# LIST OF TABLES

# ACKNOWLEDGEMENTS

First and foremost, I would like to thank my advisor, Dr. Dyanna Czeck. Without her guidance and advice, this work would not have been possible. I owe a considerable amount of my success in completing my research and writing this manuscript to her.

I would also like to thank Dr. Barry Cameron for sharing his expertise in synthesizing geochemical data, and Dr. Adolph Yonkee for his help with the strain analysis. The advice and input of Dr. Julie Bowles on this manuscript has been greatly appreciated, as well. I also thank Dr. Fred Vollmer for providing the EllipseFit program used, and Dr. Carlos Fernández for providing the Excel spreadsheet used.

Without Leah Warder, the field work for this research would have been far less enjoyable, and I am grateful for her assistance and company in the field. Also, without my father, Marty Block's help, I would have been unable to navigate to island outcrops. I am very fortunate to have had such excellent help in the field.

Lastly, without the funding of the Society of Economic Geologists Canada Foundation, the Wisconsin Geological Society, and the University of Wisconsin-Milwaukee, this research would not have been possible. I deeply appreciate the support they have given me.

# Chapter 1: Introduction

In this thesis, a detailed structural analysis of rocks within two gneissic domes is presented. The purpose of the structural analysis is threefold: 1) to unravel the deformation history of these rock units in order to understand the regional tectonics and the structurally controlled distribution of gold and other resources, 2) to further our understanding of how deformation due to oblique plate collision is partitioned in lithologically diverse terranes, and 3) to provide an example of how detailed analysis of structures can be compared to results of mathematical modeling in order to constrain relatively complex deformation parameters.

## *1.1: Structural Analysis and Kinematics*

Structural analyses are essential for understanding the tectonic settings that actively play a role in shaping our world. Throughout time, geologic terranes composed of rock units with various lithologies have collided with each other and separated, creating wide assemblages of structures acting as evidence for past tectonic events. The end result of these tectonic movements is deformation or strain, a permanent change in the rock resulting in structures such as tectonic fabrics, shear zones, faults, folds, tension gashes, veins, and deformed features in rocks such as stretched pebbles or mafic enclaves. Through documentation of structures including detailed orientation measurements and strain estimations followed by careful analysis, the nature of ancient tectonic events can be unraveled and the processes by which rocks accommodate tectonic motions can be understood.

Kinematic analyses from orientation data allow structural geologists to obtain the deformational history of rock units (e.g. Fossen & Tikoff 1993; Druguet et al. 2008; Carreras et al. 2010). From varying types of field data, many aspects of deformation can be determined. On the regional scale, the style of tectonic motion can be determined. Styles of tectonic motion form in extensional and collisional settings, including transpression (oblique collision) and transtension (oblique extension). Transpression and transtension have varying degrees of pure shear versus simple shear that accommodate the shortening and the strike-slip respectively (e.g. Fossen & Tikoff 1993). Transpression and transtension also have the additional variables of extrusion angle relating to the pure shear and simple shear obliquity (Lin et al. 1999; Czeck & Hudleston 2003; Fernández & Díaz Azpiroz 2009; Fernández et al. 2013).

Fabrics and deformed objects within an outcrop can be used to interpret the kinematic history of a rock body and how the deformation was accommodated at a variety of scales. For example, orientations of lineation and foliation within specific units can constrain the style of motion (e.g. Fossen & Tikoff 1993; Czeck & Hudleston 2003; King et al. 2008). Foliations form perpendicular to the maximum shortening, while lineations indicate the orientation of maximum stretching (e.g. Fossen & Tikoff 1993), and can be used to constrain kinematic models, (e.g. Tikoff & Greene 1997; Sullivan & Law 2007) including the angles of extrusion and shear obliquity in transpression (King et al. 2008; Fernández et al. 2013). Strain markers such as mafic enclaves or pebbles in a metaconglomerate can also aid in determining if flattening or constriction is more prominent during deformation (Flinn 1965; Yonkee, 2005; Yonkee et al. 2013), and can be used in conjunction with foliation and lineation data to further constrain kinematic

models (Fernández et al. 2013). Deformation at the large scale is often partitioned into different domains (e.g. Goodwin & Williams 1996; Sullivan & Law 2007; Fernández et al. 2013). Shear zones are discrete localized areas of deformation, and sets of dextral (right lateral) and sinistral (left lateral) shear zones can indicate how deformation was partitioned within a unit (Carreras et al. 2010). Folded and boudined layers (indicating contraction and extension, respectively) are useful in constraining the directions of strain, and when used in conjunction with the lineation data, can be used in determining strain magnitudes (e.g. Druguet et al. 2008). Late stage quartz veins and tension gashes can be used to interpret stresses present during the final stages of deformation (e.g. Carreras et al. 2010).

*1.2: Study Area*

Deformation in the Rainy Lake Zone of the Superior Province in Ontario, Canada (Figure 1) took place during oblique plate collision. The geologic structures in this zone are dominated by shear zones on a variety of scales, ranging from microscopic systems to broad shear zone systems that can be traced over hundreds of kilometers. This region has a complex juxtaposition of geological units, and the style and orientation of shear zones and other deformation features differ substantially within various units.

The Rice Bay Dome (RBD) and Northeast Bay Domes (NEBD) are gneiss domes contained within the Rainy Lake Zone (Figure 2a; Figure 2b). They contain internal complex deformation features. The locations and orientations of much of the deformation (Druguet et al. 2008) and mineralization (Poulsen, 2000) in surrounding units may be

partially controlled by their presence. Both the RBD and NEBD are tonalites dated to 2.69 Ga (Davis et al. 1989) and were emplaced syntectonically (Poulsen 2000).
While recent work has illuminated many aspects of deformation within other units in the Rainy Lake Zone (Poulsen, 2000; Czeck et al. 2006; Druguet et al. 2008; Czeck et al. 2009; Carreras et al. 2010), these gneisses are relatively unstudied; no kinematic analysis has yet been done on the RBD or NEBD. Understanding the strain regime of the gneisses is important for understanding the deformation of the region. In particular, understanding deformation in the gneisses is also important to understanding the complex partitioning of deformation within the various units in the Rainy Lake Zone, evidenced in part by the weaker surrounding rocks (metagabbros and schists), which appear to have wrapped around the competent RBD and NEBD. This study also fills in a gap in the general knowledge of the area. The more accessible RBD will be studied in more detail and the nearby NEBD will be investigated to a lesser extent as time permits.

*1.3: Objectives and Goals of research*

This study has three main objectives. First, a structural map of features within the RBD and NEBD will be produced, as no such map has been produced in the past. This map will be the first of its kind for these two rock units and will be used to understand the spatial distribution of structures, which may be used to analyze the deformation partitioning and understand the distribution of commodities.

Second, a kinematic analysis will be performed to determine the deformational histories of the two gneiss domes, filling an important gap in the knowledge of deformation of the area. The kinematic analysis will then be compared to kinematic

models determined by studies in surrounding units. Currently, the accepted kinematic model is one of transpression, where both dextral motion and contraction are occurring simultaneously. However, the transpression is partitioned differently in the different units within the Rainy Lake Zone. Some units have relatively little deformation such as the Algoman plutons (Czeck et al. 2006), some have only localized deformation along discrete shear zones like the gabbroic units (Carreras et al. 2010), and others have pervasive deformation like the biotite schists (Druguet et al. 2008) and metaconglomerates (Czeck et al. 2009). Partitioning of different degrees of the contractional and dextral components of the transpression is also likely between units and even within units as evidenced by various estimates of vorticity (Druguet et al. 2008; Czeck et al. 2009). The kinematic analysis will be used to determine the partitioning of transpression within the RBD and NEBD. Understanding how strain is partitioned within the RBD and NEBD will add to the growing body of work on the deformation of the Rainy Lake zone. This research will add to the understanding of how strain partitions in broad zones with heterogeneous lithologies.

Lastly, I will look for an emplacement mechanism of the Rice Bay Dome. Emplacement mechanisms for gneiss domes are still controversial and unfortunately the studied units may be too deformed to accurately unravel emplacement fabrics. A likely culprit for emplacement of gneiss domes in this region is diapirism, as has been attributed in many Archean terranes (Figure 3a). Gneiss domes typically form the core of orogens and may or may not flow laterally to build orogenic plateaus (Whitney et al. 2004). Diapirism was long favored to be the main process forming domes, but has gone out of favor, particularly in younger (non Archean) domes, due to the lack of evidence for

syntectonic structural doming (Whitney et al. 2004). Instead of diapiric processes, it is suggested that some gneiss domes are emplaced through lateral flow and folding (Figure 3b). This method of emplacement would yield very different structures than pure vertical ascent. Horizontal fabrics would be present in domes emplaced by lateral flow. Flattening fabrics and evidence for extrusion during emplacement would also be visible. Rather than emplacement through exclusively one end member (be it vertical or lateral flow domination), many domes are likely emplaced through a combination of the two (Whitney et al. 2004).


**Figure 1:** The Superior Province. The Rainy Lake area is marked with a star. Modified from Marquis (2004).

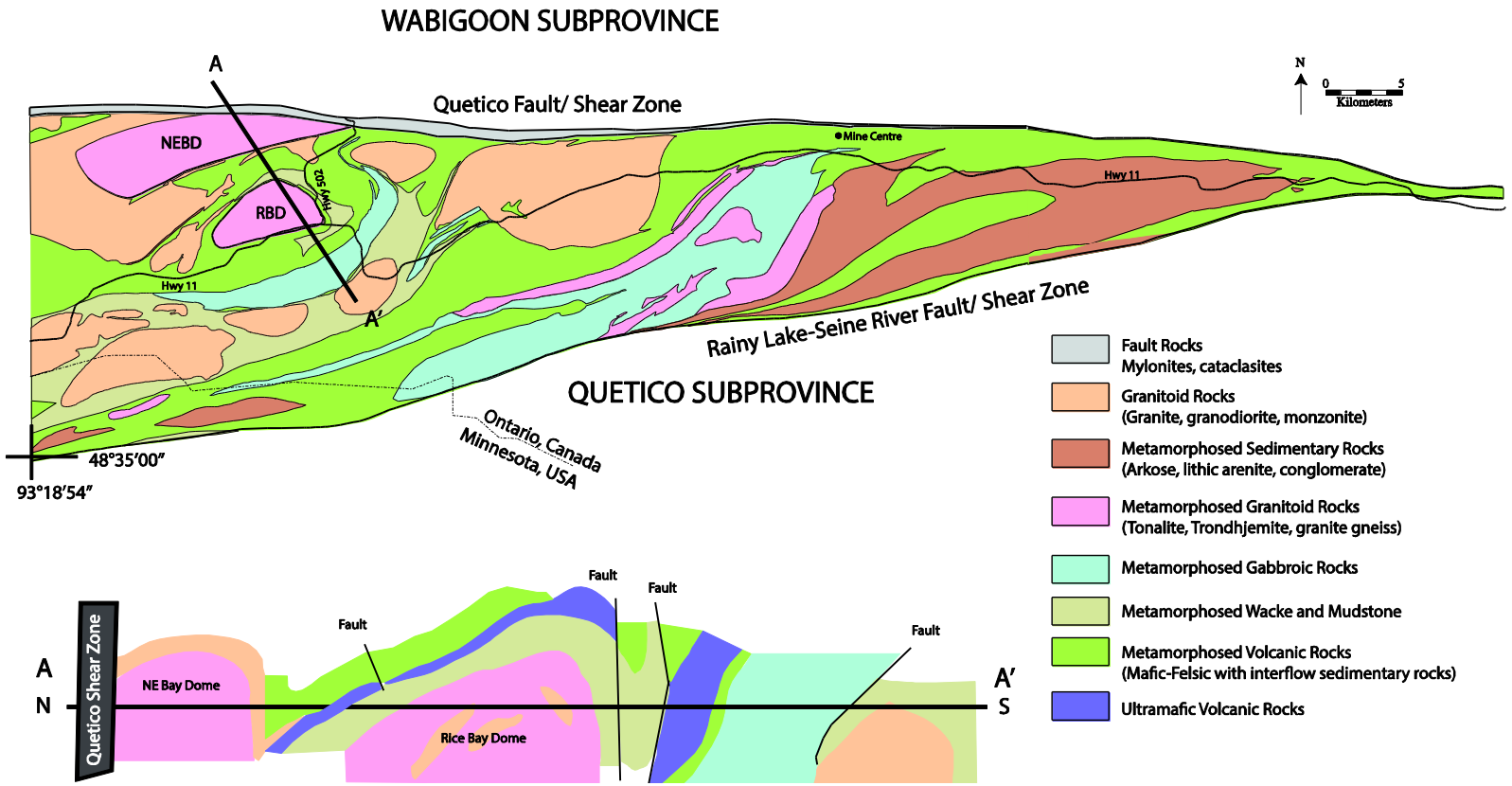


**Figure 2:** Map and cross section of study area.

**Figure 2a:** Geologic map of the Rainy Lake area. NEBD and RBD marked, along with approximate cross section line (A-A'). Green metavolcanic units include both mafic and ultramafic rocks. Image modified from Bauer et al. 2011, modified and combined from Wood et al. (1980a, 1980b), Stone et al. (1997a, 1997b), and Poulsen 2000.

**Figure 2b:** Cross-section of study area. Ultramafic metavolcanic units marked in purple and separated from the mafic metavolcanics. Modified from Davis et al. (1989).

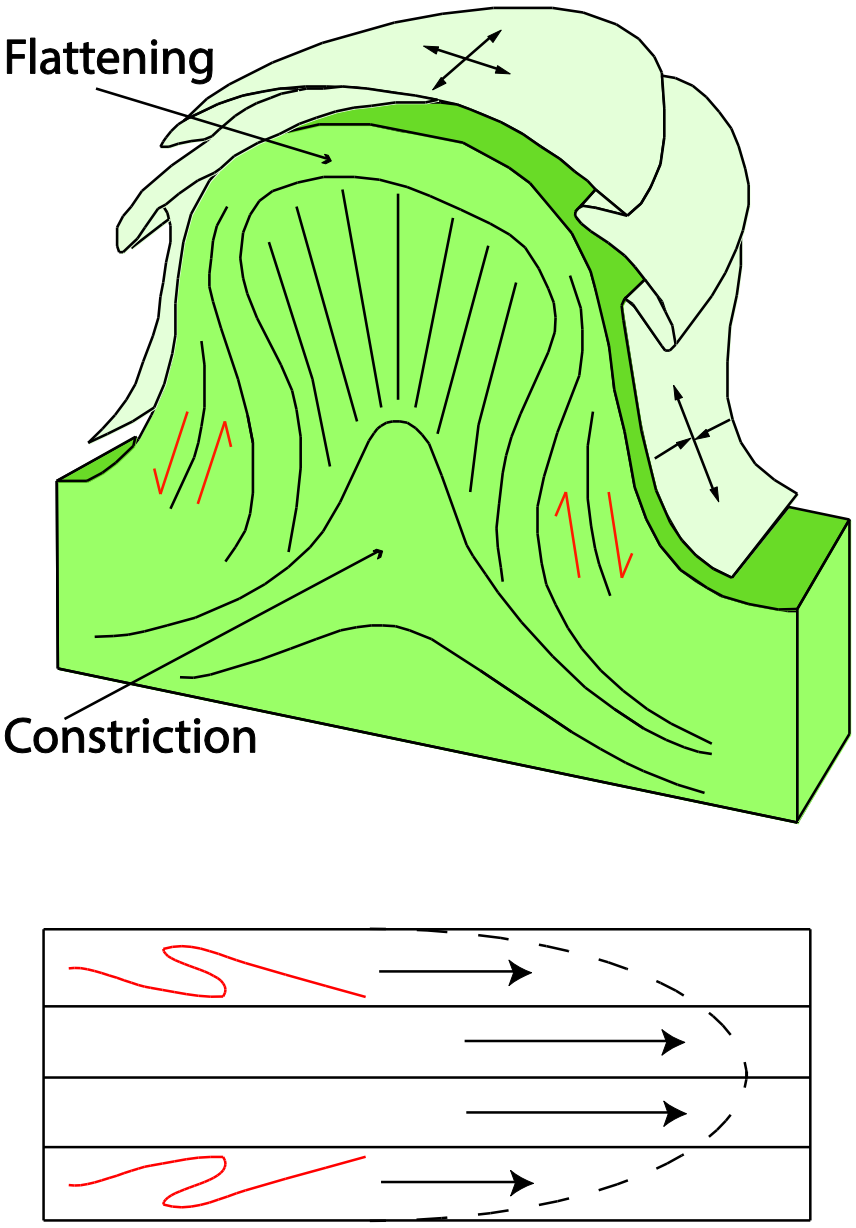


**Figure 3:** Structures associated with doming.

**Figure 3a (top):** Schematic drawing of diapiric ascent. Regions of flattening and constriction shown, along with differential movement within the dome. Mantling rocks shown in pale green; cascading folds and radial lineations common in diapiric domes. Image modified from Whitney et al. (2004).

**Figure 3b (bottom):** Schematic drawing of structures associated with channel flow. Horizontal flow fabrics present.

# Chapter 2: Background

## *2.1: Regional Geology*

The Rainy Lake region is located in the southern portion of the Superior Province in northwestern Ontario (Figure 1). The Superior Province is a large portion of the Canadian Shield composed of several different subprovinces of varying lithologies. The central subprovinces are composed of metasedimentary rocks (representing accretionary wedges) and others are metavolcanic (representing island arc terranes). The Rainy Lake zone is the boundary between metasedimentary Quetico and metavolcanic Wabigoon subprovinces. It is a wedge-shaped area bounded by two shear zones—the Quetico shear zone to the north and the Rainy Lake-Seine River shear zone to the south. The Rainy Lake zone does not belong to either the Wabigoon or the Quetico subprovinces; it is its own unique entity (Poulsen 2000).

The central part of the Superior Province was assembled into its current form during the Neo-Archean Kenoran Orogeny (~2.69-2.7 Ga) (Davis et al. 1989) and has not been tectonically active since. In the area that was to become the Rainy Lake zone, around 2.725-2.728 Ga, island arcs began forming, and continued subduction caused an accretionary prism to form around 2.7 Ga (Davis et al. 1989, Poulsen 2000). As subduction continued, island arc terranes (such as the Wabigoon and Wawa subprovinces) and sedimentary provinces, which were originally accretionary prisms caught between island arc margins (such as the Quetico subprovince), collided through oblique collision, or transpression (Poulsen 2000; Bauer et al. 2011). The Rainy Lake zone is a transitional

area between the Wabigoon and Quetico subprovinces, containing a mixture of lithologies from both the Quetico and Wabigoon subprovinces and other allochthonous rock units (Figure 2a).

Transpression resulted in many structures in the Rainy Lake zone including the large-scale bounding faults/shear zones, the Quetico to the north and the Rainy Lake-Seine River to the south (Poulsen 2000). Tonalitic plutons, such as the Rice Bay Dome and Northeast Bay Dome that are the focus of this study, were coeval with the main tectonic event, forming around 2.7 Ga (Davis et al. 1989, Poulsen 2000). After emplacement, the plutons deformed with continuing transpression becoming gneisses.

The oldest rock units in the area are metavolcanics of tholeiitic and calcalkaline composition, the Keewatin group. These rocks formed at approximately 2.728 Ga (Davis et al. 1989). Metagabbros are also present in the area, such as the Grassy Portage sill (Poulsen 2000). These metagabbros formed at approximately the same time as the Keewatin Group rocks (Davis et al. 1989). Tonalitic gneisses such as the Rice Bay Dome and Northeast Bay Dome (also referred to as Laurentian Plutons) were emplaced at approximately 2.725 Ga (Davis et al. 1989), making them also coeval to the Keewatin group and the metagabbros. Metasedimentary rocks, such as biotite schists, were once accretionary prisms forming from 2.704 Ga to 2.692 Ga. These rocks are also known as the Coutchiching Group (Davis et al. 1989, Poulsen, 2000). The Seine River Group is largely composed of a conglomerate slightly younger than the Coutchiching Group. These rocks were deposited from 2.976 – 2.686 Ga (Davis et al. 1989). Lastly, the relatively unmetamorphosed granitic Algoman Plutons were intruded into the area around

2.686 Ga during the final stages of deformation in the Rainy Lake area (Davis et al. 1989, Czeck et al. 2006, Druguet et al. 2008).

*2.2: Structural Geometry*

The two most prominent structural features of the Rainy Lake Zone are the Quetico and Rainy Lake-Seine River faults. The features have likely acted as both brittle faults and ductile shear zones during their Neoarchean history of movement. These faults truncate distinctive lithologic units at a low angle, indicating lateral movement (Poulsen 2000). Within the 1 km wide Quetico fault to the north, mylonites are common and a steep foliation parallel to the fault is present. Within the much smaller (50 m) wide Rainy Lake-Seine River fault, chlorite schists are present and contain enclaves of varying heterogeneous rocks. Both faults have a considerable, but immeasurable, amount of offset on the order of 100 km (Poulsen 2000). These two strike slip faults/shear zones bound the Rainy Lake Zone from the rest of the Superior Province, and overall have dextral senses of shear (Poulsen 2000). This sense of shear appears in all of the major shear zones in the region, including shear zones within the Rice Bay and Northeast Bay Domes (Poulsen 2000).

Foliations throughout the Rainy Lake zone strike generally E-NE, and dip moderately to steeply (Poulsen 2000; Czeck & Hudleston 2003). Lineations are generally variable in trend and plunge, with most observed lineations trending E-W and plunging moderately to steeply (with a few exceptions plunging shallowly) (Czeck & Hudleston 2003). Foliation fabrics dominate over lineation fabrics (S > L), indicating flattening strain was more prominent than constriction (Czeck & Hudleston 2003; Bauer

et al. 2011).

Smaller scale (mesoscopic) shear zones are prominent in several of the units in the Rainy Lake zone, particularly the metagabbros near the RBD and the tonalite-trondjehemite gneiss southwest of Mine Centre (Figure 2). Mesoscopic shear zones are also noted in the RBD and NEBD (Poulsen 2000). These shear zones vary in size from the cm scale to the m scale, and are of both shear senses. The shear zones fall into two distinct groups, one dextral with a general E-W strike, and the other sinistral with a NW-SE strike. These sets can be interpreted as conjugate shear zones and further confirm dextral wrenching of the faults (Poulsen 2000). Further analyses of shear zones in the RBD and NEBD are completed in this study.

Large folds within the Rainy Lake zone are identified by orientations and facing directions of mappable units (Poulsen 2000). These large early folds are recumbent and caused inverted stratigraphy (Poulsen 2000b), although they are difficult to fully identify due to subsequent deformation and metamorphism along with lack of stratigraphic markers in the now largely vertically oriented layering. Smaller upright folds locally fold the large features along ENE striking axial planes parallel to the regional foliation. These folds in the region are small, and are mainly found in schists, especially those surrounding the RBD and NEBD (Druguet et al. 2008). These folds in the schists are often difficult to pinpoint due to lack of prominent layering, and are most typically observed in leucocratic veins that intruded the schist (Druguet et al. 2008). These are interpreted as fold structures associated with the wrench zone due to their orientation (45°) with respect to the major faults, as demonstrated experimentally by Lowell in 1972

(Poulsen 2000). Late-stage crenulation cleavage that formed asymmetric folds is present in some schists as well, and these folds have a minor local effect on the largely vertical foliation (Poulsen 2000). Folds of both dextral and sinistral sense can be found, but the dextral folds outnumber the sinistral 2:1 (Poulsen 2000; Bauer et al. 2011).

*2.3: Deformational history*

The Rainy Lake zone underwent three major phases of deformation, each producing distinct structures. The first phase ($D_1$) of deformation consisted of faulting and recumbent folding of island arc rocks (metavolcanic rocks, metagabbros, and granitoid plutons including the Rice Bay Dome) and accretionary prism rocks (biotite schists). These folds were likely nappe-like (Davis et al. 1989; Poulsen 2000). Thrust faulting and vertical to sub-vertical strike-slip faulting may have also been active during $D_1$, resulting in stacking of geologic units and large scale fault offsets (Poulsen 2000; Poulsen 2000b; Czeck & Hudleston 2003; Czeck & Poulsen 2010; Bauer et al. 2011). During $D_1$, a regional schistosity subparallel to compositional banding in the units formed, which pervaded the whole region (Poulsen 2000; Druguet et al. 2008).

This schistosity is retained by the Rice Bay and Northeast Bay Domes (Poulsen 2000). This event also may have initiated the emplacement and doming of the Rice Bay area (Davis et al 1989; Poulsen 2000). The stratigraphy of the RBD area is overturned, and can be explained by a large scale nappe-like fold, which initially faced sideways and was progressively rotated and folded into a downward facing fold during later deformation (Poulsen 2000). The current map pattern could also be produced by faulting the RBD into the fold (Poulsen 2000), which would be consistent with a diapiric

emplacement (Whitney et al. 2004). The foliation found in the Rice Bay Dome (approximately EW striking) is attributed to this initial tectonic event (Poulsen 2000, Druguet et al. 2008). The foliation present in the NEBD is also attributed to this initial tectonic stage (Poulsen 2000).

$D_2$ is marked by a transition in deformation style to ductile transpression (as in Figure 5, discussed in *Section 2.4*), creating most of the S>L (foliation dominant over lineation) strong deformational fabrics that are pervasive throughout the region (Czeck & Hudleston 2003; Bauer et al. 2011). A composite schistosity of $D_1$ and $D_2$ fabrics formed during this stage, and lineations formed during this time plunge variably (Czeck & Hudleston 2003; Druguet et al. 2008). There are many lines of evidence supporting a transpressional model for the area, including the pervasiveness of dextral shear markers in the horizontal plane, widespread flattening fabrics, and subvertical foliations (Poulsen 2000; Czeck & Hudleston 2003; Bauer et al. 2011). However, the lineations observed in the Rainy Lake zone do not fit with the more basic model for homogenous monoclinic transpression (Sanderson & Marchini 1984; Fossen & Tikoff 1993). If this were the case, either vertical or horizontal lineations would be observed (Fossen & Tikoff 1993). In the Rainy Lake area, lineations are variable and plunge both east and west at nearly all angles (Czeck & Hudleston 2003; Fernández et al. 2013). Therefore, the model that best fits the field observations in the Rainy Lake zone is triclinic transpression with subhorizontal simple shear and a variable extrusion angle (Czeck & Hudleston 2003, Bauer et al. 2011, Fernández et al. 2013).

The ductile transpression is manifested differently in various geologic units,

characterized by homogenous deformation in the less competent units (metavolcanics and biotite schists) or concentrated deformation in the more competent units (metagabbros and gneisses) (Druguet et al. 2008, Bauer et al. 2011). It is also likely that certain lithologic units partitioned simple shear and pure shear differently to various degrees (Druguet et al., 2008, Bauer et al. 2011). Anastomosing shear zones formed during $D_2$ are a product of ductile wrenching, presumably with a high degree of simple shear (Czeck & Hudleston 2003, Bauer et al. 2011). Contemporaneously, greenschist-amphibolite facies metamorphism occurred, and more folds were formed during this second phase of deformation, ranging from tight to isoclinal (Poulsen 2000, Druguet et al. 2008). During $D_2$, the nappe-like folds created during $D_1$ were folded again, creating new folds with ENE striking axial planes parallel to the prominent $S_2$ foliation, including those on the flanks of the Rice Bay Dome (Davis et al. 1989, Poulsen 2000).

The metaconglomerates of the Seine Group may have been deposited in a pull apart style basin resulting from the dextral shearing of the Quetico and Rainy Lake-Seine River faults during this deformational phase (Davis et al. 1989, Czeck & Hudleston 2003, Czeck et al. 2009). Late stage intrusions of granites (the Algoman plutons) occurred late during $D_2$ (Czeck et al. 2006). These granitic plutons are compositionally distinct from the Rice Bay and Northeast Bay domes, which are tonalite-trondjhemite-granodiorite (Poulsen 2000).

Lastly, the area was exhumed and subjected to retrograde metamorphism ($D_3$) (Bauer et al. 2011). This last stage of deformation, involving all lithologies of the Rainy Lake zone, was likely controlled by the distribution of lithological units (Poulsen 2000).

During this phase, strain became localized along shear zones in the region, including the major mylonitized Quetico and Rainy Lake-Seine River faults and the NW-SE trending mesoscale shear zones (Bauer et al. 2011). Crenulation and kink bands also formed during this time, which locally altered the orientation of the $S_2$ foliation (Poulsen 2000). Late stage quartz and carbonate rich veins were also likely intruded into many units of the region (Bauer et al. 2011). $D_3$ deformation is more brittle-ductile than $D_2$ and represents rock exhumation (Bauer et al. 2011).

Metamorphic conditions in the Rainy Lake zone were low to medium grade, at a temperature of approximately 540° C and a pressure of 3.4 kilobars (Poulsen 2000). Rocks of the Rainy Lake region are mainly of greenschist and amphibolite facies. The distinguishing factor between the two is based on the abundances of key minerals. In the greenschist facies rocks, chlorite is abundant in all lithologies, carbonate minerals are found in the metabasites, sericite is found in the altered metavolcanics, and muscovite +/- biotite are found in the metapelites (Poulsen 2000). In the amphibolite facies rocks, garnet is relatively ubiquitous in the metapelites and amphiboles (hornblende and actinolite) are found in the metabasites. The amphibolite facies metavolcanics display retrograde assemblages as well (Poulsen 2000). Contact metamorphism is also present nearby the late Algoman plutons (Poulsen 2000). The RBD and the NEBD lie entirely within the amphibolite facies region of the Rainy Lake zone.

The most deformed units are those of the Keewatin and Coutchiching Group rocks, which were present throughout all phases of deformation, while the Algoman plutons are the least deformed, being late $D_2$ stage intrusions (Poulsen 2000). The

metatonalites of the Rice Bay and Northeast Bay domes display characteristics of amphibolite facies metamorphism, indicating a considerable amount of deformation, but are not as deformed as some of the less competent schists (Poulsen 2000).

*2.4: Transpression*

Most tectonic fabrics are not formed through one component of shear (be it pure or simple), but rather a combination of the two. This makes plane strain, where only one model of shear is operating or both pure shear and simple shear operate on the same plane, quite rare (Fernández et al. 2013). The amount of simple shear to pure shear can be represented by the kinematic vorticity number, $W_k$, which relates to the internal rotation of the deformation field. A $W_k$ value of 0 corresponds to exclusively pure shear, while a $W_k$ value of 1 corresponds to exclusively simple shear.

Transpression in its most basic definition refers simply to oblique collision (Harland 1971). Transpression has been utilized as a three-dimensional kinematic model useful for explaining a wide variety of flattening fabrics found in geologic settings (Sanderson & Marchini 1984; Fossen & Tikoff 1993). There are many different transpressional scenarios, from the simplest monoclinic transpression with simultaneous simple shearing and shortening in the same plane with vertical extrusion (Sanderson & Marchini 1984; Fossen & Tikoff 1993), to a more complicated triclinic transpression with oblique simple (Lin et al. 1999) and pure shear components (Figure 4) (Czeck & Hudleston 2003; Fernández & Díaz-Azpiroz 2009; Fernández et al. 2013). When considering possible transpressional models, the lineation orientation is a key deciding factor. Monoclinic models predict lineations that are either horizontal or vertical

(dependent on which type of shear is dominant and how much strain has accumulated) (Fossen & Tikoff 1993). However, in triclinic scenarios, lineations will plunge obliquely, indicating a component of shear obliquity (Lin et al. 1999; Fernández & Díaz-Azpiroz 2009; Fernández et al. 2013) and/or inclined extrusion (Czeck & Hudleston 2003; Fernández & Díaz-Azpiroz 2009; Fernández et al. 2013).

In the Rainy Lake zone, obliquely plunging lineations are ubiquitous throughout all units (Czeck & Hudleston 2003). This indicates that the Rainy Lake area underwent a more complicated form of transpression than the basic monoclinic case. Czeck & Hudleston (2003) concluded that the observed lineations in the Rainy Lake area do not fit the case of triclinic transpression with an inclined shear plane, and require an additional component to explain the lineation patterns observed. Adding a component of oblique extrusion (in variable orientations) mostly fits the observed field data (Fernández et al. 2013). In this study, the field data are tested against this generalized transpression model where the obliquity of the simple shear component and the angle of extrusion, along with $W_k$ and strain magnitudes, are considered variables following the method of Fernández et al. (2013).

*2.5: Gneiss domes*

Gneiss domes appear in orogenies all over the globe, during all time periods (Whitney et al. 2004). Gneiss domes have been documented in recent orogenies, such as the Himalayas, as well as ancient orogenies, such as those in South Africa (e.g. Gerya et al. 2004). Typically, gneiss domes are structural domes (plunging anticlines in both directions on the surface) with migmatite and orthogneiss cores. Many domes in the

world also have a mantling of metavolcanic or metasedimentary rocks (Whitney et al. 2004). Gneiss lithologies often record a higher amount of strain than the surrounding metavolcanics or metasedimentary rocks (Whitney et al. 2004).

The origin of gneiss domes is still debated by geoscientists (Whitney et al. 2004). Initially, all gneiss domes were thought to have formed through diapirism, or a part of the lower crust "bubbling" up into the upper crust. However, in more recent years, there has been a shift in accepted formation to that of crustal flow, with varying vertical components, from pure lateral flow to pure vertical flow. The structures present in gneiss domes vary depending on the direction of crustal flow (Figure 3a, 3b) (Whitney et al. 2004). Diapirism is thought to be more common in Precambrian terranes, due to the nature of tectonics at the time and the elevated mantle temperature (Whitney et al. 2004; Chardon et al. 2009). Radial lineations and specific finite strain patterns of flattening and constriction at specific localities are excellent indicators of diapiric flow (Figure 3a) (Whitney et al. 2004).

*2.6: The Rice Bay Dome*

The Rice Bay Dome is a gneissic body with a tonalitic composition approximately 3.5 km by 5 km in lateral extent. It outcrops along the Trans-Canada Highway (Hwy 11), approximately 10.5 km north of the United States border, as well as along abandoned logging roads and island outcrops in Rice Bay of Rainy Lake (Figure 5b, 5c). Outcrop size varies from small (about 9 $m^2$ along the logging roads) to large (sprawling and extensive outcrops, such as those along Hwy 11). Low-lying areas of the islands in Rice Bay exposed significant rock surface as well, as the lake level had recently dropped

during the year of this study (2013) (Figure 5a).

The RBD consists of three rock types: quartz/plagioclase/mica schists and gneisses, quartz-poor mafic schists and gneisses, and dikes and sills consisting of metamorphosed quartz/feldspar porphyry (Poulsen 2000). Quartzofeldspathic gneisses are the dominant lithology in the Rice Bay Dome, with internal veins of various composition (quartz and K-feldspar, mainly) being common. While the Rice Bay Dome has been classified as both a paragneiss (shale protolith) and an orthogneiss (igneous protolith) in the past, it is generally accepted that the orthogneiss interpretation is correct for at least the majority of the unit, and the protolith for this unit is an intrusive igneous rock, although parts may be derived from a felsic volcanic protolith (Poulsen 2000).

The RBD and its nearest neighbors, the metavolcanics and metasedimentary schists, were likely folded into their present configuration during $D_1$ and $D_2$. The units were first folded into nappe-like structures ($D_1$), and then folded and rotated again into an inverted antiformal structure ($D_2$) (Poulsen 2000). $D_2$ folds are largely restricted to the units flanking the RBD and are not prominent within the dome itself.

Foliation fabrics are strong throughout the RBD (Figure 5d), and weak lineation fabrics are present as well. Foliation planes dip away from the center of the dome, and are moderately to steeply dipping. Lineations are not well constrained, and have no preferred orientation. The Rice Bay Dome exhibits several internal structures, including shear zones, folds, boudins, tension gashes, mafic enclaves, and veins. Shear zones and folds are more prevalent in the center portion of the dome, while mafic enclaves are only found in the outer rim. Quartz veins and tension gashes outcrop in all areas of the dome.

Most folds and shear zones indicate approximately east-west dextral motion on the subhorizontal plane, but sinistral shear zones also exist. A detailed study of shear zones with the RBD is undertaken in this study. Internal folds are not as abundant, but where present, are generally tight and asymmetrical. Most folds were not visible in 3D.

*2.7: The Northeast Bay Dome*

The Northeast Bay Dome is also a tonalite body emplaced at the same time as the Rice Bay Dome. This dome is laterally more oblong in shape (approximately 14.5 km long and 4 km wide) than the neighboring Rice Bay Dome, which lies approximately 5.25 km to the southeast (Poulsen 2000) (Figure 2). Access to this dome was limited, as the area had been logged in recent years and the forest had overgrown much of the previously exposed gneiss. Outcrops in the NEBD were fairly large in size (15 m long), and consisted of many pavement surfaces created due to erosion from Pleistocene glaciation. Much of this area had been reforested since its last logging, resulting in relatively few extensive outcrops.

The NEBD also contains strong foliation fabrics and weaker (but present) lineation fabrics, shear zones, folds, and boudins. Foliation in the NEBD generally trends east-west and is moderately to steeply dipping. Unlike within the RBD, the NEBD contains almost exclusively dextral shear markers—all shear zones and folds display dextral motion. Internal folds are tight and asymmetrical as well. All structures appear to be distributed evenly throughout the unit (Figure 5e). The NEBD was likely significantly impacted by the Quetico shear zone (Poulsen 2000).

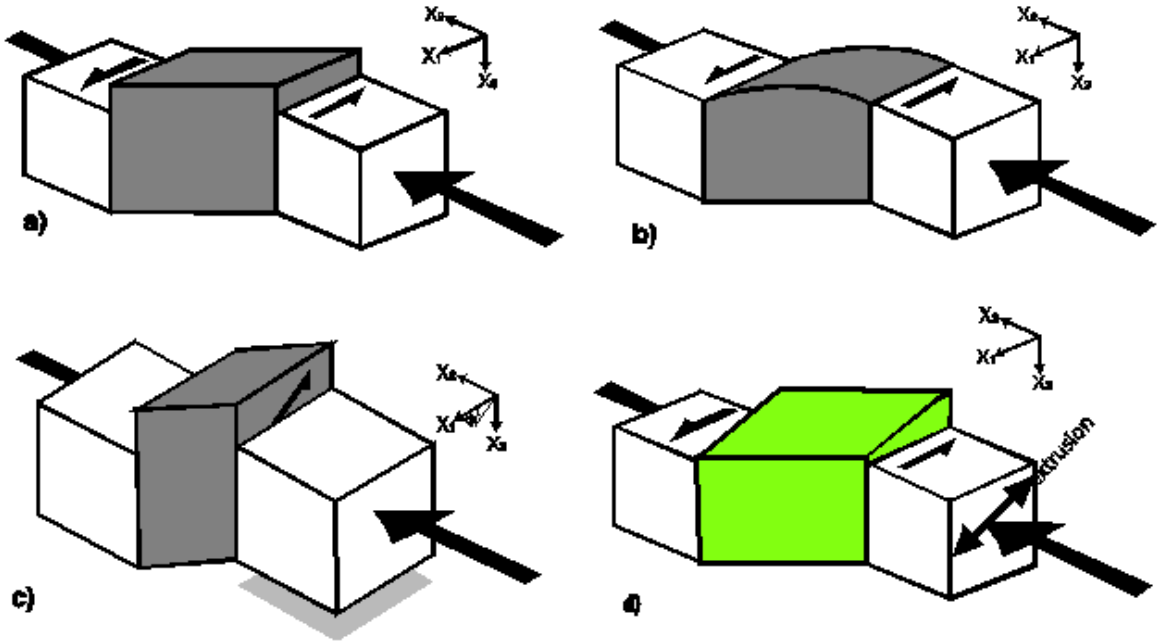


**Figure 4:** Examples of transpression where $X_1$, $X_2$, $X_3$ are coordinate axes of reference frame with $X_1$ parallel to the strike of the shear zone boundary, $X_2$ normal to the boundary, and $X_3$ is vertical (modified from Bauer et al. 2011). (a) Classical model of monoclinic transpression from Sanderson & Marchini (1984) and Fossen & Tikoff (1993). (b) Model of Robin and Cruden (1994) and Dutton (1997) with no-slip boundaries. (c) Model of triclinic transpression of Lin et al. (1998) with oblique simple shear component. φ is the angle between the simple shear component and the strike of the shear zone boundary. (d) Model of triclinic transpression with inclined extrusion direction from Czeck & Hudleston (2003). A combination of cases (c) and (d) is most appropriate for the Rainy Lake area where the angle φ is between 0-20° and the extrusion angle varies (Fernández & Díaz-Azpiroz 2009; Fernández et al. 2013).

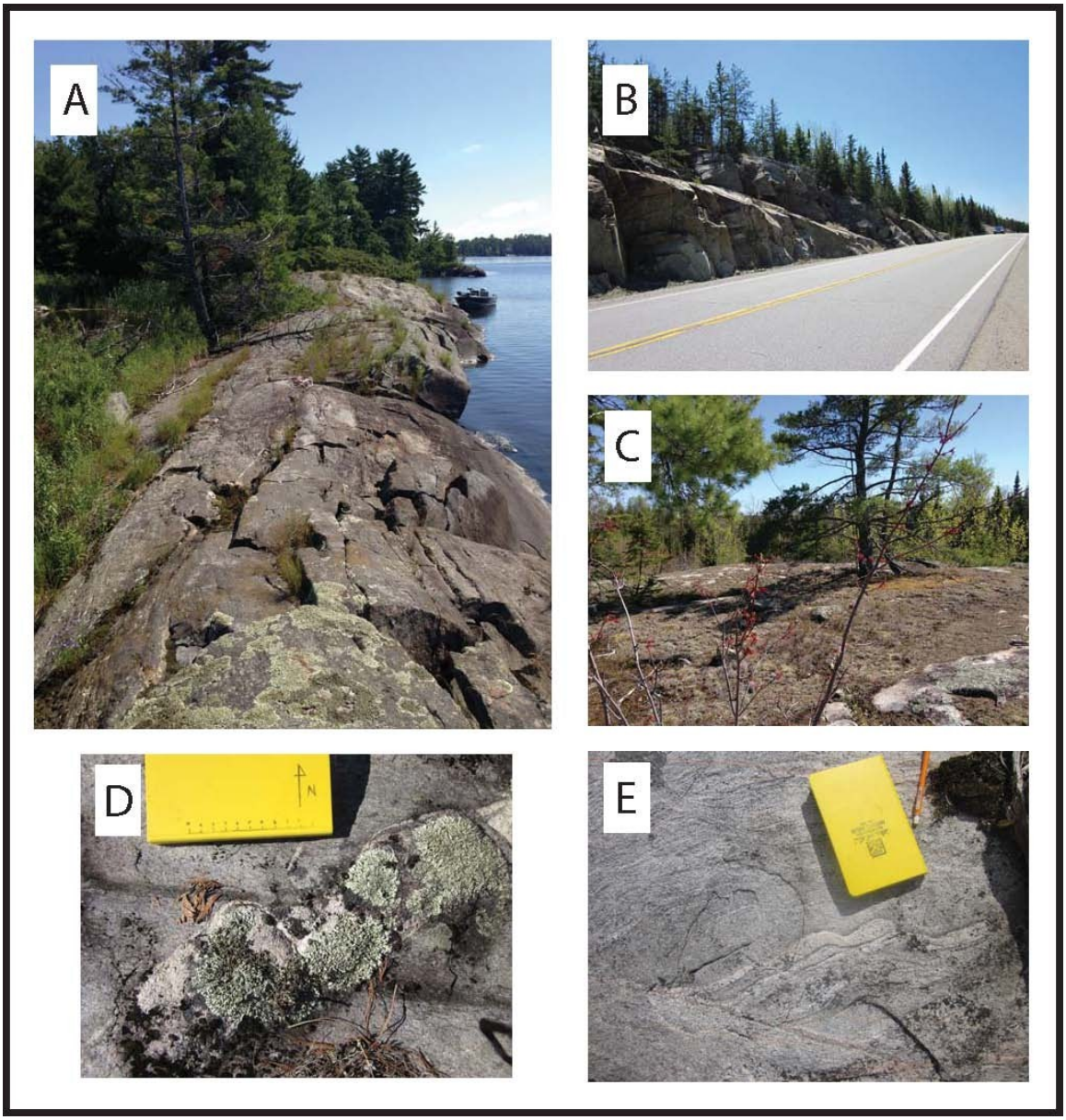


**Figure 5:** Rainy Lake images.
A: Typical island outcrop displaying lowered lake level.

B: Outcrop along Highway 11. Outcrop extends for a significant distance.

C: Typical outcrop along logging roads. Note prevalence of cover.

D: Foliation in the Rice Bay Dome. View is taken facing northwest. Foliations are dipping moderately to the right (north).

E: Foliation in the Northeast Bay Dome. View is taken facing down on subhorizontal plane. Foliations are striking from left-right across the photo.

# Chapter 3: Methods

## *3.1: Field Work*

Field work was carried out in May and July of 2013. In May, data were collected from all land-based outcrops in the RBD and NEBD, while in July island outcrops were visited by boat. A Garmin GPSMap 76S was used to pinpoint locations of outcrops for revisiting and data analysis. Samples from outcrops were also taken for later geochemical analysis.

### *3.1a: Foliations*

Foliation planes were measured with a Brunton compass. These planes were easily distinguishable, even in the heavily glaciated pavement outcrops, as biotite is the main foliation forming mineral, and biotite grains stood in marked contrast to the rest of the lighter colored minerals in the rock (Figures 5d, 5e, 6b). Strike and dip of foliation planes were measured.

### *3.1b: Lineations*

Lineation fabrics were much weaker than foliation fabrics. Due to the glaciated nature of the terrain, many outcrops were often subhorizontal exposures only, so steep foliation surfaces were not regularly exposed and therefore lineations could not be observed. On exposed foliation planes, lineations were defined by alignment of elongated minerals. When present, a pencil was held in the same orientation of the elongate mineral, and trend and plunge was measured.

### *3.1c: Shear Zones*

Small-scale (<10 cm width) shear zones were present throughout both domes and identifiable by offset and deflected foliation traces (Figure 6a). When exposed, strike and dip of each shear zone were measured with the Brunton. However, as the area had undergone extensive glacial weathering, many shear zones were found on two-dimensional pavement outcrops. In this situation, a strike of the shear zone was taken by aligning the Brunton with a notebook on the shear zone plane, but dip could not be recorded.

One outcrop in the central area of the RBD displayed a large quantity of anastomosing small-scale shear zone sets, and was utilized for a detailed strain analysis. This outcrop was on a large (2 m by 5 m) two-dimensional pavement surface. A clear, thin plastic painter's tarp was overlain on the outcrop and the shear zones and their relationships were traced as they appeared in the field. All features of this outcrop were noted on the plastic, including the strike, dip, and shear sense of the shear zones, foliation traces, tension gashes, and places where significant quartz had filled the shear zones.

*3.1d: Tension Gashes*

Tension gashes were defined for this study as filled cracks of which both ends were visible (Figure 6a). These tension gashes are late stage intrusions that record the final stress field present. Tension gashes in both the RBD and NEBD vary in fill (quartz, K-feldspar, and an iron-rich quartz fill). When possible, both strike and dip of the tension gashes were collected with the Brunton, but in most cases, only the strike of the tension gash could be collected, using the same method as the shear zones in section 3.1c. The type of fill was also recorded.

*3.1e: Quartz Veins*

Many late-stage quartz veins are present in the RBD, but absent within the NEBD. In contrast to the tension gashes, quartz veins were defined by planar quartz features where no end to the vein was visible—the plane appeared to be continuous. Strikes and dips of these veins were measured with the Brunton. Quartz veins were predominantly located towards the outer rim of the dome.

*3.1f: Folded and Boudined Veins and Dikes*

Folded and boudined veins and dikes were present in both the RBD and NEBD, but were more extensive in the NEBD. Folded and boudined dikes in the NEBD and RBD were granitic and otherwise leucocratic in composition. Some folded and boudined veins on the margin of the RBD were quartz veins, however. Initial and final lengths of the folded and boudined features were measured with a rope that was measured (for initial) and tape measure (for final) for the purpose of strain estimation (Figure 6c). Strike of the vein envelope was measured. Strike and dip of the surface containing the fold or boudin was also measured, although most measurements were taken from the subhorizontal plane.

*3.1g: Mafic Enclaves*

Mafic enclaves are the result of incomplete magma mixing. Xenoliths are small, elongate remnants of the nearby country rock incorporated into the dome during emplacement. In the case of the RBD, it is not known whether the features seen are enclaves or xenoliths, so are referred to generically as enclaves here (Figure 6b). Mafic enclaves were only found in the RBD on surfaces along the outer rim. The shape and

orientation of the enclaves were measured for strain analysis. Ideally, in order to best fit a three-dimensional ellipsoid from two-dimensional data taken from multiple planes, enclaves would be measured on three mutually perpendicular surfaces; however, due to natural outcrop shapes, surfaces oriented at high angles to each other were the best choice, and reasonable ellipsoid fitting could be conducted (e.g. Owens 1984). The strike and dip of the plane containing the mafic enclaves was recorded. Next, the rake of the long axis of each enclave was measured using a protractor. The maximum length and minimum width of the enclave were measured, using a visual approximation of an ellipse. Some surfaces contained up to 50 enclaves, while some only yielded 5.

### *3.2: Data Analysis*

GPS locations of outcrops were entered into a KML file for Google Earth. The resultant image was exported for use in Adobe Illustrator, and overlain with the relevant portions (RBD and NEBD) of the map from Poulsen 2000. To create the base layer of the structural maps, the Poulsen 2000 map was traced and the stations from the Google Earth image were placed on the tracing (Figure 7).

#### *3.2a: Foliations*

Foliations were plotted on equal area stereonets using Rick Allmendinger's Stereonet 8 program. Foliation measurements were plotted on the Adobe Illustrator tracing of the RBD and NEBD maps. Plotting each foliation plane on the map is useful in visualizing the overall structure of the domes.

#### *3.2b: Lineations*

Lineation data were also plotted on equal area stereonets using Stereonet 8. Each

lineation was plotted on a stereonet with its accompanying foliation measurement and placed on the map.

*3.2c: Shear Zones*

Shear zones with dip data were plotted in Stereonet 8 on equal area stereonets. For shear zones with only strike data, Matty Mookerjee's Rose diagram program (from Geological Programs for Mathematica) was used. Stereonets were plotted for shear zones by both shear sense and station.

The detailed tracing of the anastomosing shear zone network from the center of the dome (RBD 13-07) was digitized in Adobe Illustrator. Shear zone traces, foliation traces, strike and dip measurements of both shear zones and foliations, and prominent quartz veins were all noted on the traced image. Outcrop photographs were stitched together in Adobe Photoshop to fully show the relationships between shear zone strands.

Networks of shear zones often form with progressive deformation. As deformation continues, the many smaller shear zone strands form (Mitra 1979). The relationships between shear zones can be used to determine the strain history of the network, as wider shear zones are typically considered to be older (Mitra 1979) and deflections of foliations at shear zone intersections, along with cross-cutting relationships can be used to determine relative age of shear zone strands (Carreras et al. 2010). At this outcrop, foliations at confluences of shear zones were indiscernible in most places. Also, there was a considerable amount of merging of separate shear zones into one, further complicating determining relative timing (Carreras et al. 2010).

*3.2d: Tension Gashes*

As most tension gashes in the study area could only yield strike data due to the limited two-dimensional exposure, strikes of tension gashes were plotted in the Rose Diagram program. Tension gashes were plotted according to station and by type (quartz fill, K-feldspar fill, or Fe-rich fill). Tension gashes typically open in the direction of the least compressive stress ($\sigma_3$) and can be used to approximate stress orientations within the dome (e.g. Saintot et al. 2003). Because the deformation may have had a rotational component, orientation will not be preserved for the tension gashes that form early in the deformation so care needs to be taken when interpreting the stress data.

*3.2e: Quartz Veins*

Strike and dip of quartz veins were plotted using Stereonet 8. These veins appear largely undeformed, not folded or boudined, and are likely late-stage features that can be used to interpret final stress regimes in the dome, allowing for a paleostress analysis. The vein envelope was considered to be perpendicular to $\sigma_3$ (e.g. Saintot et al. 2003).

*3.2f: Folded and Boudined Veins and Dikes*

Folded and boudined dikes and veins were analyzed with the EllipseFit program by Fred Vollmer in order to determine the best fit two-dimensional finite strain on a horizontal surface. For stations with more than four features with folds and/or boudins present, initial and final lengths of the folds were entered, along with the strike of the dike or vein enveloping surface. From folds and boudins, a general shape of the 2D strain ellipse can be calculated. Boudins indicate extension and folds indicate contraction, and the stretch (final length/ initial length) can be calculated for each. When many

extended and contracted lines on a surface are combined together, the best fit two-dimensional finite strain ellipse can be calculated with maximum stretch direction, $S_1$, and minimum stretch direction, $S_3$ (Talbot 1970; Druguet et al. 2008). From the 2D strain ellipses output by the EllipseFit program, 3D strains were interpreted following the methods of Druguet et al. (2008). The EllipseFit program provides the ratio of the long/short axes, but not the actual stretch calculations for the axes. As a check on the program and a way to determine the actual stretch values at the axes, stretch magnitudes ($l_f / l_o$) from the veins were plotted by hand and the angle of maximum elongation (φ) was plotted along with the minimum elongation direction which is 90° away from φ. The EllipseFit programs were then digitally scaled in Adobe Illustrator to match the stretch magnitudes of the hand-drafted ellipses, and stretch values were obtained for the axes.

To find the best three-dimensional ellipsoid, constant volume during deformation is assumed (the magnitude of axes of the strain ellipsoid multiply to 1; $X \times Y \times Z = 1$, using terminology that principal axes X>Y>Z), allowing for an estimation of the 3D strain ellipsoid from 2D sections (Druguet et al. 2008). This assumption is acceptable, because while there is some evidence for fluid movement during emplacement of the folded and boudined veins (quartz veins in the necks of tension gashes), there is no evidence for a significant fluid transport component of deformation in the bulk rock. We also assume that the subhorizontal two-dimensional surface that folded and boudined veins are contained on contains one of the principal planes (X and Z or Y and Z, depending on lineation orientation). If lineations are horizontal, then X and Z are contained on the outcrop surface; if lineations are vertical, then Y and Z are contained on the surface (Druguet et al. 2008). Given the subhorizontal nature of the lineations within

the RBD, this is a reasonable assumption**.** Given the unknown nature of the lineations within the NEBD, this assumption may not be as robust for those data.

Some factors can complicate strain analysis methods using deformed dikes and veins. Dikes and veins are typically emplaced within a host rock during deformation, which seems to be the case in this region (Druguet et al. 2008); therefore, they only record a portion of the strain path. Thus, it can be assumed that overall strain is likely higher than strain estimates from deformed dikes and veins. The rheology of dikes and veins also vary from the rheology of the host rock. At initial emplacement, they were weaker or less competent than the host rock so will deform more than the host rock. However, as the dikes and veins cool, they typically become more competent than the host rock. More competent veins and dikes will record lower strain than the more pliable host rocks. Conversely, less competent veins will record higher strain values than present in the host rocks. Additionally, dikes and veins may not have been emplaced in perfect planes, and may even have been intruded in zig-zag patterns, further complicating the estimation of the strain ellipsoid (Druguet et al. 2008; Druguet et al. 2012). Druguet et al. (2012) provided criteria to determine whether the dikes and veins were intruded as straight planes and care was taken to avoid strain analysis in areas with strong rheological contrasts that would likely result in problems.

Ratios of X to Y and Y to Z were calculated for the ellipsoids from the folded and boudined veins. The 3D strain ellipsoid data were plotted on both Flinn and Hsu plots to obtain the shape of the ellipsoid. On the more commonly used Flinn plots, if the data plot closer to the X/Y (vertical) axis, then the ellipsoid is prolate; whereas if the data plot

closer to the Y/Z (horizontal) axis, then the ellipsoid is oblate (Flinn 1965; Hobbs et al. 1978). However, if the data plot along a 1 to 1 line drawn from the origin, the ellipsoid shows plane strain (Flinn 1965; Hobbs et al. 1978). The orientations of the axes were also plotted on equal area stereonets.

While Flinn plots are more commonly used, Hsu plots are also useful for strain ellipsoid shape visualization, as they allow for direct comparison of strain magnitude between ellipsoids of different shapes. Natural strain magnitudes for each direction were calculated using the following formula: $\epsilon_x = \ln (1 + X)$ (Hossack 1968; Hobbs et al. 1978). Once natural strains were calculated, Lode's parameter was found using the following equation:

$$\upsilon = (2\epsilon_Y - \epsilon_X - \epsilon_z) / (\epsilon_x - \epsilon_z)$$ (Hossack 1968; Hobbs et al. 1978).

Lode's parameter indicates the shape of the ellipsoid; if $\upsilon = -1$, then the ellipsoid is prolate (and constriction is dominant), if $\upsilon = 0$, then plane strain is dominant, and if $\upsilon = 1$, then the ellipsoid is oblate (and flattening is dominant) (Hobbs et al. 1978). Lastly, the strain magnitude was calculated using the equation:

$$\epsilon_s = ((\ln X - \ln Y)^2 + (\ln Y - \ln Z)^2 + (\ln Z - \ln X)^2)^{1/2} / 3^{1/2}$$ (Hossack 1968; Czeck et al. 2009).

*3.2g: Mafic Enclaves*

Long and short axes and rake angles for mafic enclave surfaces were entered into text files for Rf/Phi analysis using Dr. Adolph Yonkee's suite of strain programs (see Yonkee et al. 2013). Each surface was analyzed to obtain average final ratios (Rf), initial

ratios (Ri), and angle of maximum elongation (φ) using the Rf/Phi technique. This technique finds two-dimensional strain ellipses based on the axial ratios and rake of the enclaves for each plane and will allow evaluation of any potential initial preferred orientation that may skew the final results (Lisle, 1985). In this technique, the tensor mean ratio (R) and direction (ϕ) of the two-dimensional shape ellipse for all enclaves on a plane were calculated using the approach of Shimamoto and Ikeda (1976), with uncertainties determined by bootstrap statistics (Mulchrone et al. 2003).

Each two-dimensional ellipse has an Rf (final aspect ratio) and φ (angle of elongation) value that can be used to obtain the three-dimensional strain ellipsoid. The Rf/Phi program from Adolph Yonkee's suite of strain programs (Yonkee et al. 2013) was used to analyze this data, which utilizes the method by Owens (1984) for best-fitting a tensor ellipsoid and incorporates the addition of Monte Carlo simulations to estimate uncertainties.

While the Rf/Phi technique is useful for strain modeling, it may not be entirely appropriate to use it with mafic enclave data, as initial enclave shapes vary greatly and may have large initial ratios (Paterson et al. 2004). Unlike the folded and boudined veins and dikes (which intruded into the unit during deformation), the mafic enclaves were present in the rock prior to deformation so they will record the full finite strain. However, they record only the finite strain of the enclaves themselves. The whole rock strain may be more or less depending on the relative strengths of the enclaves versus the host rocks. In this case, we estimate that the mafic enclaves are less competent, and therefore more strained than the host rock. Despite its limitations, the Rf/Phi technique is

the best available to analyze the strain recorded by the mafic enclaves, so the best approach requires careful and conservative interpretations of the results.

Before the two-dimensional strain estimates can be used to find a three-dimensional strain ellipsoid, one additional scaling step is necessary. From the raw output of the Rf/Phi program, each value was scaled to its natural strain value by the following formula: Rf = ln(Rs/Ri). Axial ratios for mafic enclaves are extremely high, as they are normally long and narrow features. This may skew the raw strain data so that any attempts at best-fitting an ellipsoid will be inconsistent and impossible to evaluate accurately. The natural strain allows the raw data to be scaled down to a usable value so that a realistic ellipsoid can be determined.

Once the scaled values for each surface were obtained, they were input into the Strain3D program, which outputs a Flinn plot along with principal axes for the three-dimensional strain ellipsoid. To obtain useful values, several different combinations of surfaces from each station were run in the Strain3D program. These Flinn plots are used to determine the shape of the strain ellipsoid (oblate, prolate, or plane strain). A Hsu plot was also drafted from the Strain3D output to visualize the strain ellipsoid.

*3.2h: Transpression modeling*

Kinematic modeling (after Fernández et al. 2013) was performed in order to determine the angle of simple shearing, the angle of extrusion, and $W_k$ during transpression using a simple spreadsheet in Excel. This model was selected because it is the most general model of ductile deformation with oblique collision (Fernández et al. 2013) and because the field evidence fits general aspects of transpression with vertical

flattening fabrics and asymmetric features on subhorizontal planes. Models were run in Excel at varying simple shear obliquity, ϕ, (0°, 20°, 160°) and extrusion angles, ν, (0°-170°) (Figure 8), with varying amounts of kinematic vorticity ($W_k$ = 0 to $W_k$ = 1) and shortening amounts. Simple shear obliquity (ϕ) was constrained to 20° E, 0°, and 20°W because of the field observations throughout the region. Asymmetric shear sense indicators like z-shaped folds, winged porphyroclasts, and winged conglomerate clasts are found predominantly on subhorizontal planes. Therefore, the ϕ value may be constrained to shallow angles (Czeck & Hudleston 2003; Fernández et al. 2013). Extrusion angle (ν) was left unconstrained because any extrusion angle (from 0° to 180°) is possible given the field evidence, and this angle does not need to be the same for every unit found in the Rainy Lake area (Fernández et al. 2013). The maximum range of kinematic vorticity values from 0 to 1, which relate to the ratios of simple to pure shear, were input for testing. Any kinematic vorticity value is possible for the region, as no field observations can accurately constrain the value in the gneisses. The modeling predicts the strain ellipsoid, both magnitude and orientation of the principal strain axes, for increasing values of finite strain. Therefore, for each set of ϕ, ν, and $W_k$, one can predict the orientation of the fabrics and the strain ellipsoid shape, magnitude, and orientation along a path of increasing strain. Flinn plots and orientations of the strain ellipsoids were output for each ϕ, ν, and $W_k$ set along the strain path. The trend and plunge of the orientation of the X-direction for each ϕ, ν, and $W_k$ set were plotted on an equal area stereonet to determine the strain path of the lineation and long axis of the strain ellipsoid. Two-dimensional horizontal ellipse sections were also calculated from the strain ellipsoid output.

All of the field data can be compared with the transpression modeling. Lineation data can be compared to the X axis of the strain ellipsoid for each model. If the lineation orientation overlaps with any of the points along a strain path, then it is a viable model. Flinn plots from mafic enclave data can also be compared to the models mathematically derived from Excel. The Excel spreadsheet outputs a logarithmic Flinn plot for each kinematic vorticity value's strain path. Like the lineation measurement, if the strain data from the mafic enclaves matches any point on the output Flinn plot, then it is considered a viable model. The angles of elongation of horizontal sections of the mafic enclave ellipsoids can be compared to similar horizontal sections of the model output ellipsoids. If the angles of elongation match, then the model is considered viable. This method has been applied to the Rainy Lake zone in the Seine metaconglomerates (Fernández et al. 2013), and offers additional constraints to the models fitted from the RBD and NEBD data.

*3.2i: Geochemical analyses*

A brief geochemical analysis was done on rocks from the RBD in attempt to distinguish the outer edge of the dome from the inner portions, as there is a distinct textural difference between the two. The geochemical signatures may help test dome emplacement models. X-ray fluorescence (XRF) was done on one sample each from RBD 13-01 and RBD 13-07. These were powdered in a shatter box and dried overnight at 105°C. 10.000 grams of flux (Claisse 50:50 LiT:LiM), 1.0 gram of ammonium nitrate, and 1.0 gram of sample were mixed together and fused in a crucible (Figure 9). The fused disks were analyzed in the Bruker S4 Pioneer XRF spectrometer at the University of Wisconsin- Milwaukee's Geosciences Department.

Bulk geochemical compositions were plotted on a ternary diagram modified from Martin et al. (2005), and trace element compositions were plotted on additional plots modified from Martin et al. (2005). Typical Archean TTG's are silica rich with high sodium concentration and low ferromagnesian minerals (Richards & Kerrich 2007).

X-ray diffraction (XRD) analysis was also conducted to check for typical primary minerals in granitoid rocks (such as quartz, varieties of K-feldspar, biotite, and amphibole). The same powders prepared for XRF analysis were further ground to smaller size, randomized, and analyzed using the XRD equipment housed at the University of Wisconsin- Milwaukee's Geosciences Department: a Bruker DB Focus XRD spectrometer with a Cu target and typical Bragg geometry (0.8 sec/step, 0.02° 2Θ step size, 2-50° 2Θ). The diffraction peaks obtained were analyzed and identified using the Bruker licensed EVA software and the ICDD database for comparison.

Samples were also sent to Michigan State University for inductively coupled plasma mass spectrometry (ICP-MS) analysis. ICP-MS allows for more accurate quantification of trace elements, which are often important markers in TTG (tonalite-trondhjemite-granodiorite) suites (e.g. Condie 2003; Martin et al. 2005), the group to which the RBD and NEBD belong. These analyses are still underway at the time of writing.

Trace element markers are useful in fitting TTGs into categories, particularly high-Al and low-Al groups. In high Al TTG's, elevated strontium and europium levels are typical with highly fractionated rare-earth element patterns, while the low-Al group is characterized by lower strontium levels and less fractionated rare-earth element patterns.

The relative abundances of Sr reflect the presence or absence of various minerals, namely garnet, amphibole, and plagioclase. High-Al TTG's contain garnet and amphibole, but no plagioclase, while low-Al TTG's do not contain garnet or amphibole, but do contain plagioclase (Martin et al. 2005). Other important elements to quantify are Ti, Nb, Y, Cr, Ni, and all rare-earth elements (Martin et al. 2005). Understanding the geochemistry of TTG's can potentially provide insight into crustal evolution and emplacement (Martin et al. 2005).

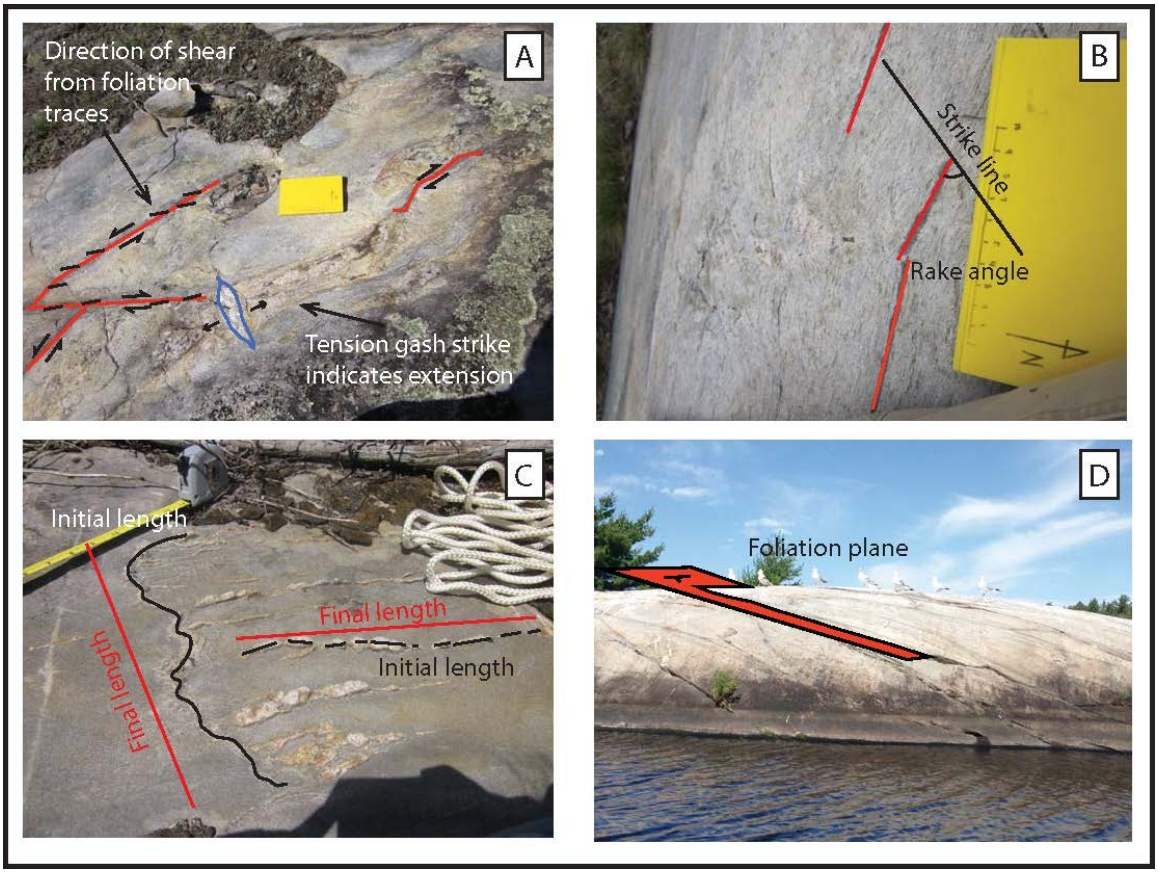


**Figure 6:** Field methods for data collection.

A: Field methods for tension gashes and shear zones. Shear zones identified by foliation deflections. Tension gashes identified by having both ends of the cracks visible. Tension gashes are usually filled with quartz. $\sigma_3$ is interpreted to be perpendicular to tension gash strike.

B: Mafic enclave measurement procedure. The long and short axes of the mafic enclave were measured based on a best-fit ellipse through the enclave. Strike of the surface marked, and rake angle from strike was recorded.

C: Fold and boudin measurement method. Initial and final lengths of folds and boudins recorded. The initial length of the folds was determined using a string following the fold (measurement taken once the string was stretched out). The initial length of the boudins was determined by adding all pieces of the boudined marker.

D: Foliation planes. Strike and dip taken of plane. Here, foliations within the RBD are shown.

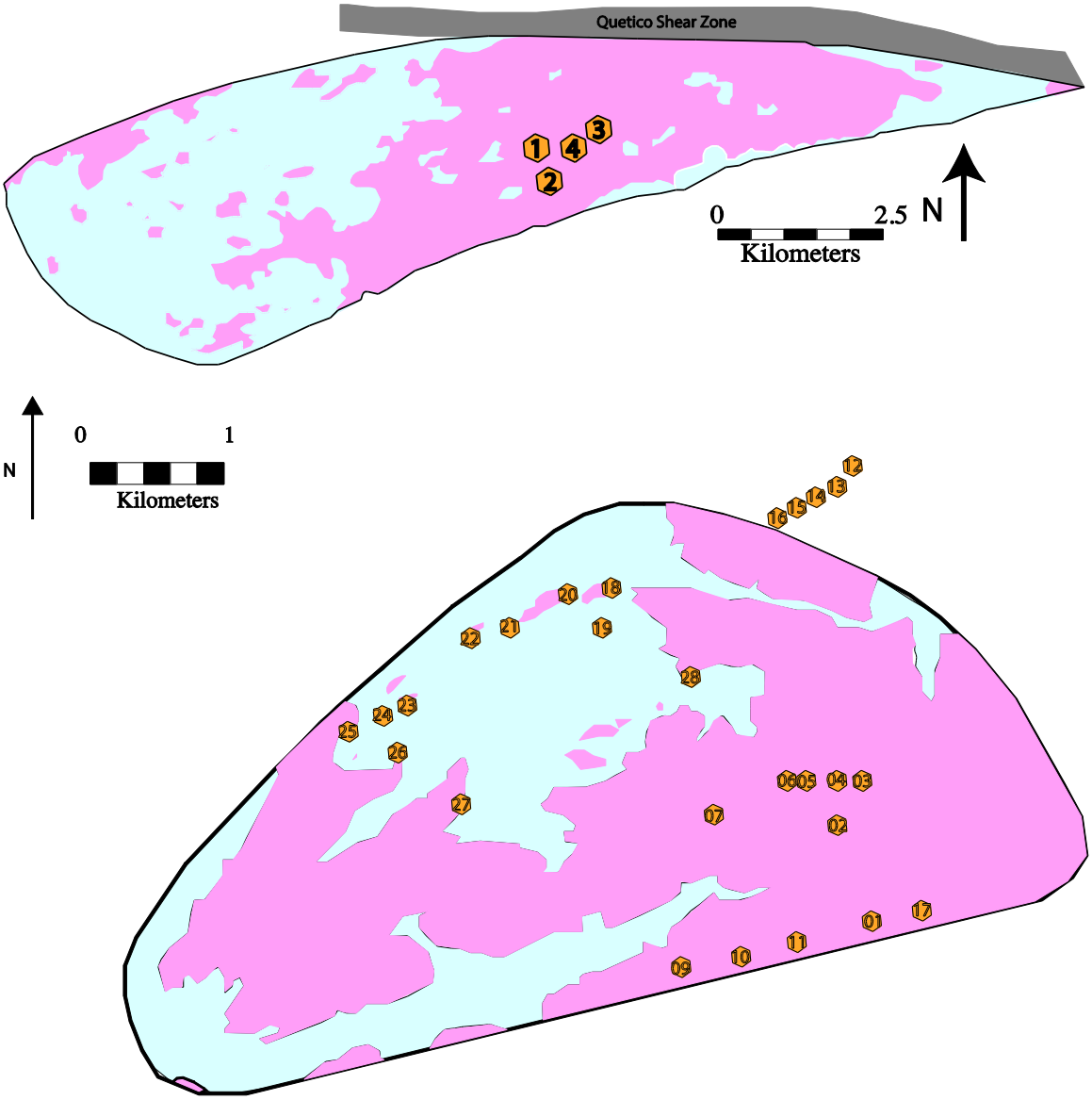


**Figure 7:** Sampling locations.

**Figure 7a (top):** Stations in the NEBD.

**Figure 7b (bottom):** Stations in the RBD.

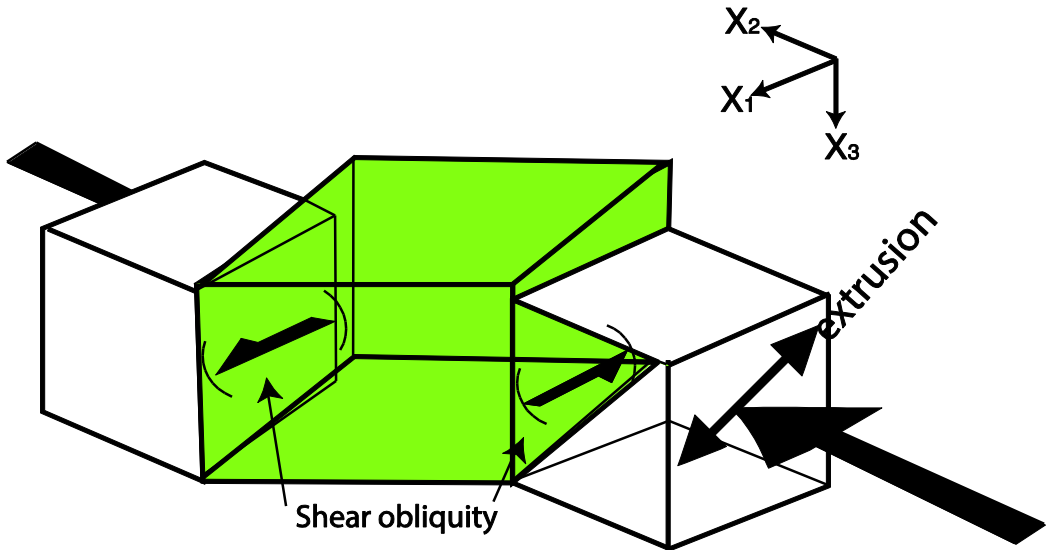


**Figure 8:** Triclinic transpression with varying shear obliquity and extrusion angles shown. Possible shear obliquity angles determined from field studies, extrusion angles are variable. Modified from Fernández et al. (2013).

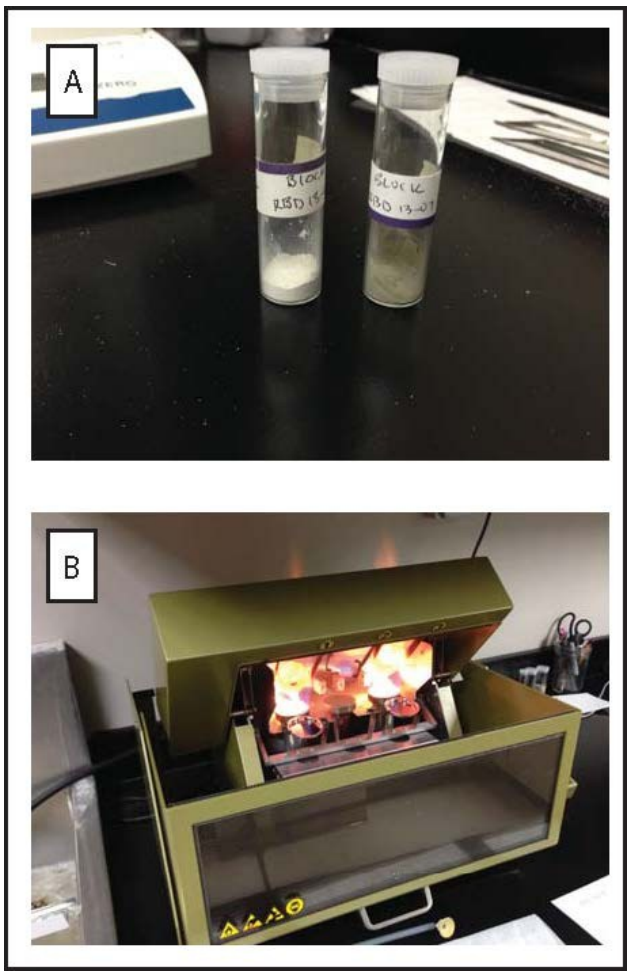


**Figure 9:** XRF/XRD methods.

A: Powdered samples from RBD stations 13-01 (left) and 13-07 (right). Note distinct coloration difference between the two samples. Powders not used for XRF fusing were later ground to a finer grain size and run through XRD.

B: Fusing process to produce glass bead for XRF analysis.

# Chapter 4: Data

*4.1: Stereonets*

*4.1a: Foliations*

Within the RBD, foliation was measured at all 28 outcrops, for 35 total measurements. The foliation in the RBD is strong and typically defined by alignment of biotite. Where mafic enclaves were present (along the southern edge of the dome), many of the smaller enclaves were aligned with the foliation plane. Figure 10 shows poles to foliation planes from the RBD. Foliations are generally moderately to steeply dipping, and are oriented roughly in the E-W direction, with the exception of a few foliation planes oriented to the NW-SE (Figure 11). The average foliation plane for the northern dipping cluster of foliations is 262, 61 N, while the average plane for the southern dipping cluster is 089, 53 S. These orientations reflect the domed nature of the unit.

Figure 10 also shows poles to foliation planes for the NEBD. Foliation in the NEBD is strong, and formed from the alignment of biotite. Foliation planes were more difficult to find in the NEBD due to the effects of glaciation and weathering; most outcrops were "moundy" and covered with a considerable amount of overgrowth. Foliations are steeply dipping and strike NE-SW (Figure 12), with an average orientation for the northern dipping foliations of 262, 61 N, and an average orientation of 047, 69S for the southern dipping foliations.

*4.1b: Lineations*

Figure 11 shows lineations found in the RBD. Foliation fabrics were much stronger than lineation fabrics, creating a general S>L fabric. Lineations were often

difficult to find or absent. When present, lineations were formed by elongated quartz or biotite grains. Lineations were observed at eight stations. They varied in orientation between stations, plunging shallowly-moderately in variable directions (Figure 11). No lineations were visible in the NEBD, due to a lack of exposed foliation planes.

*4.1c: Shear zones*

111 shear zones were measured at 20 outcrops within the RBD. Shear zones were identified by observations of foliation bending into distinct bands, indicating sheared offsets. They were largely observed on subhorizontal planes, but were occasionally seen in the third dimension. On the subhorizontal outcrops, they formed an anastomosing pattern. Where they could be seen intersecting on steep planes, the shear zones were steeply dipping throughout most of their extent and changed to a shallower dip only near the intersections. The total affect was to create shear zone bounded lozenges of relatively less deformed rocks where the vertical length of the lozenge was potentially the longest dimension.

In the RBD, shear zones were of both dextral and sinistral sense. However, dextral shear markers were dominant, with 69% of shear zones being dextral and 31% being sinistral (Figure 13a). Shear zones were more common in the central parts of the dome (Figure 14). Both sinistral and dextral sets strike generally east-west and dip steeply to moderately north, but the dextral set shows more variation in dip. The range in dextral shear zone dip is from about 30 degrees to 90 degrees, while the sinistral shear zone dips range from about 60 degrees to 90 degrees. The average sinistral shear zone orientation is 262, 80 N; and the average dextral shear zone orientation is 275, 69 N.

47 shear zones were measured at all four outcrops within the NEBD (Figure 15). Shear zones were identified by deflections of foliation into bands of tightly packed and aligned minerals. They were only observed on subhorizontal planes, as the third dimension was not exposed. Consequently, very few of these shear zones were exposed so that dip could be identified; therefore, they are plotted on rose diagrams (Figure 13b). The average strike of the shear zones in the NEBD is 094. In the NEBD, all shear zones were of dextral sense.

*4.1d: Detailed analysis of shear zones at location RBD 13-07*

One well-exposed outcrop towards the center of the Rice Bay dome, RBD 13-07, yielded a detailed view of the anastomosing shear zones. The main continuous outcrop is approximately 5.5 m in length, and 1-2 m in width, however many smaller exposures are located in the immediate vicinity. More shear zones were visible within the neighboring exposures, but the connections between them could not be seen due to lichen and bog cover. A tracing was made of the large outcrop with visible connections and digitized in Adobe Illustrator, and photographs of the outcrop were stitched together into one image (Figure 16a). Shear zone orientations were measured directly on the outcrop and are noted on Figure 16b, along with foliation traces and locations of large quartz nodules.

65 shear zones were measured in this detailed investigation. Dextral shear zones outnumber sinistral shear zones in this outcrop (Figure 16c). 70% of the shear zones are dextral, while 30% are sinistral. The dextral strands are generally wider than the sinistral strands (Figure 16d), perhaps indicating that these played a greater role in deformation and were active for longer periods of time (Mitra, 1979; Carreras et al. 2010). Only one

clear crosscutting relationship was observed (Figure 16b) where a large (>10 cm wide) dextral shear zone cuts and offsets a narrower sinistral shear zone. This is the only clear cross cutting relationship present, and all other sinistral shear zones have not been offset. Unfortunately, foliation deflections at confluences to determine relative timing (e.g. Carreras et al. 2010) did not prove to be useful at this outcrop because the relationships were not clear. The one cross-cutting relationship that indicates the wide dextral shear zone offset the narrow sinistral one suggests that the dextral strand had a prolonged history that outlasted its sinistral counterpart. This, combined with the lack of cross-cutting relationships between other shear zone sets, could indicate that earlier sinistral shear zones formed first, but later sinistral shear zones formed simultaneously with the dextral shear zones.

*4.1e: Tension gashes*

Tension gashes were classified for this study as infilled cracks where both ends of the crack were visible. 94 tension gashes were measured at 13 outcrops within the RBD. They were found at many locations within the RBD (Figure 17). Tension gashes within the RBD vary in composition, with the majority observed being quartz filled (46 tension gashes). K-feldspar tension gashes were also common (13), with few (5) being filled with a mixture of quartz and feldspar. Some tension gashes along the southern margin of the dome appeared to be stained red, suggesting the presence of iron, similar to other areas of the Rainy Lake zone where siderite alteration is common and carbonate and quartz rich fluids were demonstrably coeval (Poulsen 2000; Czeck and Poulsen, 2010). These iron-rich tension gashes are abundant at outcrop RBD 13-10, with 23 of the observed 29 Fe-filled tension gashes being observed there (Figure 18).

The orientations of tension gashes are diverse, so the "average" orientation may not be too meaningful. The average strike of the quartz tension gashes is 079 degrees, but the rose diagram indicates that the largest cluster of them have an orientation of 100 degrees (Figure 18). For K-feldspar tension gashes, the average strike is 091 degrees, but the rose diagram indicates the largest cluster is oriented nearly north-south (Figure 18). The average strike of the five mixed K-feldspar and quartz tension gashes match the cluster on the rose diagram at 080 degrees (Figure 18). Lastly, the iron-rich tension gashes display a bimodal distribution. More tension gashes strike NE-SW, as reflected by the average (062 degrees), but the remaining tension gashes are clustered in the NW-SE direction, at a high angle to the main set (Figure 18).

35 tension gashes were measured at three outcrops within the NEBD. They were located at all stations within the NEBD (Figure 19). In the NEBD, only quartz and K-feldspar filled tension gashes were present. As in the RBD, the quartz tension gashes are more abundant than the K-feldspar tension gashes (28 quartz, 8 K-feldspar). Average strike for the quartz tension gashes is 093 degrees, although the rose diagram indicates the greatest cluster in the NW-SE direction (Figure 20). There is a considerable amount of variation between the strikes of the quartz tension gashes. The K-feldspar tension gash strikes, on the other hand, are tightly clustered in the NE-SW direction, and the average orientation is 070 degrees (Figure 20).

*4.1f: Quartz veins*

28 quartz veins were measured at 7 outcrops within the RBD. They were located mainly along the southern portion of the RBD (Figure 21), but not observed within the

NEBD. Late-stage quartz veins in the RBD have variable orientations. Many dip vertically, however a significant portion of the dataset has moderate to shallow dip. Veins strike in variable directions. The average orientation of all veins (total 37) is 341, 12 NE, but this estimate is likely not a good representation of the data set. Where quartz veins are present, they appear to preferentially emplace close to the strike and dip of the foliation (Figure 22).

*4.2: Mafic enclave strain estimates*

Mafic enclaves were observed at 3 outcrops (Figure 23), all found near the southern border of the RBD. A summary of the output of the Strain3D program for the mafic enclaves is shown in in Figure 24. The program requires input from three planes, so several runs were conducted to incorporate data from as many planes as possible, resulting in several ellipsoid solutions from each station. The three stations with sufficient data for analysis yielded different results, with RBD 13-11 indicating a flattening fabric; RBD 13-01 indicating near plane strain; and RBD 13-17 indicating plane strain to slightly constrictive fabrics. Strain was fairly low across all stations, with the exception of RBD 13-11. RBD 13-11 showed the highest strain magnitude. Strain magnitudes from RBD 13-01 and 13-17 were fairly low. Principal directions for each ellipsoid are also shown (Figure 24). The X-axis orientation from most ellipsoids calculated from the enclave data matched the observed lineation orientations (where present), with the exception of the run from RBD 13-17. This station also had a high amount of uncertainty associated with its Strain3D Flinn plot. One run from RBD 13-01 (run 4) did not match either.

The Hsu plot of the mafic enclave data (Figure 25) not only indicates the shape of the ellipsoid, but also provides a convenient way to compare the magnitude of the strain between each location. Each station indicates the same strain ellipsoid shape as the corresponding Flinn plot (RBD 13-01 plane strain, RBD 13-11 flattening, and nearly plane strain for RBD 13-17). RBD 13-01 and RBD 13-17 have the lowest strain magnitudes, while RBD 13-11, the example with the flattening strain, has the highest strain magnitude. Strain magnitudes are fairly low.

*4.3: Strain determined from folded & boudined dikes and veins*

The best fold and boudin data were available in the NEBD, and all were measured on subhorizontal planes. Nine folds and boudins were present in NEBD 13-01, while only five were present in NEBD 13-02. When the data were combined at each outcrop, a horizontal two-dimensional strain ellipse was calculated. Both stations have a similar angle of maximum elongation (φ) N79E and N82E, respectively (Figure 26). However, the ellipse from NEBD 13-02 (axial ratio of 1.629) has a lower eccentricity (long axis / short axis) than the ellipse from NEBD 13-01 (axial ratio of 2.059), suggesting that these neighboring outcrops had different strain magnitudes.

Following the technique of Druguet et al. (2008) and utilizing the assumptions described in Chapter 3, the full three-dimensional strain ellipsoids were calculated for each outcrop. When this was done, the long axis was found to be vertical, not consistent with the subhorizontal lineations found within the RBD, but potentially consistent within the NEBD since lineations were not observed at outcrop. For NEBD 13-01, the scaled principal strain magnitudes are: X = 1.85, Y = 1.05, Z = 0.51. For NEBD 13-02, the

scaled principal strain magnitudes are: X = 1.64, Y = 0.99, Z = 0.62. The principal axes of the strain ellipsoid were plotted on the Flinn diagram (Figure 27). Results from both outcrops plot very close to the plane strain line, just as the Flinn plots from the mafic enclaves in the RBD. However, data from NEBD 13-01 indicates a slight flattening fabric while data from NEBD 13-02 indicates a slight constriction fabric. Both stations yield results indicating low strain, but on average higher than the strain magnitudes of the mafic enclaves in the RBD, as shown by the Hsu plot (Figure 28).

*4.4: Transpression models*

Three types of data were compared to the 30 possible transpression models generated for reasonable values of φ (0°, 20°, 160°), ν (0°-180°), and simple shear rate/ pure shear rate ratio $\frac{\dot{\gamma}}{\dot{\varepsilon}}$ (0.5, 1, 2, 4, 6 and 20; and their corresponding kinematic vorticity numbers $W_k$: 0.24, 0.45, 0.71, 0.89, 0.95 and 0.99) (Appendix A). The kinematic vorticity value, $W_k$, is a mathematical representation of the type of shear dominant. If pure shear is the dominant operator, then $W_k$ will be 0. If simple shear is dominant, then $W_k$ will equal 1. Values between 0 and 1 are combinations of simple and pure shear. First, for all stations with lineation data, the lineation trend and plunge of each station was compared to each possible modeled scenario (Step 1, see Figure 29; Appendix A). Next, for outcrops with mafic enclave strain data, 2D ellipse sections were generated for a range of kinematic vorticity numbers from the models that matched measured lineations for each station. Then, the angles of elongation and strain magnitudes for the model ellipse sections were compared to horizontal slices of the 3D ellipsoid (orientation and strain magnitudes) of the mafic enclave data (Step 2, see Appendix A). Lastly, for those

stations with mafic enclave 3D strain data, the shape of the ellipsoid (prolate or oblate) can be compared to the Flinn plots generated by the models (Step 3, see Figure 29; Appendix A). The same procedure was undertaken for the two NEBD outcrops with estimated 3D strain data derived from 2D folded and boudined veins.

Eight stations within the RBD were used during Step 1 of model comparisons. From the results of Step 1, most models that fit the lineation data were those with higher kinematic vorticity values (0.8-1). Matching values of φ and ν varied for each outcrop, as shown in Appendix A and Table 1. Generally, more vertical (160°-180°; 0°-30°) angles of extrusion were more common fits than horizontal ones. The best fit shear obliquity angle, φ, varied as well. For one station, RBD 13-05, all kinematic vorticity values coincided with the lineation for three φ and ν scenarios, but this was abnormal for the data set. Generally, a smaller range of kinematic values fit the data at each station, but the matching kinematic values were not the same everywhere (Appendix A).

2D ellipse sections derived from the models were calculated for a wide variety of $\frac{\dot{\gamma}}{\dot{\varepsilon}}$ values (0.5, 1, 2, 4, 6, 20) for stations RBD 13-01 (model φ = 20°, ν = 170°), RBD 13-11 (model φ = 20°, ν = 170°), and RBD 13-17 (model φ = 20°, ν = 170°) (Appendix A). Mafic enclave strain data (Rs and strain magnitude) were compared to the model 2D ellipse sections in this, Step 2 of the procedure. Model φ = 20, ν = 170 was the only model tested for Rs and strain magnitudes due to it being the only viable model for these stations after Step 1. The Rs values for every kinematic vorticity number began at low axial ratios and increased to impossible unreasonably high ratios with continued increasing strain. Angles of elongation typically begin at about 45 degrees to the shear

plane and rotate towards being parallel with the shear plane. Horizontal sections from ellipsoids of all runs derived from mafic enclave data were compared to these values. The Rs and angle of elongation data from the model matched the data best at low and medium amounts of finite strain. Models that fit the data yielded Rs amounts of approximately 1.0 to 2.0.

The 3D strain shapes from the models were compared to the mafic enclave Flinn plots as well. Most models appear to originate as plane strain or nearly plane strain, but move to the flattening field with increasing strain for all kinematic vorticities. This 3D strain shape pattern matches the field data of the RBD well (Table 1).

Given all steps, the best fit models to the RBD data are $\varphi = 20°$, $\nu = 170°$, with a high kinematic vorticity value ($W_k$ approaches 1). Although the data did not perfectly match at RBD 13-01 or 13-11, this model was the only likely model, and was a perfect fit for RBD 13-17 (Table 1).

Transpression modeling was also performed on the NEBD using the data from the folded and boudined veins and dikes. Lineations from the NEBD were not directly observed, but are assumed to be steeply plunging based on the analyses from folded and boudined veins analysis. The direction of the X-axis from the strain analysis is assumed to be close to the lineation orientation (as demonstrated by Czeck et al. 2009 and many other studies). These assumed lineation orientations were compared to the X axes from the model output, just as for the RBD (Step 1).

Transpression modeling was also performed on the NEBD using the data from the folded and boudined veins and dikes. From the 3D strain ellipsoids obtained by

manipulating the two-dimensional EllipseFit outputs, it was determined that the Y-Z plane was on the horizontal surface, and the X axis was vertical. Therefore, 90°→090 can also be used as an approximate lineation value. The foliation planes from the stations at which folds and boudins were abundant had very steep foliation planes as well, further justifying the approximation of the lineation being close to 90°. This approximate lineation orientation was compared to the model outputs of the X-axis, just as for the RBD. There were 8 models matching this vertical lineation, and they matched for most $W_k$ strain paths (as the strain paths approach a vertical orientation). φ values varied for the NEBD data (each station had at least one matching model with each shear obliquity value tested). ν values were somewhat constrained to vertical to subvertical extrusion angles (0°, 10°, 170°). In almost every model, all $W_k$ values (0.24-1) were possible.

For these 8 models, the secondary Excel sheet to cut the 3D ellipsoid along a horizontal sectional ellipse was used and compared to the 2D ellipses output from EllipseFit for the field data (Step 2). As both stations had a similar strain ellipse, the results were very similar for this step between the two stations. Rs values from field observations were 1.70 and 2.01 (13-01 and 13-02, respectively), with angles of elongation of roughly N 80 E. Both stations matched models with lower kinematic vorticities (0.24-0.71), indicating a considerable amount of pure shear was occurring in the NEBD.

Finally, the Flinn plot from the folded and boudined veins was compared to the strain ellipsoid outputs from the models (Step 3). This final stage provided the means to further limit the possible matching models.

Most models matched the strain data at lower kinematic vorticities (where deformation is dominated by pure shear with a component of simple shear), but some matched the data at all kinematic vorticities. Six models for NEBD 13-01 ($\varphi = 0°$, $\nu = 0°$, 10°, 170°; $\varphi = 20°$, $\nu = 10°$, 170°; $\varphi = 160°$, $\nu = 10°$) and five models for NEBD 13-02 ($\varphi = 0°$, $\nu = 10°$, 170°; $\varphi = 20°$, $\nu = 10°$, 170°; $\varphi = 160°$, $\nu = 10°$) are considered possible. Therefore, the simple shear obliquity ($\varphi$) could be anywhere within 20° from horizontal, as suggested by the outcrop evidence, and was not further constrained by the modeling. The extrusion angle ($\nu$) was substantially constrained by the modeling and limited to within 10° from vertical in either direction for all models are very similar (Table 1).

*4.5: Geochemistry—XRF & XRD; ICPMS*

X-ray fluorescence analysis is useful in determining the major element and select trace element compositions of rocks, including Br, Y, Zr, Nb, V, Zn, Ni, Cr, Co, Ce, Sr, Ba, and Mn. However, some of these compositions from the XRF analysis have errors above the accepted threshold of 12% or are present in concentrations below the lower detection limit of the machine, and those compositions should be disregarded. Table 2 shows compositions of the two analyzed samples compared to the average late Archean TTG (tonalite-trondjhemite-granodiorite) suite (from Condie 2005) from the XRF study. At RBD 13-01, 70.47% of the sample was $SiO_2$, with 16.19% $Al_2O_3$, 5.66% $NaO_2$, 1.99% $K_2O$, and 2.31% CaO. At RBD 13-07, 72.74% of the sample was $SiO_2$, with 11.48% $Al_2O_3$, 3.86% $Na_2O$, 1.79% $K_2O$, and 0.25% CaO (Figure 30). A ternary diagram depicting the bulk element geochemistry (potassium, sodium, and calcium) indicates that both samples are highly sodic, with Na composing 5.66% of RBD 13-01 and 3.86% of

RBD 13-07 (Figure 31). Aluminum is also abundant, suggesting that the RBD is a high-Al TTG. Transition metals (such as iron and titanium) appear to be more abundant in RBD 13-07 (7.07% Fe2O3 at 13-07, compared to 0.91% at 13-01), taken from the center of the dome, while lighter elements appear to dominate the composition of the outer rim of the dome.

Figure 32 shows trace element compositions compared to the results of Martin et al. (2005) who studied trace elements in Archean tonalites. Trace element compositions of RBD 13-01 fit within these boundaries, but not as many meaningful data could be gathered from RBD 13-07 due to high errors in measurement. RBD 13-07 is enriched in iron oxides, but depleted in sodium.

X-ray diffraction results show that the main minerals composing RBD 13-01 are albite, quartz, and biotite. RBD 13-07 shows a nearly identical mineralogy, but with the addition of illite and garnet. This mineralogy is consistent with observations from the field in this and other studies (Poulsen 2000).

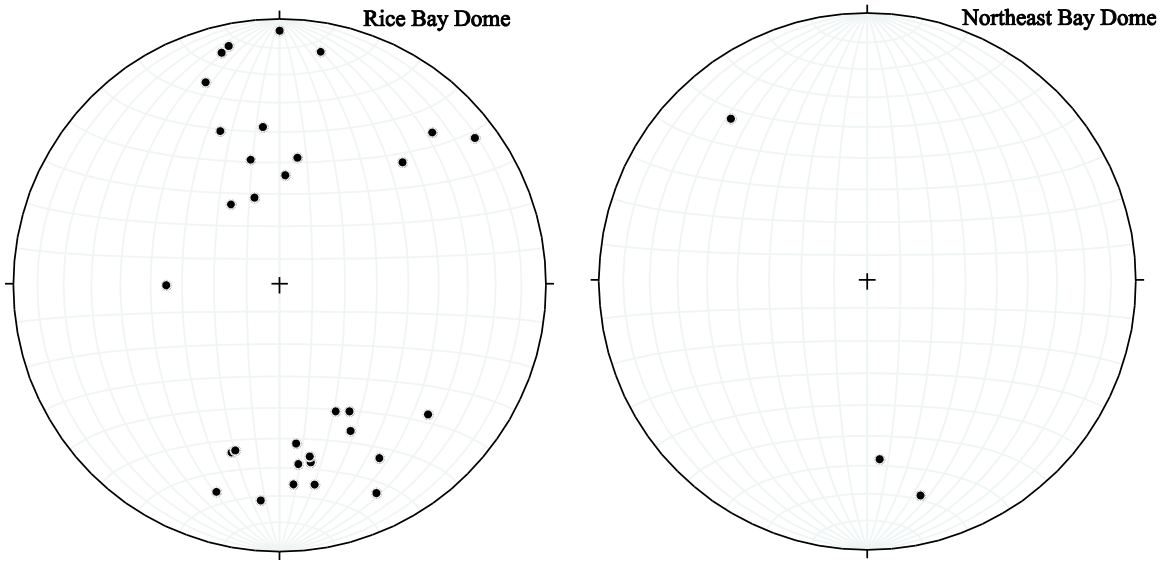


**Figure 10:** Poles to foliation planes for the RBD (left) and NEBD (right) plotted on equal area stereonets.

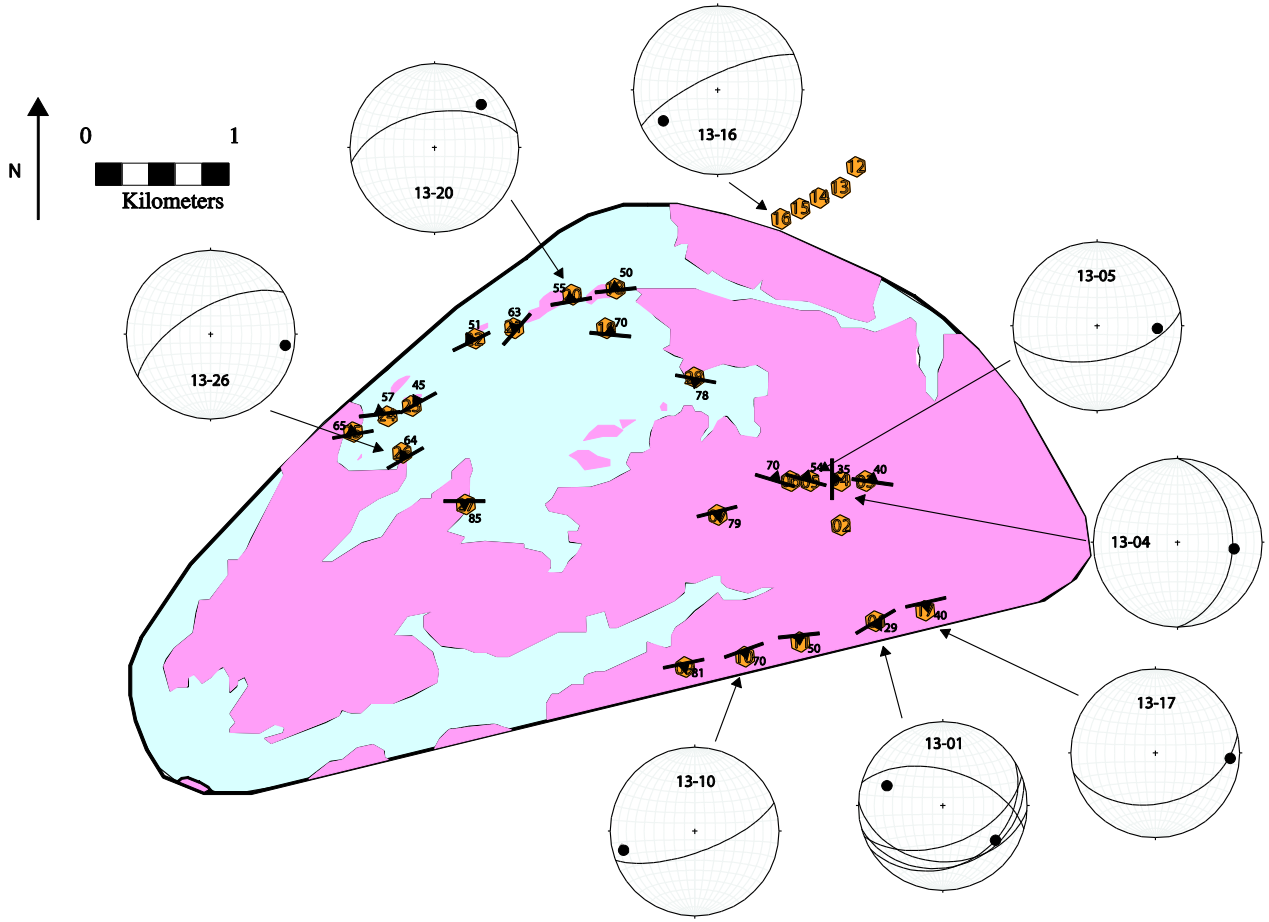


**Figure 11:** Foliation planes for the RBD. Equal area stereonets showing foliation and lineation also shown. Note E-W striking foliations and obliquely plunging lineation orientations.

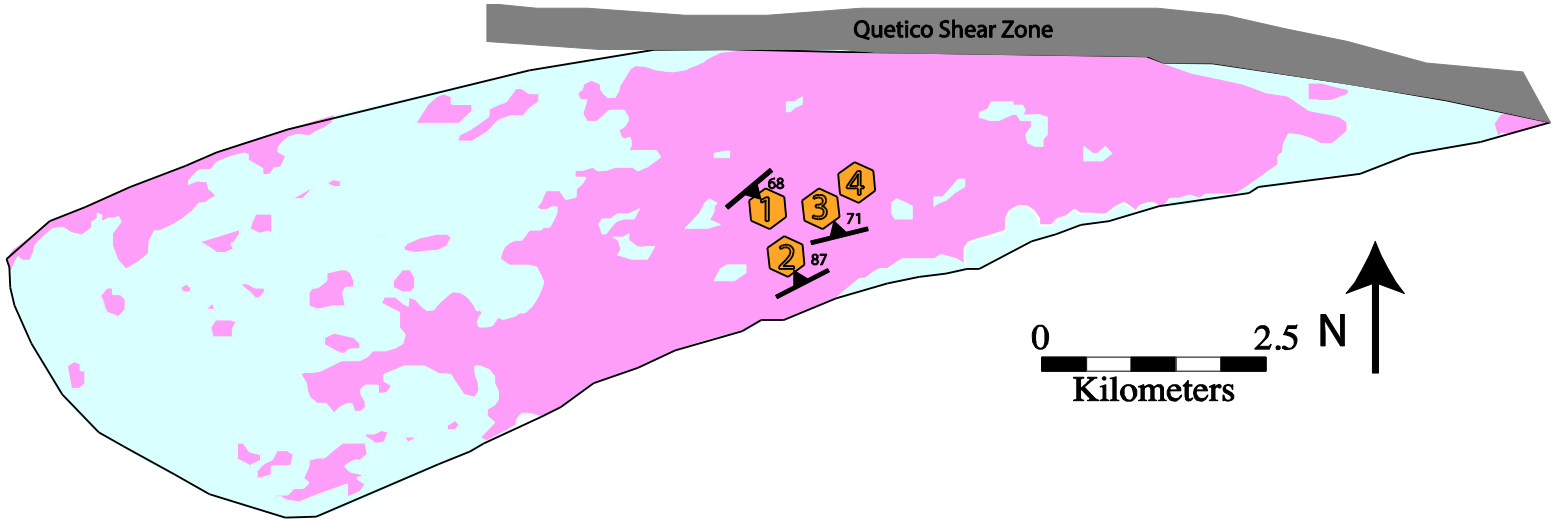


**Figure 12:** Foliation planes from the NEBD. Planes suggest a possible synformal structure.

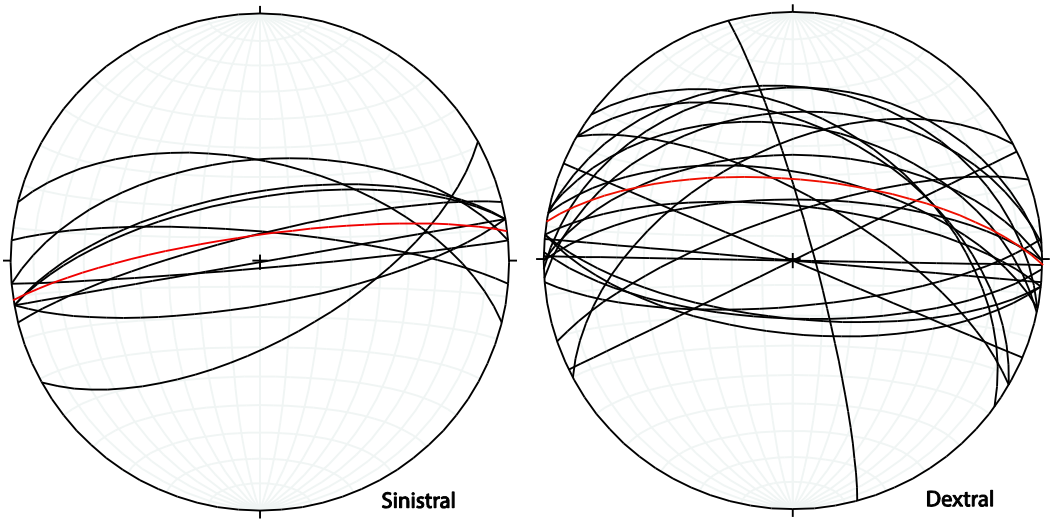


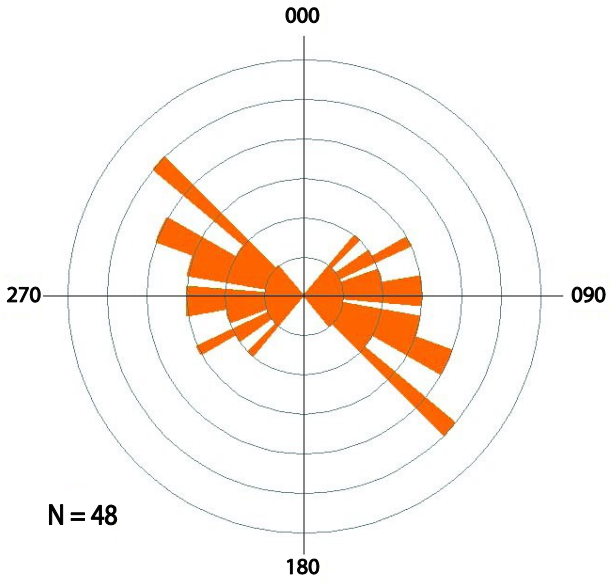


**Figure 13:** Shear zones observed in both domes.

**Figure 13a (top):** Shear zones for the RBD plotted on equal area stereonets. Average shear zone orientations marked in red. The average orientation for sinistral shear zones (left) is 262 80NW, while the average orientation for dextral shear zones (right) is 275 69 NE.

**Figure 13b (bottom):** Shear zone strikes for the NEBD plotted on a rose diagram (each concentric circle represents one feature). No sinistral markers observed; rose diagram is representative of all dextral markers (average strike 094).

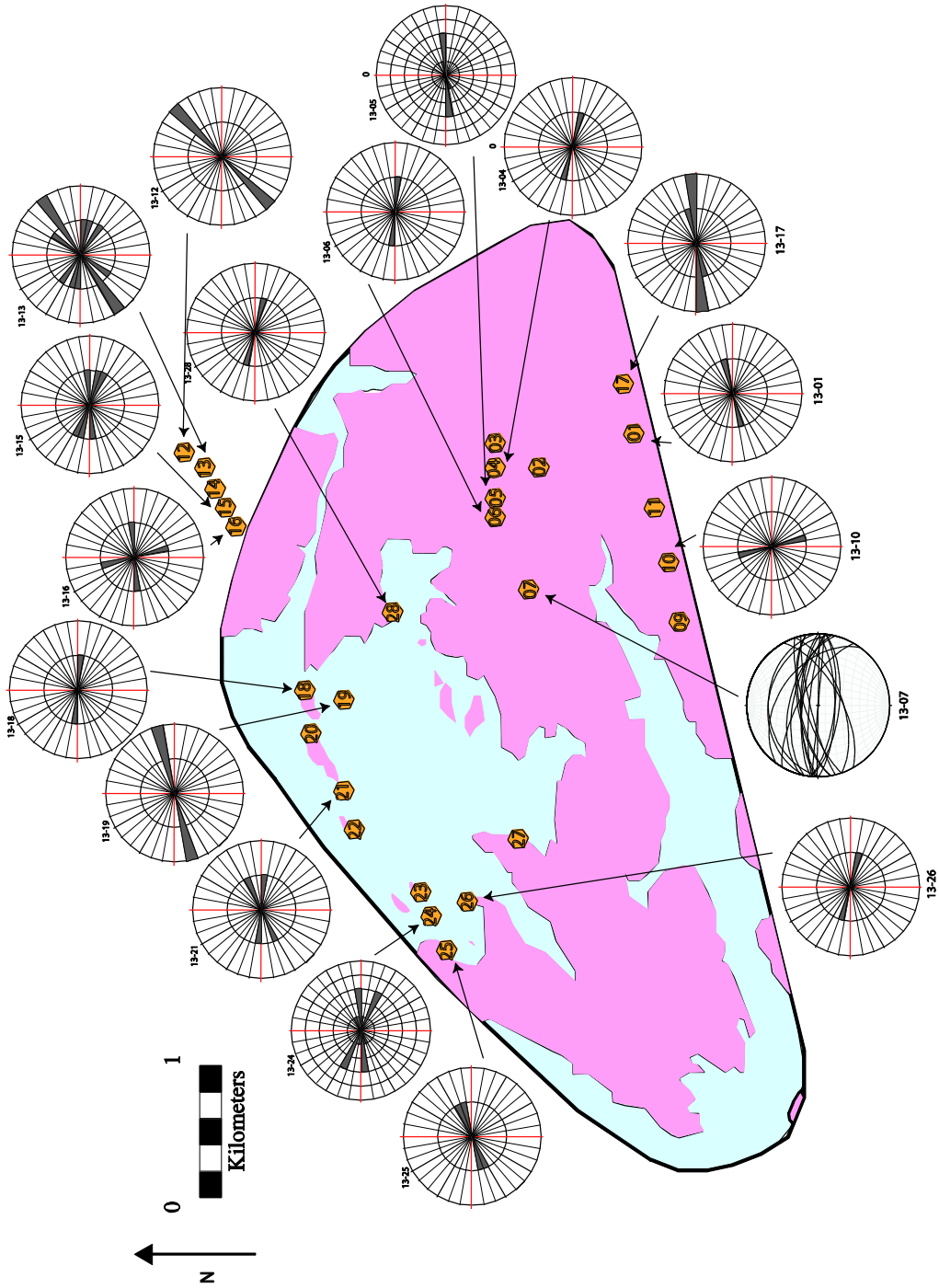


**Figure 14:** Spatial relationships of shear zones in the RBD. Where rose diagrams are plotted, one concentric circle indicates one feature. Equal area stereonet plotted at RBD 13-07 due to the large number of dipping shear zones present.

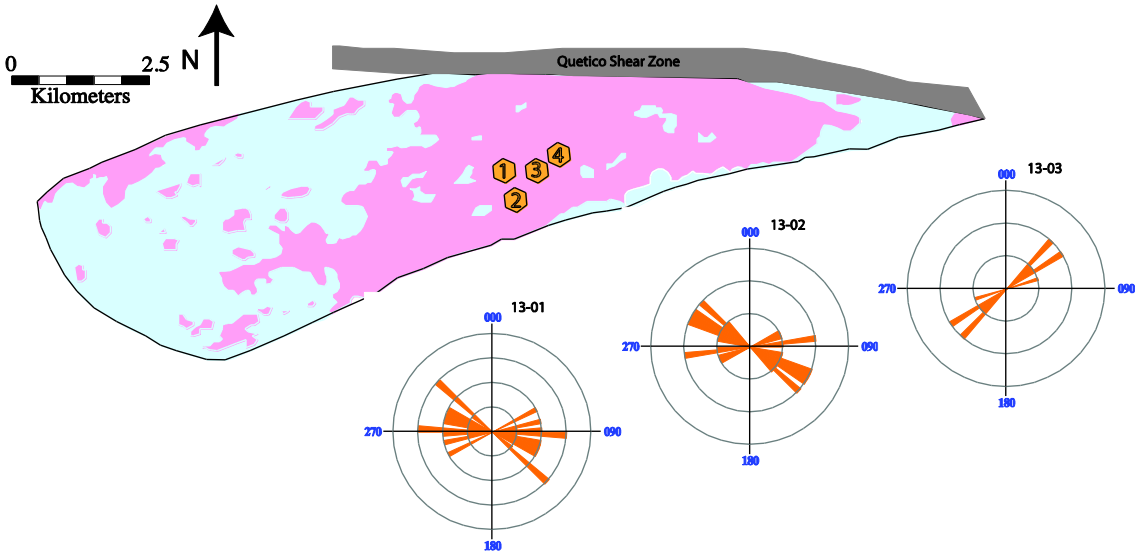


**Figure 15:** Spatial relationships of shear zones in the NEBD. On rose diagrams, each concentric circle indicates one feature.

**Figure 16:** Anastomosing shear zones at RBD 13-07.

**Figure 16a:** Anastomosing shear zones on subhorizontal plane found at station RBD 13-07. Above image is the outcrop stitched together in Adobe Photoshop. North is towards the left side of the page.

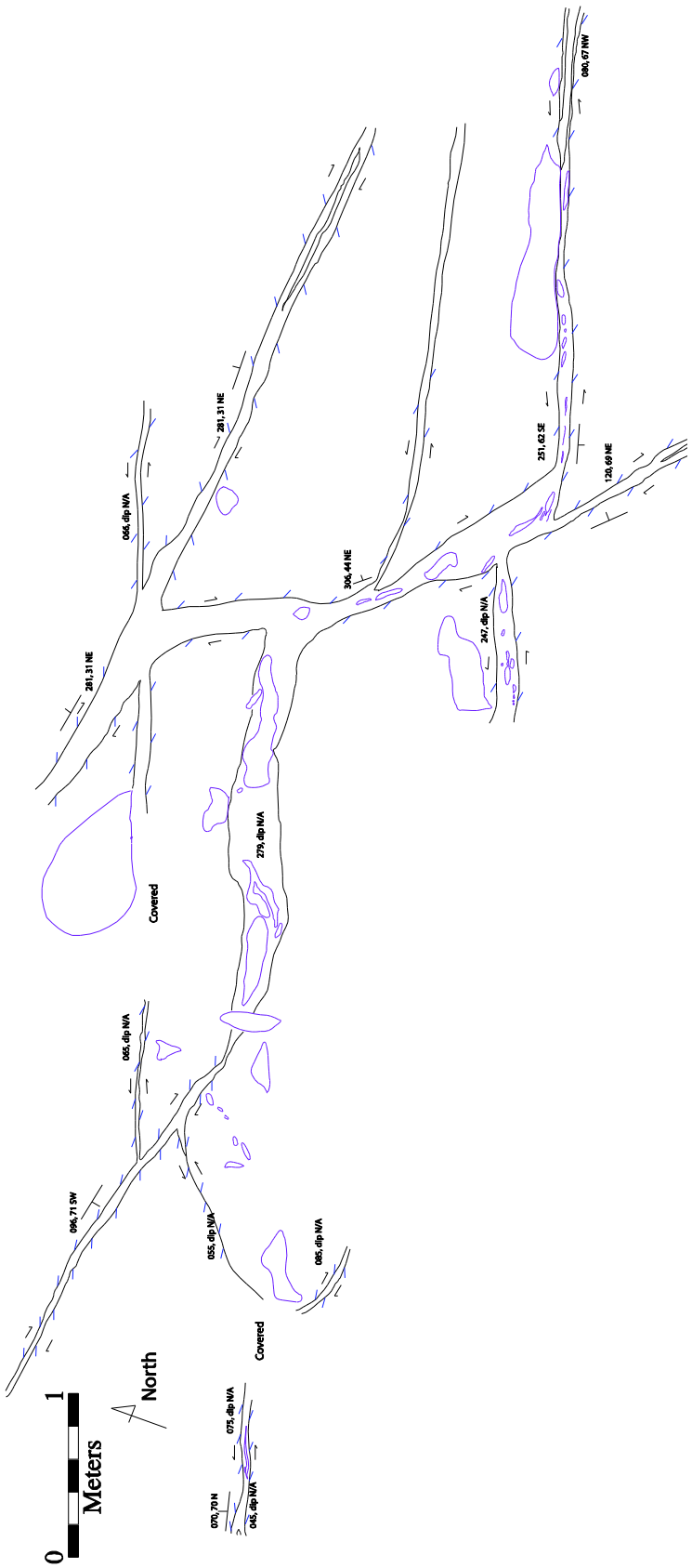


**Figure 16b**: Anastomosing shear zone tracing from RBD 13-07. Shear zone boundaries, strikes and dips, foliation traces, and quartz vein occurrences (likely gold-associated) marked.

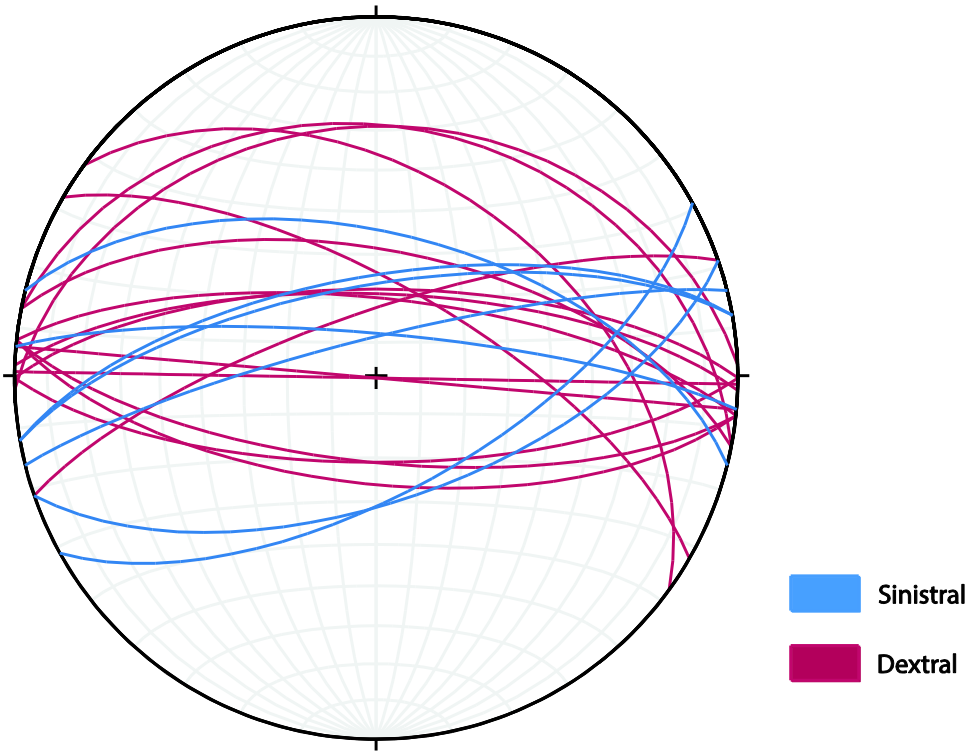


**Figure 16c**: Equal area stereonet of all shear zones present at RBD 13-07. Shear zones are 70% dextral and 30% sinistral, and oriented in the same manner as the overall shear zone orientation for the RBD

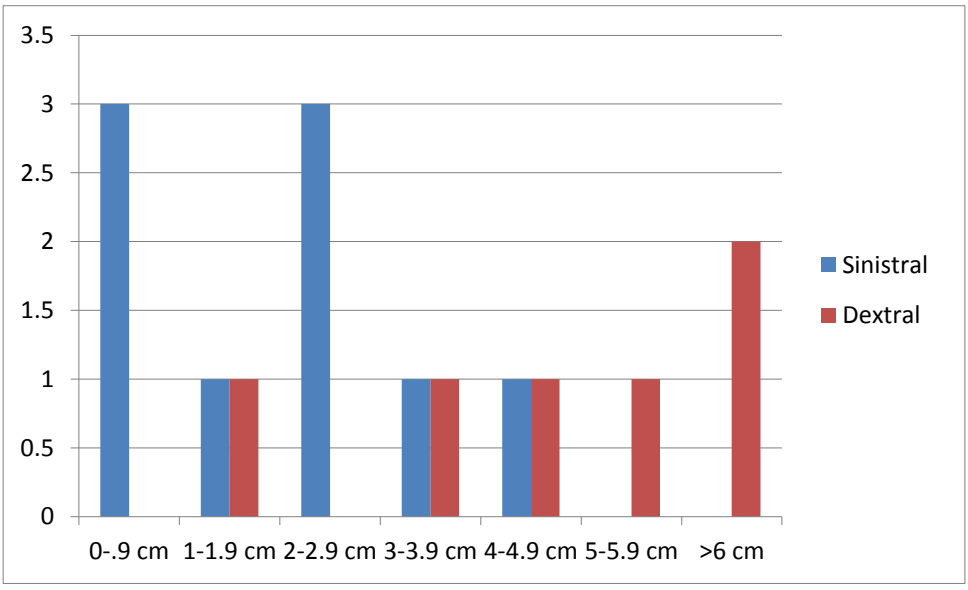


**Figure 16d**: Thicknesses of shear zones from shear zone tracing (Figure 16b). Dextral shear zones are considerably wider at the outcrop than sinistral ones.

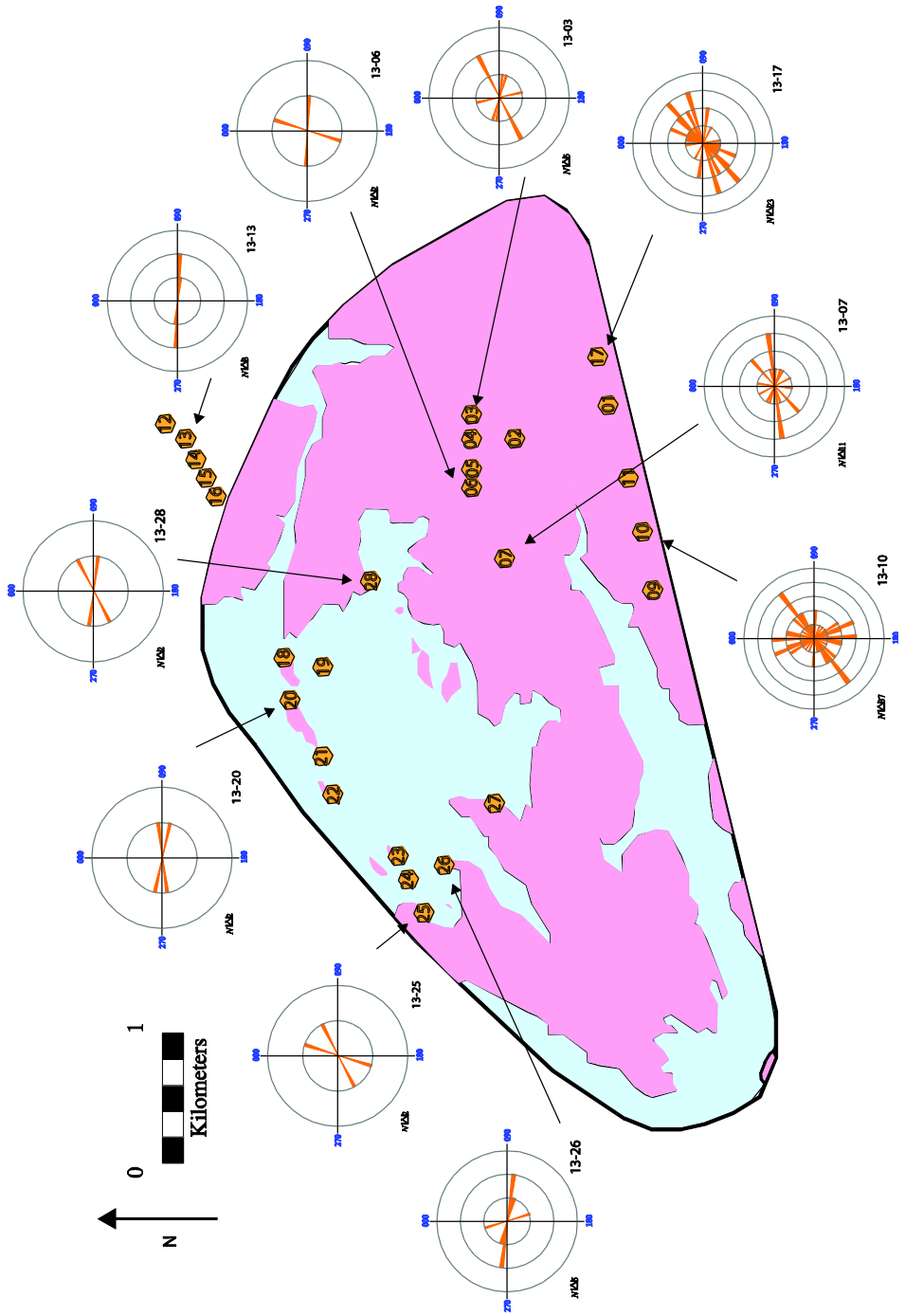


**Figure 17:** Tension gash locations and rose diagrams of tension gashes within the RBD. Late stage $\sigma_3$ stress field likely oriented NW-SE; perpendicular to vein envelopes. On rose diagrams, each concentric circle indicates one feature.

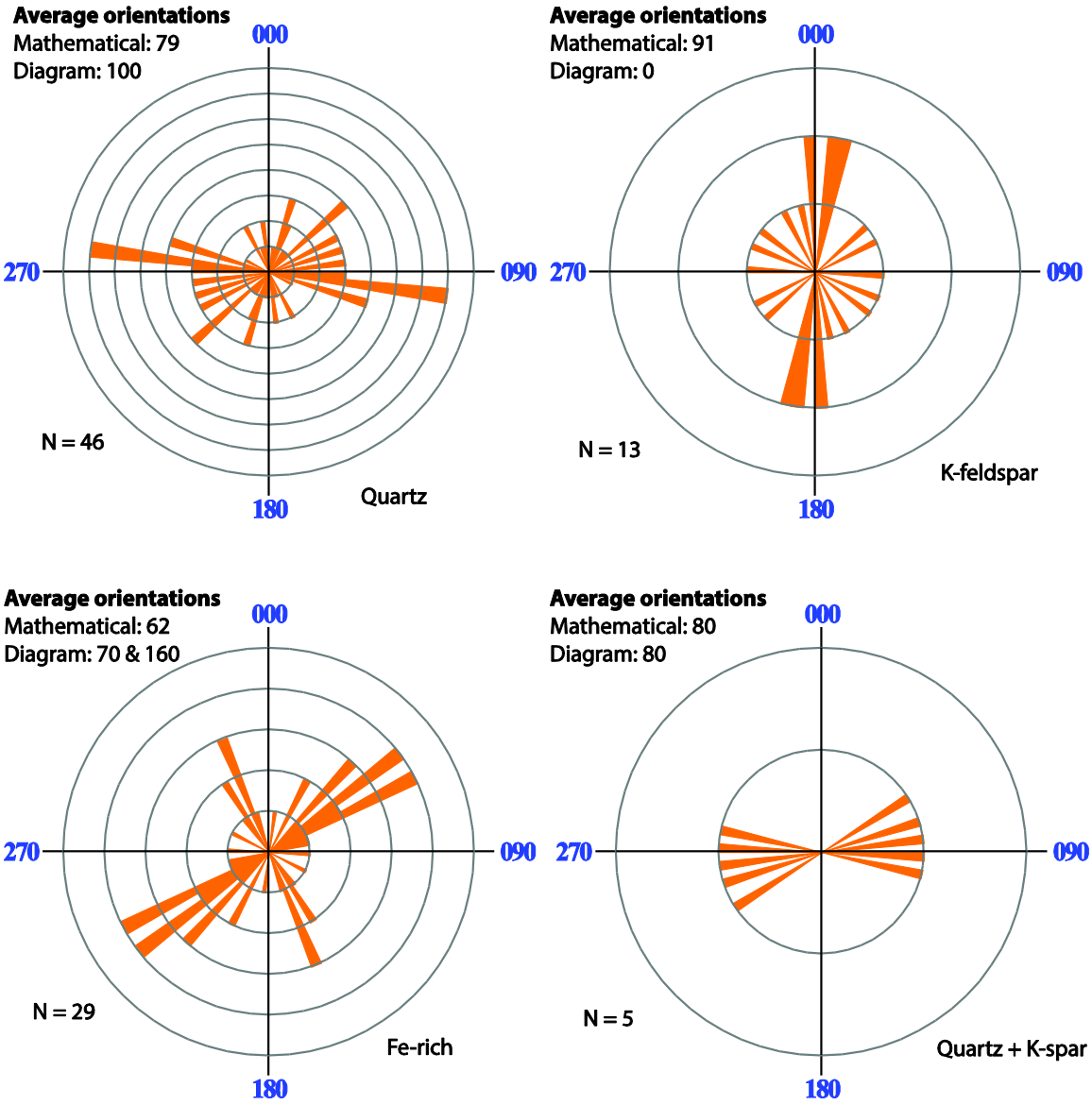


**Figure 18:** Rose diagrams of tension gashes within the RBD, grouped by type of fill. Both mathematical average orientations and visual estimations of orientations shown. For rose diagrams, each concentric circle indicates one feature.

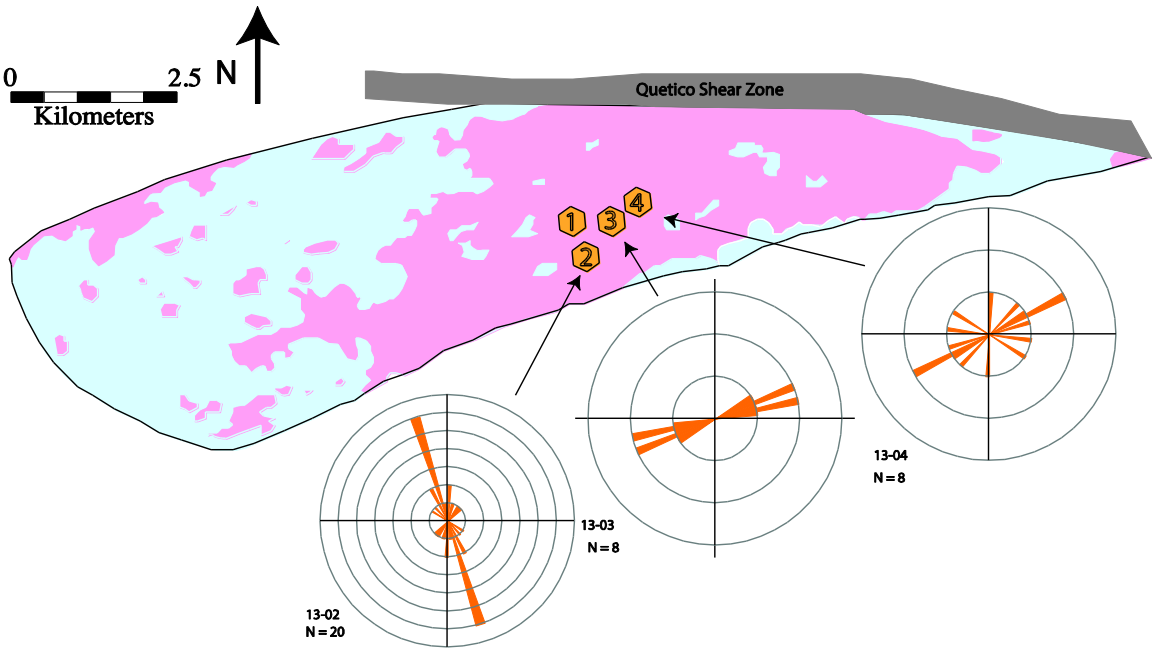


**Figure 19:** Locations and rose diagrams for tension gashes within the NEBD. $\sigma_3$ Stress field oriented similar to the RBD with the exception of station 13-02. Each concentric circle indicates one feature.

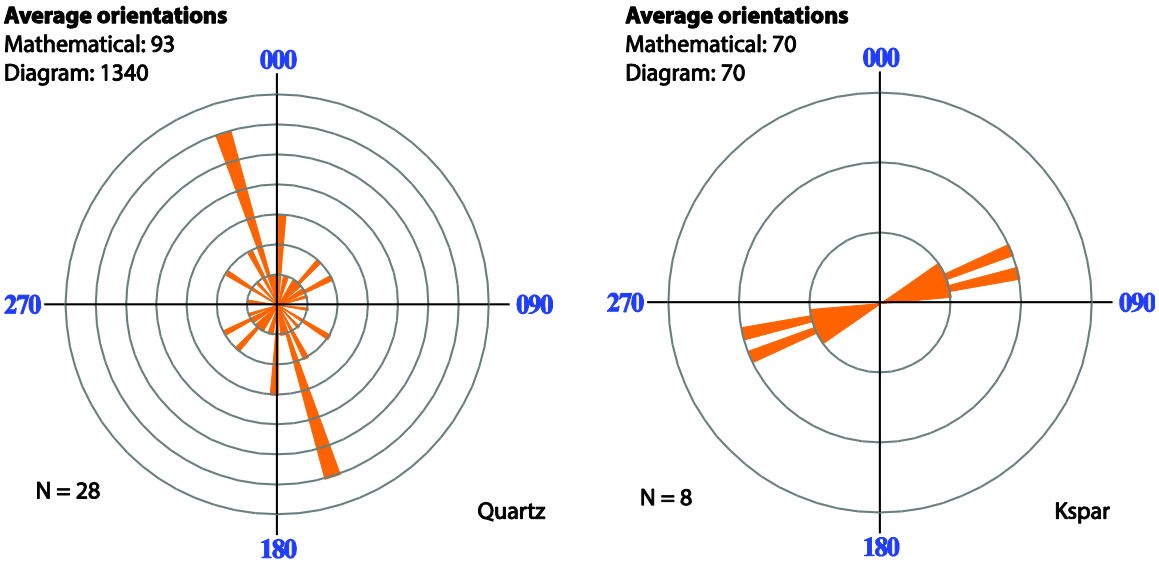


**Figure 20:** Rose diagrams of tension gashes within the NEBD grouped by type of fill. Quartz is most common. Each concentric circle indicates one feature.

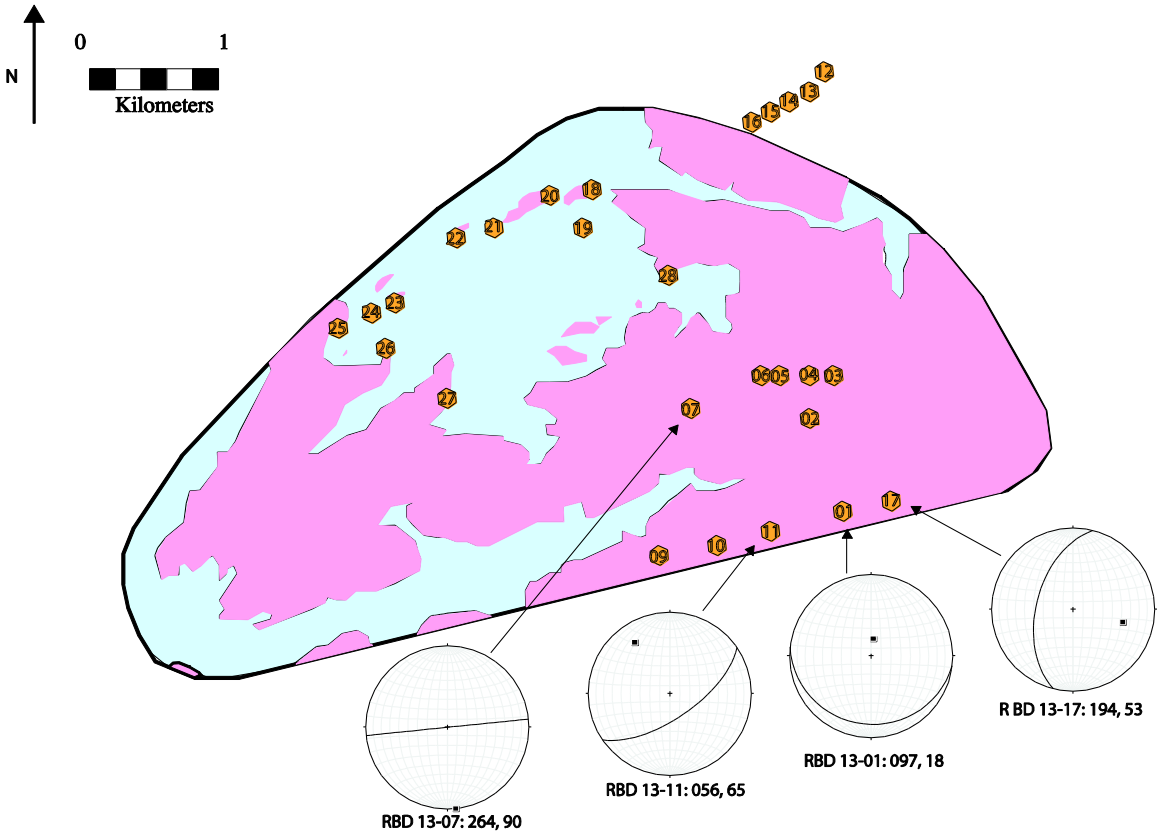


**Figure 21:** Equal area stereonets indicating average quartz vein orientations for each station within the RBD.

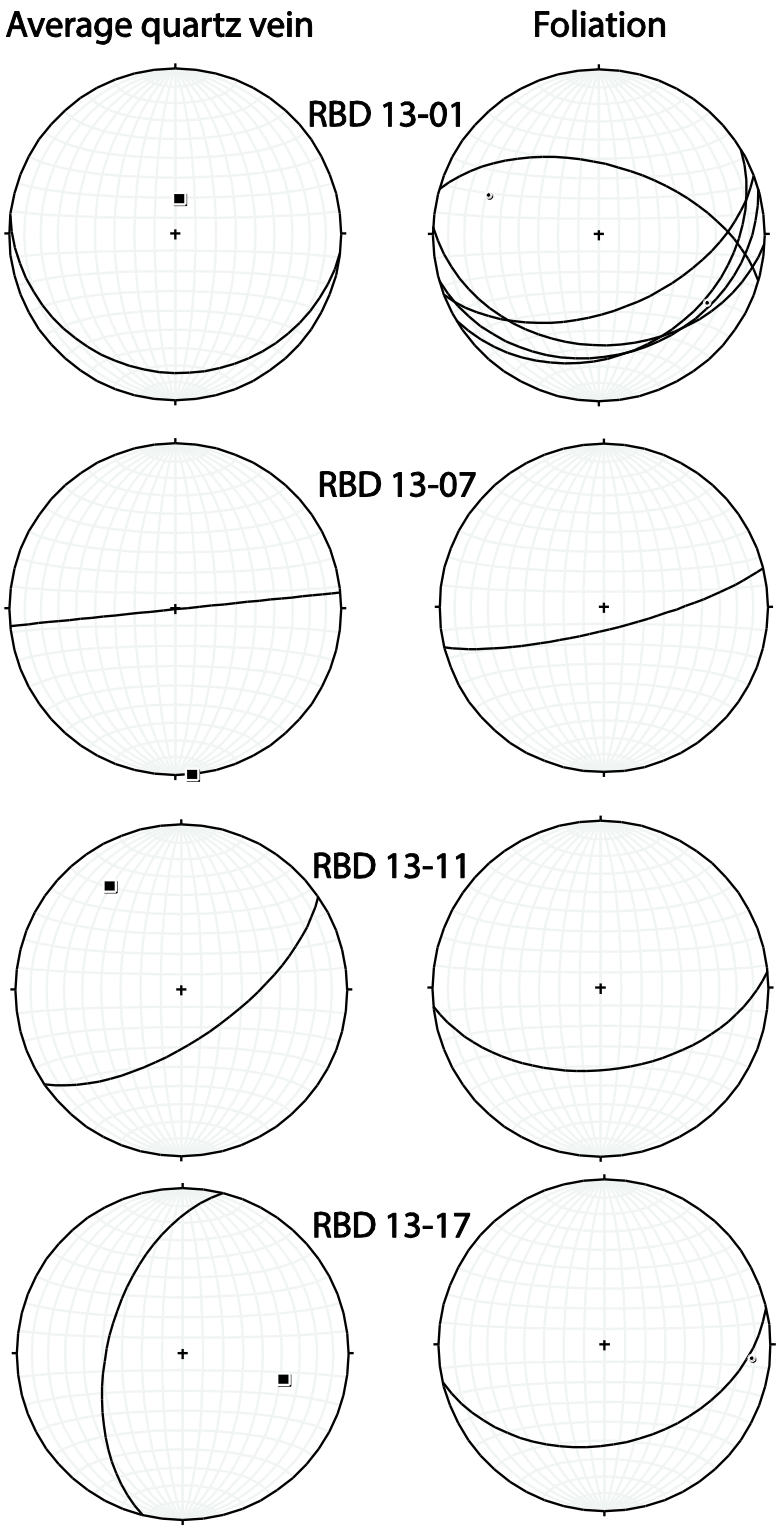


**Figure 22:** Equal area stereonets showing average quartz vein orientation (left) compared to foliation orientation (right) for each site. Note that the orientations of the average quartz vein generally matches the foliation orientation observed at each site.

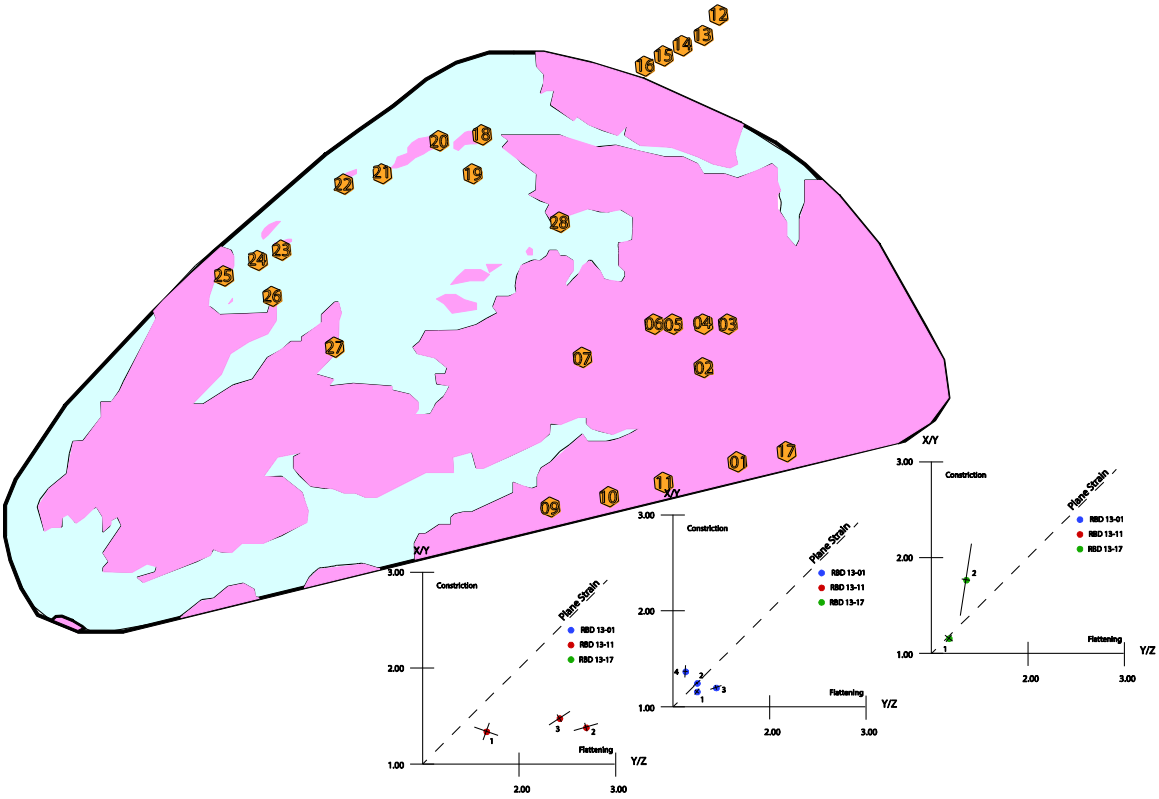


**Figure 23:** Flinn plots for each station in the RBD where mafic enclaves were found.

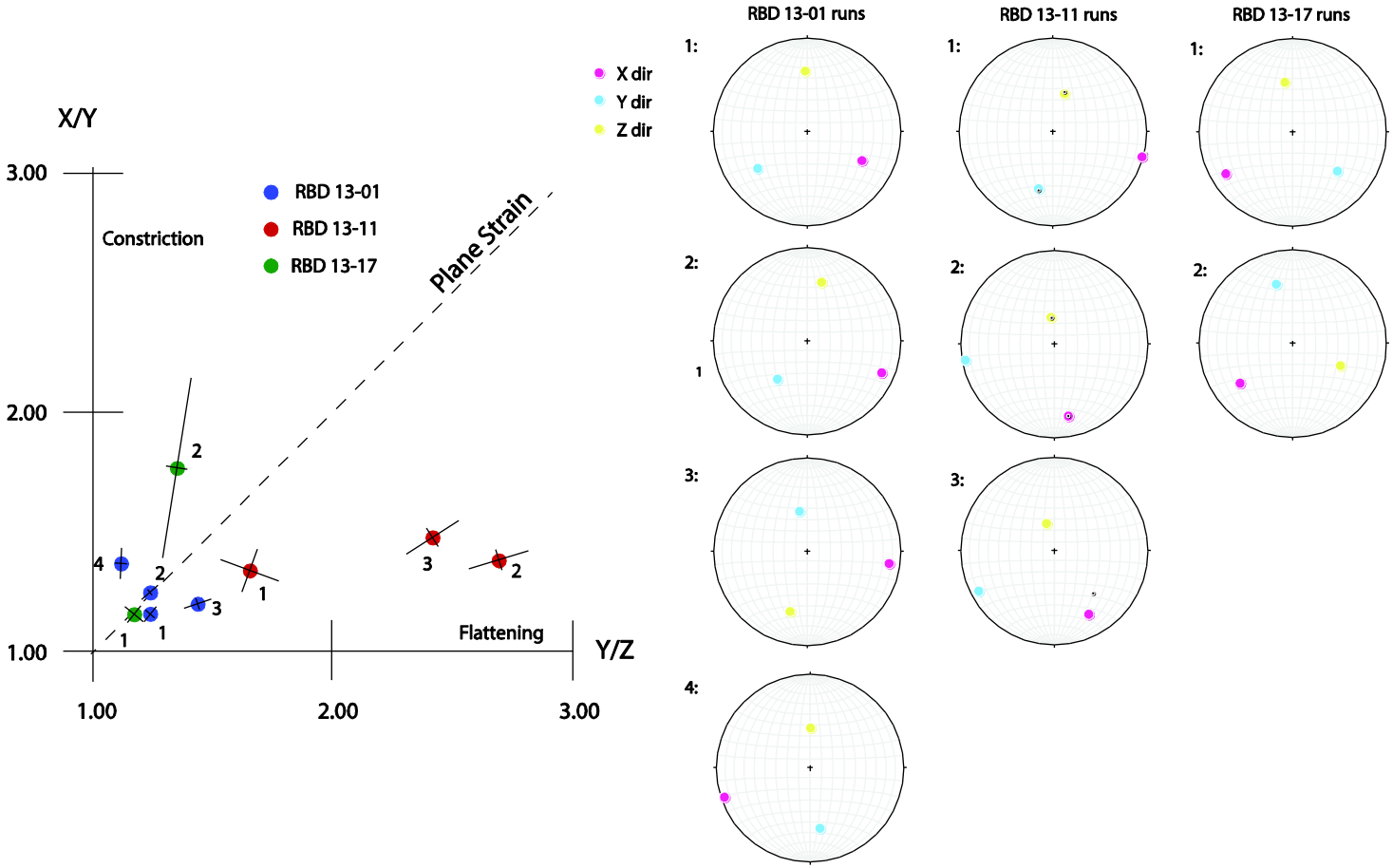


**Figure 24:** Flinn plots of all mafic enclave data combined. Error bars drawn on Flinn plot data points. Principal axes orientations shown at right.

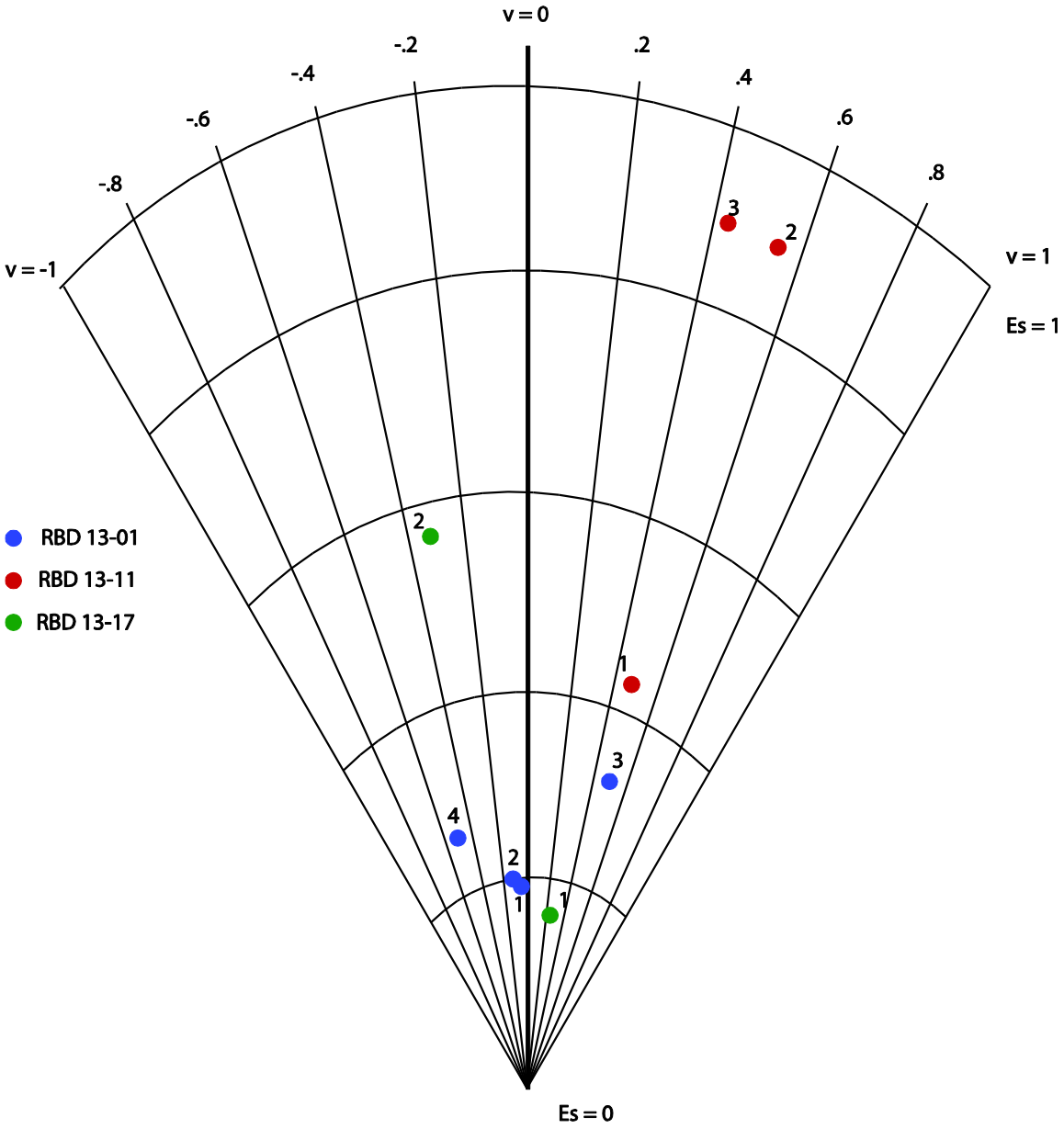


**Figure 25:** Hsu plot from mafic enclave data. Strain magnitude is low for most samples, with the exception of RBD 13-11.

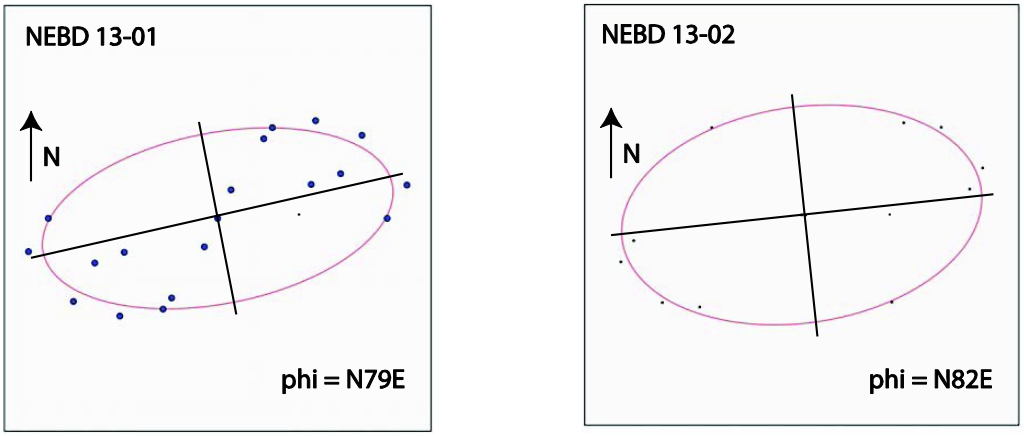


**Figure 26:** Output from EllipseFit modeling of folded and boudined dikes and veins on subhorizontal outcrops in the NEBD. NEBD 13-01 shows an angle of elongation of N79E, and NEBD 13-02 shows an angle of elongation of N82E (North is at top of page).

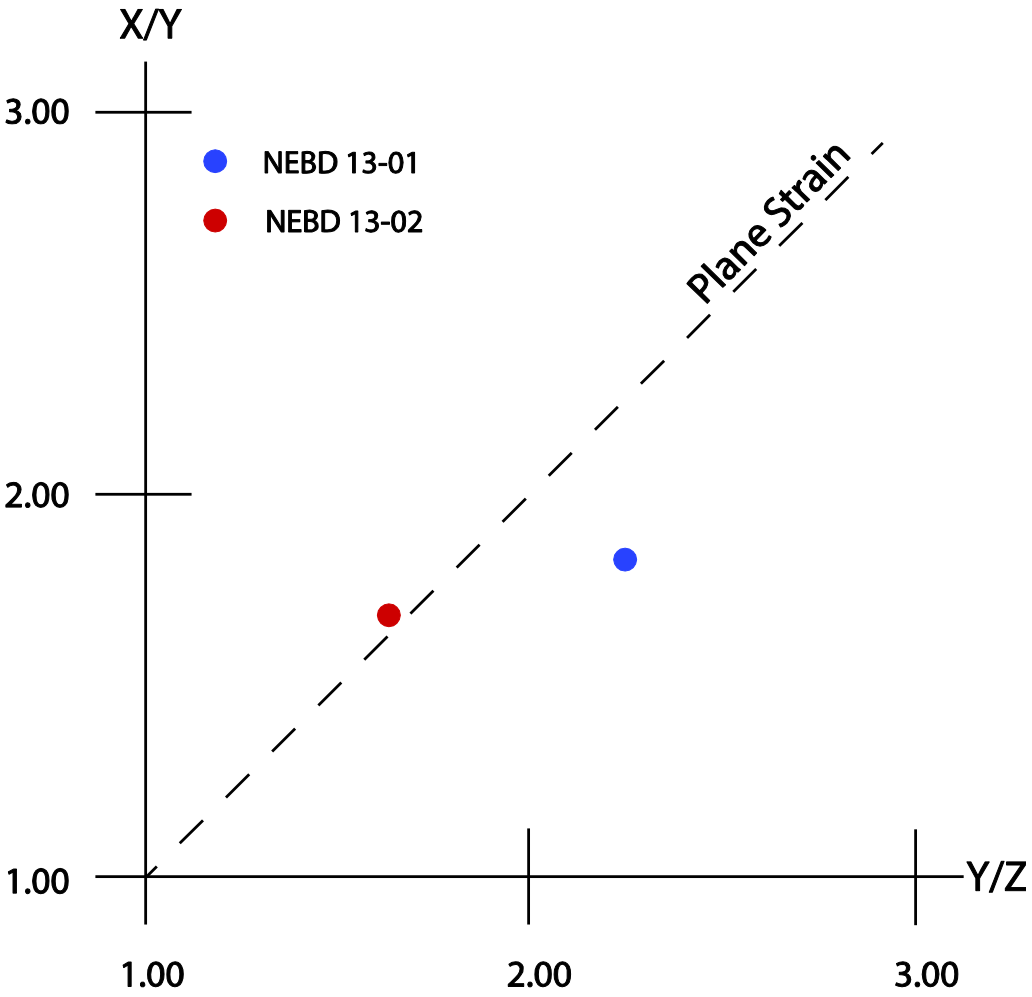


**Figure 27:** Flinn plots from folded and boudined vein data (assumptions discussed in text). Both stations show approximate plane strain as the dominant fabric.

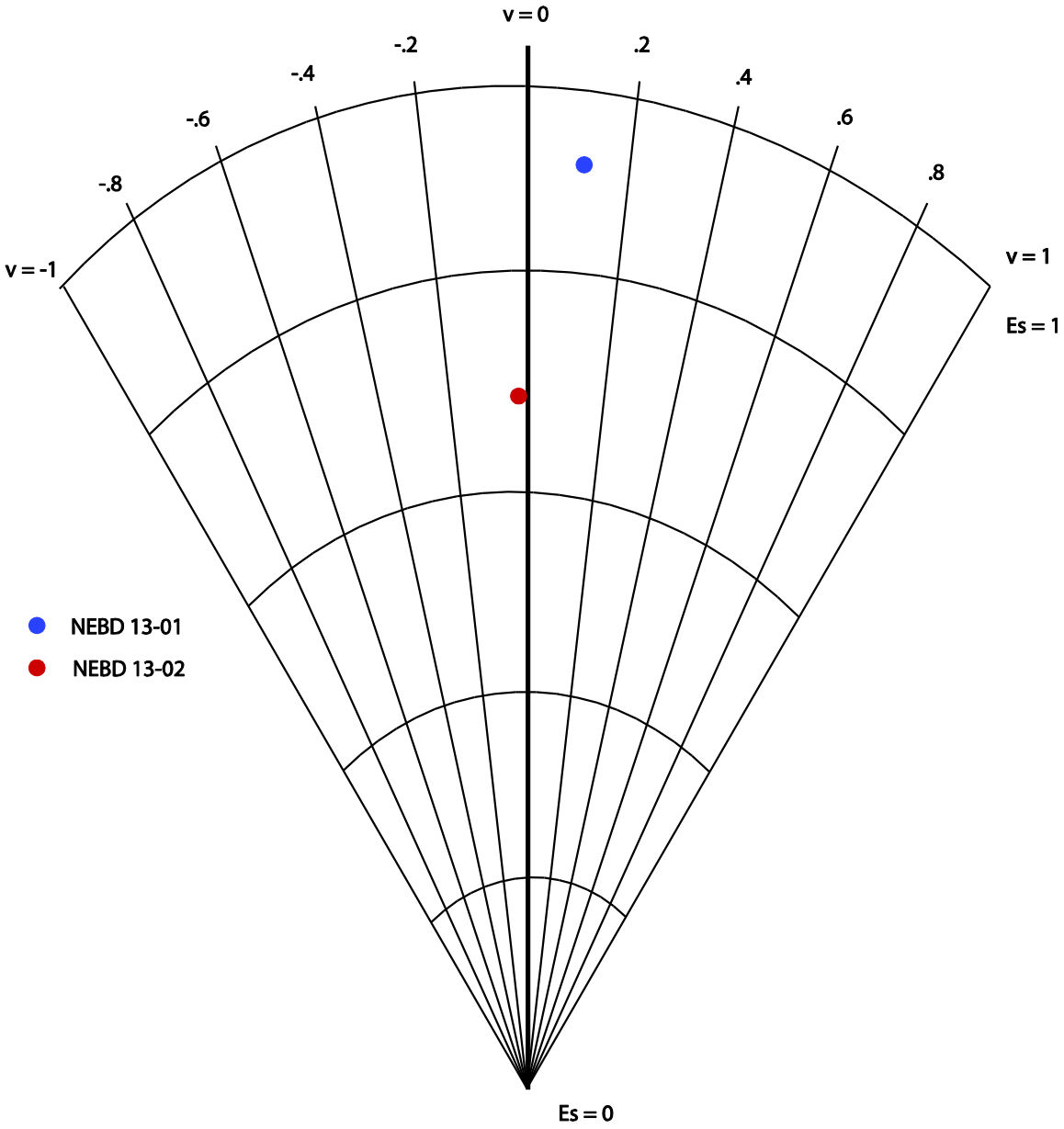


**Figure 28:** Hsu plot from folded and boudined vein data. Strain magnitude is considerably higher than that determined from mafic enclaves in the RBD.

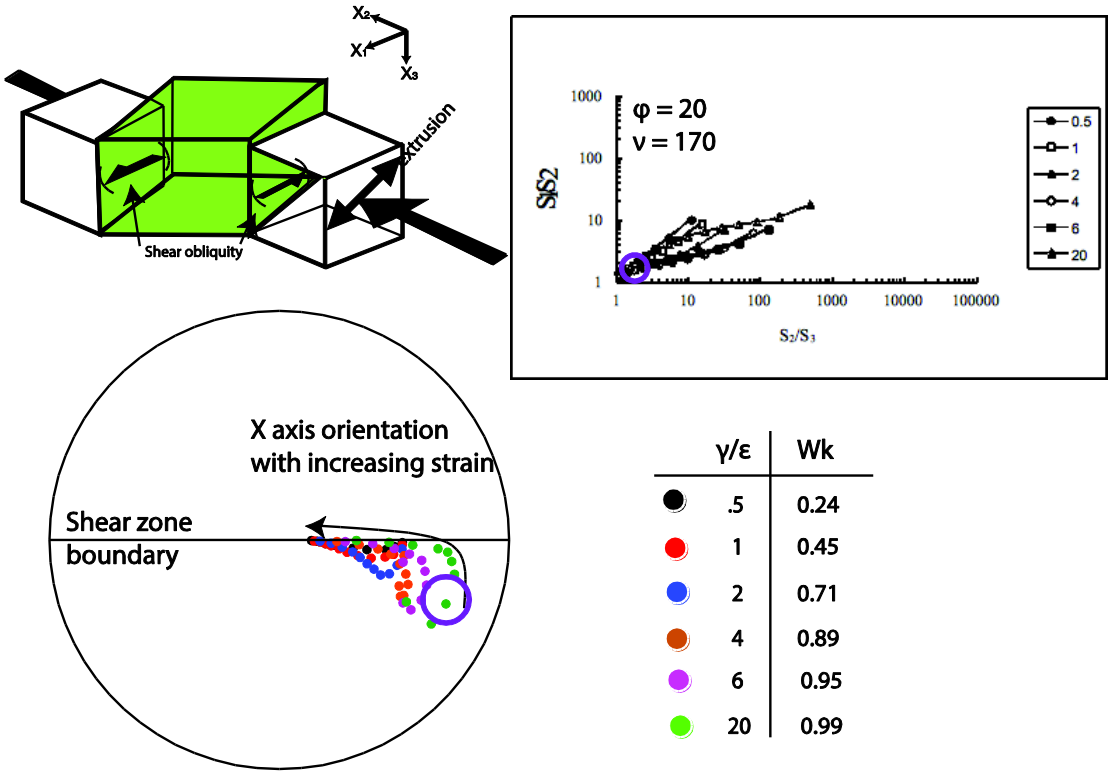


**Figure 29:** Example of transpression modeling and testing. For varying φ (shear obliquity) and ν (extrusion) (see top left corner) values, models were output (see Appendix A for full modeling output). The model shown is the output for φ = 20, ν = 170. The lineation orientations at each station are compared to X-axis orientations (Bottom left). Strain ellipsoid shapes are compared to Flinn plots (top right). Each colored dot represents a $\frac{\dot{\gamma}}{\dot{\varepsilon}}$ ratio, listed with its corresponding kinematic vorticity value (the ratio of simple to pure shear). An example for matching the data is shown here, from RBD 13-01. The lineation orientation (24°→122°), plus room for error, is shown in purple on the X-axis stereonet. The strain ellipsoid shape is also shown in purple on the Flinn plot. For this example station's data, this model is an acceptable match.

| Site | φ | ν | $W_k$ | Quality |
|---|---|---|---|---|
| RBD 13-17 | 20° E | 170° | 0.99 | Poor |
| NEBD 13-01 | 0° | 10° | 0.24-.71 | Good |
| | 0° | 170° | .24-.45 | Good |
| | 20° E | 0° | 0.24 | Poor |
| | 20° E | 10° | 0.71 | Poor |
| | 20° E | 170° | .24-.89 | Good |
| | 20° W | 10° | 0.24 | Poor |
| NEBD 13-02 | 0° | 10° | 0.24-.71 | Good |
| | 0° | 170° | .24-.71 | Good |
| | 20° E | 10° | 0.71 | Poor |
| | 20° E | 170° | .24-.89 | Good |
| | 20° W | 10° | 0.24 | Poor |

**Table 1:** Transpression modeling results for stations in both the NEBD and RBD. For full procedure and additional results, see Appendix A.

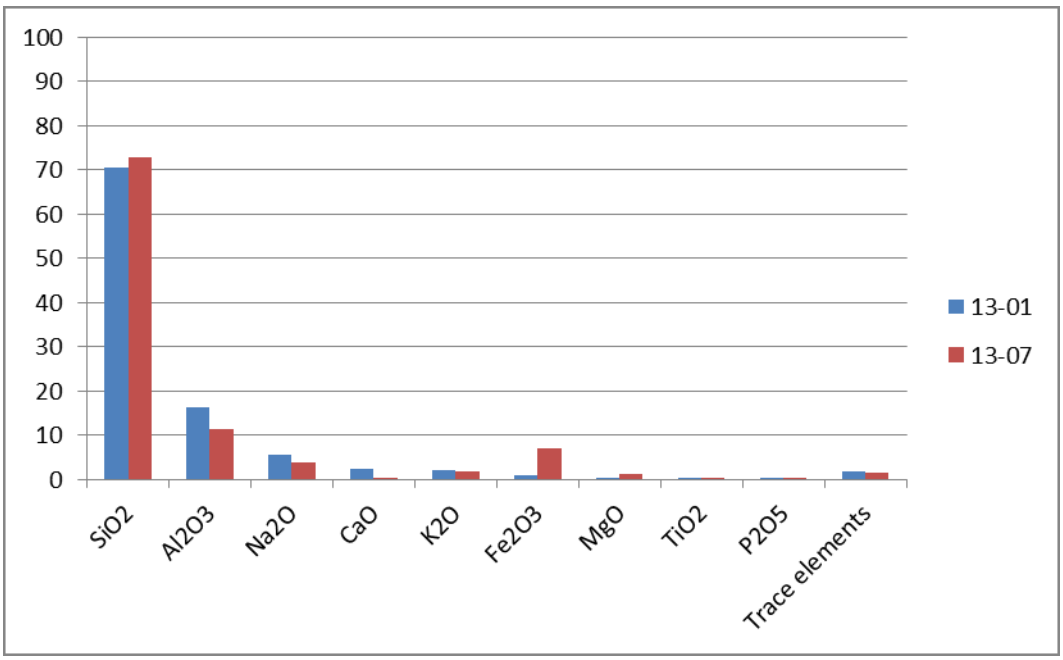


**Figure 30:** Major element geochemistry for the RBD.

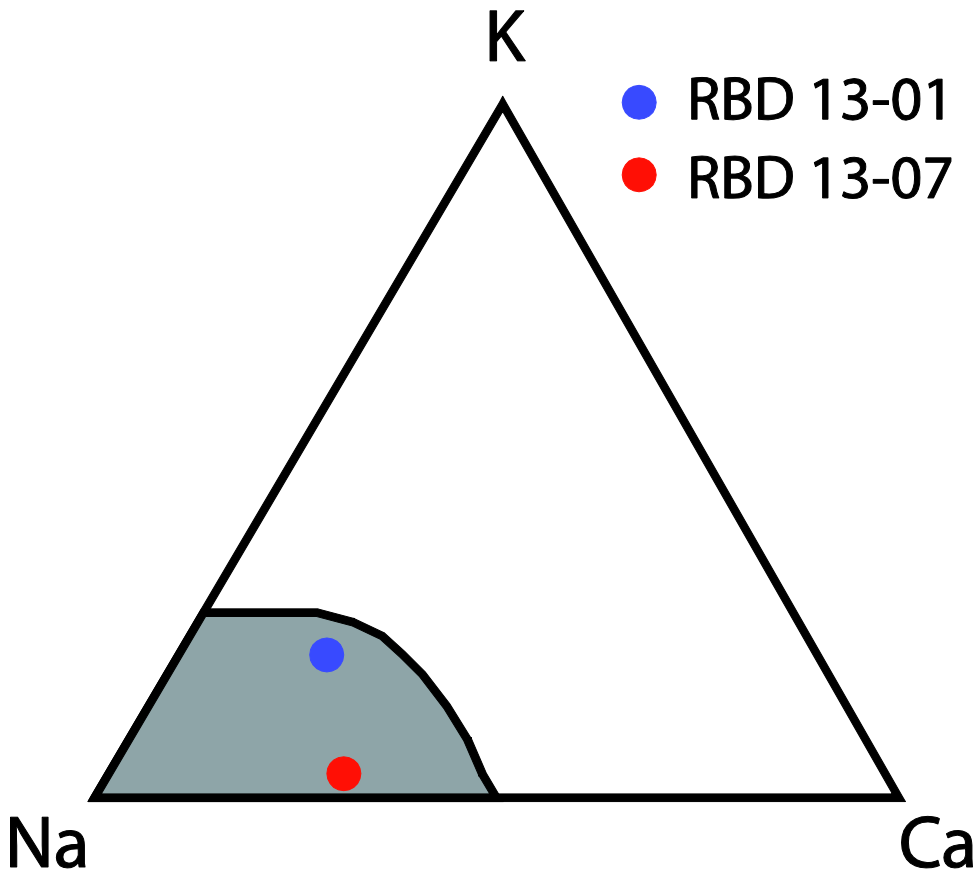


**Figure 31:** Ternary diagram representing bulk composition of the dome compared to Martin et al. (2005) data on the composition of Archean TTGs (shaded region). Both samples fall within the accepted boundary of Archean TTG composition.

| | RBD 13-01 | | RBD 13-07 | | Average Archean TTG (Condie 2003) |
|---|---|---|---|---|---|
| | Concentration | Error | Concentration | Error | |
| Na2O | 5.66% | 0.38% | 3.86% | 0.47% | 4.51% |
| MgO | 0.44% | 0.85% | 1.13% | 0.39% | 1.39% |
| Al2O3 | 16.19% | 0.22% | 11.48% | 0.26% | 15.50% |
| SiO2 | 70.47% | 0.13% | 72.74% | 0.13% | 68.30% |
| P2O5 | 0.05% | 4.04% | 0.04% | 5.61% | 0.14% |
| K2O | 1.99% | 0.18% | 1.79% | 0.19% | 2.20% |
| CaO | 2.31% | 0.18% | 0.25% | 0.70% | 3.26% |
| TiO2 | 0.14% | 1.22% | 0.26% | 1.70% | 0.42% |
| Fe2O3 | 0.91% | 0.88% | 7.07% | 0.29% | 3.42% |
| Br | 0.00% | 1.09% | 0.00% | 1.41% | *Not listed* |
| Y | *19.35 PPM* | 49.20% | 35.63 PPM | 8.27% | 9.1 PPM |
| Zr | 71.41 PPM | 3.35% | 509.78 PPM | 1.07% | 154 PPM |
| Nb | *5.51 PPM* | N/A | *33.95 PPM* | 24.00% | 6.2 PPM |
| V | *11.08 PPM* | 35.80% | *Not detected* | N/A | *Not listed* |
| Zn | 36.22 PPM | 11.70% | 104.77 PPM | 6.22% | *Not listed* |
| Ni | *2.96 PPM* | 10.10% | *10.43 PPM* | 10.30% | 22 PPM |
| Cr | *13.63 PPM* | 12.00% | *Not detected* | N/A | 35 PPM |
| Ce | *104.52 PPM* | 3.73% | *176.51 PPM* | 3.12% | 65 PPM |
| Sr | 725.50 PPM | 0.83% | *12.87 PPM* | 13.80% | 515 PPM |
| Ba | 792.14 PPM | 2.91% | 888.66 PPM | 2.57% | 796 PPM |
| Mn | 0.01% | 7.93% | 0.07% | 1.48% | 0.06% |

**Table 2**: XRF results for sample 13-01 (margin of RBD) and 13-07 (center of RBD). Concentration of oxides and trace elements shown. Elements and oxides with an error above 12% or concentrations below the lower detection limit highlighted in red. Each station is compared to the average Archean TTG composition (Condie 2003).

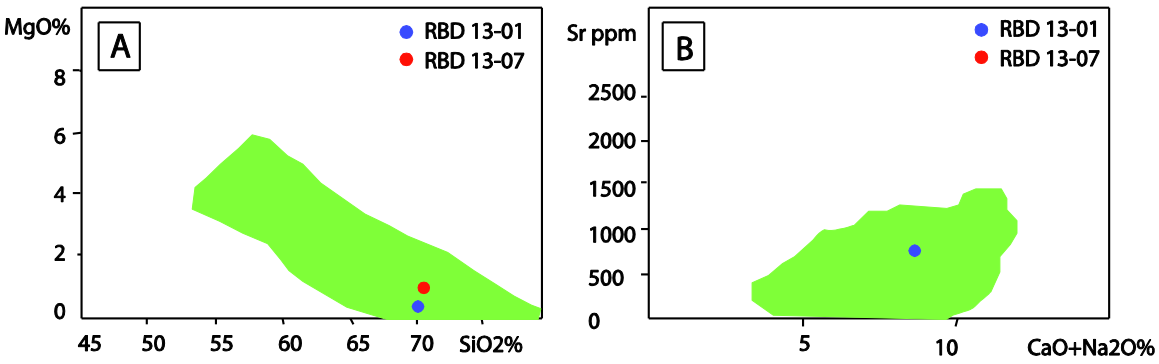


**Figure 32:** Trace element geochemistry compared to Martin et al. (2005) study of Archean TTG trace elements (fields plotted in green). These fields show the range of compositions of several samples of Archean TTG suites. The composition of RBD 13-01 fits well within the boundary of the Archean TTG, but not as much useful information could be obtained from RBD 13-07 due to high errors in measurement.

# Chapter 5: Interpretations

*5.1: Foliations & Lineations*

Foliations and lineations (where available) were distributed throughout the RBD and appear to fold over an apparent axial trace (Figure 11). Foliations strike roughly ENE-WSW and dip moderately to steeply. The general foliation pattern seems to be folded into an antiform about an axis of ~070. There are not as many data constraining the foliation pattern in the central part of the RBD, but it is possible that there are additional complexities to the folding within the central RBD. The axial trace that these foliations fold over is likely a large scale $D_2$ fold hinge based on the upright nature of the fold and the fold axis orientation (Poulsen 2000). This suggests that the pervasive gneissic fabric present within the RBD is attributed to $D_1$ or early $D_2$, and the observed foliation pattern is strictly a deformational one. The lineations observed in the RBD plunge shallowly either ENE or WSW. Their orientations are consistent with stretching along the presumed fold hinge of the dome.

Foliations within the NEBD are more limited in quantity, but show a synformal structure (Figure 12). The limited number and spatial extent of outcrops combined with the poor exposure of foliation planes in the NEBD make the interpretation of this synformal structure merely speculative.

Lineation patterns may be useful in determining the emplacement mechanism of the dome. If lineations radiate away from the central portions of the RBD, then a diapiric flow is a likely emplacement mechanism (Whitney et al. 2004). Channel flow is also a possible mechanism for dome emplacement, and would produce horizontal fabrics

(Whitney et al. 2004). Combinations of vertical and lateral flow can also produce gneiss domes, and will leave structures such as climbing folds and cascading folds on their flanks, depending on the degree of vertical motion (Whitney et al. 2004). As shown on Figure 11, the lineations in the RBD are not radially plunging away from the center of the dome, but are fairly consistent with ENE or WSW trend and shallowly plunging throughout. The regional lineations vary widely within and across lithological units (Czeck & Hudleston 2003), so the orientation of the lineations here cannot be used to conclusive determine whether they are related to emplacement or deformation. However, it seems likely that since 1) the same mineral (biotite) is forming the foliation and 2) the foliation is demonstrably deformational, then it is likely that the lineation is formed during deformation as well. Therefore, unfortunately we cannot use the lineations as a means to interpret the emplacement mechanism of the RBD. These lineations are likely deformational, and will only be useful in determining the style of deformation.

In both the RBD and NEBD, foliation fabrics are dominant over lineation fabrics ($S > L$). The dominance of foliations suggests that flattening fabrics are dominant. Lineations were formed by elongated biotite (usually) and quartz (rarely) grains. Biotite is a poor lineation marker, so lineations may not have formed as readily as the foliations. If minerals with a more prolate crystal shape were present in the rock, such as amphibole, perhaps lineations would be more prominent. Field observation and XRD analysis indicate that no amphibole is present in the units. Some combination of the two possible causes (strain shape and/or mineralogy) for the dominance of foliation is at work.

*5.2: Shear Zones*

Shear zones were more commonly found at the center of the RBD. The highest quantity of shear zones in the dome were found at RBD 13-07 (Figure 16). Within the RBD as a whole, 69% of shear zones observed were of dextral sense, and 31% were of sinistral sense (Figure 13a). The same approximate proportions of dextral to sinistral shear zones were also observed at RBD 13-07, which suggests RBD 13-07 can be used as a proxy for strain conditions for the whole dome.

The shear zones at RBD 13-07 likely formed as sets at high angles to each other, and rotated towards parallelism with increasing deformation (e.g. Carreras et al. 2010), indicating that bulk shortening is accommodated in the RBD along these discrete shear zones. Sets of sinistral and dextral shear zones can work together to accommodate shortening; as shortening occurs, one set of synthetic and one set of antithetic fractures or shear zones (Reidel shears) form at roughly 90° to each other bisected by the shortening direction (Figure 33) and rotate away from the shortening direction in opposite directions with progressive deformation (Ramsay & Huber 1987; Mancktelow 2002; Carreras et al. 2010). In this model, dextral sets rotate counter-clockwise and sinistral sets rotate clockwise making the angle bisected by the shortening direction larger with increasing deformation. This process is likely occurring here in the RBD. Generally, the accepted shortening direction for the entire region is roughly N-S (Poulsen 2000, Carreras et al. 2010). In this detailed outcrop, we see an orientation consistent with that direction (Figure 33). Both early and late shear zones have very similar orientations, indicating that the shear zones formed without a significant time interval between the early and late

sets, or there were not enough shear zones at the outcrop to determine a sense of rotation between early (thicker) shear zones and later (thinner) shear zones (Figure 33).

Dextral shear zones outnumbered sinistral shear zones at this outcrop (70% dextral, 30% sinistral). If the dome were accommodating only shortening, then sinistral and dextral shear zones would be found in equal abundances. The RBD is therefore likely accommodating a significant amount of dextral motion along with the shortening during the large transpressive event.

Shear zones were uniformly spread throughout the areas accessible in the NEBD (Figure 15). In contrast to the RBD, all shear zones observed displayed dextral motion (Figure 13b). No conjugate sets of shear zones were observed, suggesting that the NEBD is accommodating mainly the shear component of transpression.

The shear zones in the RBD are excellent targets for gold mineralization. No current mining is occurring in the RBD, but veins in tonalitic and metagabbroic units to the east (near Mine Centre, ON) have been developed for gold production (Poulsen 2000). The abundance of quartz veins along the shear zones at station 13-07 indicate significant amounts of localized fluid transport during deformation, and are typically associated with gold deposits. The gold bearing veins near Mine Centre show many of the same features visible at RBD 13-07. Those shear zones occur in conjugate sets of steeply dipping dextral and sinistral shears, and the quartz veins associated with gold mineralization typically form in the center of the shear zones.

*5.3: Tension gashes and quartz veins*

Tension gashes are distributed somewhat evenly throughout the RBD and NEBD (Figures 17 & 19). However, tension gashes appear to be more abundant along the southern edge of the RBD. The southern edge of the RBD also is the only area to host the iron-rich tension gashes. Quartz and K-feldspar tension gashes are much more uniformly spread throughout the dome and occur in the same outcrops. In the NEBD, no iron-rich tension gashes occur, but quartz and K-feldspar tension gashes occur frequently and in the same outcrops.

Quartz tension gashes were the most abundant group in both domes. Each group of tension gashes in the RBD (quartz, K-feldspar, Fe-rich, and quartz + K-feldspar) yields a slightly different orientation of extensional stress ($\sigma_3$). The average orientation of extension from the quartz tension gashes is approximately 90 degrees from the average orientation of extension from the K-feldspar tension gashes. The extension direction suggested from the quartz tension gashes is approximately E-W (about 275), while the K-feldspar tension gashes suggest an extension direction of approximately N-S. The Fe-rich tension gashes also indicate a slightly different extensional direction. These tension gashes display a bimodal distribution, suggesting two stages of tension gash emplacement. One set of the tension gashes is rotated almost parallel with the shear plane, while the other is almost perpendicular to it. The set of tension gashes perpendicular to the shear plane is likely the later set, and indicates extension was occurring in the N-S direction. This suggests that as exhumation and emplacement of tension gashes was occurring, rotation and late deformation were also occurring within the dome.

It is not possible from the field data present to conclusively determine which tension gashes occurred first, as no cross-cutting features of tension gashes were observed. However, some interpretations of timing can be made from the rotation of tension gashes. In an ideal world, tension gashes would open perpendicular to the envelope (indicating the least compressive stress). During dextral simple shear dominated deformation, tension gashes would open and rotate clockwise. During pure shear dominated deformation, tension gashes would rotate either clockwise or counterclockwise, depending on the initial orientation of the tension gash, which should vary only slightly in either direction from the shear plane normal. In a transpressional setting, tension gashes could rotate either way, depending on whether simple shear or pure shear is dominant. In all cases, tension gashes rotate towards being parallel with the shear zone with increasing strain.

From the above assumptions, the quartz and K-feldspar tension gashes are the oldest, based on their orientations. They have been rotated to an orientation parallel with the strike of the shear plane. It is likely that the quartz tension gashes have been emplaced at various times during late stage deformation, and rotated counterclockwise progressively towards being parallel with the shear plane (E-W). One cluster of quartz tension gashes is oriented in this direction. The iron-rich tension gashes were emplaced in two different phases, as they display a bimodal distribution. One set was emplaced early, and had been rotated, while the other set did not rotate as much prior to the conclusion of deformation. The age of the K-feldspar tension gashes is unknown, but is likely older (due to the high temperature needed to emplace K-feldspar). These K-feldspar tension gashes may be controlled by layering in the dome.

In the NEBD, a similar relationship between quartz and K-feldspar tension gashes was observed. However, here the K-feldspar tension gashes indicate extension in the NW-SE direction, while quartz indicates extension in the NE-SW direction. These quartz tension gashes may have been emplaced throughout late stage deformation, and were progressively rotated to their present orientations. In the NEBD, it is likely that the K-feldspar tension gashes are older, as they are close to parallel with the shear plane. This difference between the two domes indicates that the stress field during late stage exhumation may not have been consistent across the whole area, or that the tension gashes were not emplaced at the same time in both domes.

Planar quartz veins are more prominent along the southern edge of the RBD as well. No quartz veins were visible in the northern outcrops (Figure 21). These veins were emplaced during the late stages of deformation and likely record a small incremental strain, so can be used to interpret the local stress field at the time of emplacement. The late stage quartz veins largely parallel the foliation planes, which suggests that the veins intrude along local planes of weakness. This orientation supports the idea that the quartz veins formed in a late stage deformation, after the rocks had already developed a strong foliation. That foliation caused a strong mechanical boundary, which caused the local stress field to differ from the regional stress field. Veins here may be associated with mineralization, as cubic minerals (potentially pyrite or a copper alloy) had been weathered out from one of the quartz veins (figure 34). No quartz veins were found in the NEBD which may be due to lack of quartz rich fluids present during late stage deformation, the lack of strong mechanical contrasts formed on foliation planes, or lack of exposure causing the veins to remain unobserved.

*5.4: Mafic Enclave data*

Mafic enclaves were present mainly along the southern edge of the RBD at stations 13-01, 13-11 and 13-17. These three stations lie very close to a major contact with metavolcanic schists. It is possible that the mafic enclaves are actually xenoliths from the schists incorporated into the dome during emplacement. Alternatively, these enclaves could be due to various magmatic processes, but further analysis is necessary to test this.

Flinn plots for the three stations on the map are shown in Figure 23. There were not mafic enclaves present in the NEBD. From the Flinn diagrams of mafic enclave data in the RBD (Figure 24), we see each outcrop fall into a different strain regime. RBD 13-01 appears to display plane strain to flattening fabrics, RBD 13-11 displays stronger flattening fabrics, and RBD 13-17 displays plane strain or constriction fabrics (but with more error). Upon examination of the Hsu plot (Figure 25), each station appears to show low strain. RBD 13-11 has the highest strain magnitude of the three outcrops with a maximum $\varepsilon_s$ value of 0.77, and an average $\varepsilon_s$ s value of 0.57. The lowest strain magnitude is found at RBD 13-01 with an average $\varepsilon_s$ value of 0.06.

These strain magnitudes from mafic enclave strain markers must be considered carefully, as mafic enclaves may not track finite strain (Paterson et al. 2004). Mafic enclaves vary so greatly in size and shape that they may not properly record strain. The starting axial ratio of many mafic enclaves is skewed to be ellipsoidal (1.1-2.7, from Paterson et al. 2004), and therefore may be a large source of error in assigning strain magnitudes (Paterson et al. 2004). Depending on the orientation of the mafic enclaves

prior to deformation and the orientation of strain, an initial preferred orientation may have the effect of causing either an overestimate or underestimate of strain. This error is diminished and even eliminated if the enclaves are randomly oriented prior to deformation and a large sample size is measured. Unfortunately, the nature of the mafic enclaves in these rocks precluded a large sample set. However, the Rf/Phi method should be able to determine whether there was a strong preferred alignment of ellipsoidal markers (Lisle, 1985). The program used here to conduct Rf/Phi analysis (Yonkee et al. 2013) estimated the original preferred orientation factor for these mafic enclaves with the shape ellipsoid of Ri = 1.0-2.0 . So therefore, the preferred orientation was likely not a major factor. Another issue with mafic enclaves is that they are likely to have a rheology contrast with the rest of the rock so that strain analysis records the strain of the enclaves rather than the host rock. In this case, the mafic enclaves were likely less competent than their host rock gneiss, so the strain analysis of the mafic enclaves should be an estimate of the maximum strain in the gneiss.

The strain magnitudes found for the RBD are similar to those found by Druguet et al. (2008). In particular, the RBD strain estimate matches that of the strain estimates from folded and boudined veins near the margin of the RBD. The results of Druguet et al. (2008) also determined that plane strain with slight local perturbations was the dominant fabric. However, the strain results from localities away from the RBD show significantly higher flattening strain. Compared to the results of Czeck et al. (2009) (a study of the Seine metaconglomerates), the RBD exhibits significantly different strain ellipsoid shapes. The metaconglomerates display mainly flattening fabrics, with some

local constriction fabrics. The strain magnitudes of this unit are also considerably higher than the strain magnitude observed in the RBD.

The low strain magnitudes of all stations analyzed in the RBD indicate that the gneiss is highly competent, and did not accumulate as much strain as its neighboring metasedimentary units. It is possible that the center portion of the dome accommodated a higher amount of strain than the rim, but this was not possible to test as there were no mafic enclaves found in the center. The dominance of flattening fabrics and the low strain nature of the area are the most likely reasons that lineations do not form easily.

The foliation poles tend to match the Z axis of the strain ellipsoid, with the exception of 2 runs (one from RBD 13-01, one from RBD 13-17). The lineation orientations were also generally consistent with the X axis orientations.

*5.5: Folded and Boudined Dikes and Veins data*

There were very few folded veins present within the RBD. The only stations yielding significant quantities of folds or boudins were just outside of the dome, likely on the outer boundary of the gneiss and schist, RBD 13-12 and 13-13. Three folds were present at the island outcrop of RBD 13-21, but analysis was not possible, as EllipseFit requires four or more structures to accurately constrain the ellipse.

The NEBD had many more dikes and veins containing folds and boudins. NEBD 13-01 and 13-02 yielded a significant amount of folds for analysis, nine and five (respectively). Folds and boudins found at two stations within the NEBD yielded similar strain ellipses. Each ellipse was oriented with its long axis trending roughly N75E -

N80E (Figure 26). This maximum elongation direction is consistent with the strike of the foliations in the area, along with the general orientation of the Quetico shear zone to the north.

The 3D strain ellipsoids for the two stations are consistent with the overall strain ellipse from just outside the NEBD (Druguet et al. 2008). The folded and boudined veins intersected the foliations of the region at low angles in the NEBD, similar to how they do in the surrounding schists. Figure 35, modified from Druguet et al. (2008), shows orientations of shortened and extended veins from areas around the RBD and NEBD, but no data was plotted for within the NEBD. The slight flattening fabric is consistent with the overall strain regime of the area and the lack of lineations found at the outcrops. Lineations from the NEBD are inferred to be vertical, as the strain ellipsoid shows the YZ plane on the horizontal outcrop. Although this is different from the RBD, it is not entirely impossible. The RBD and NEBD are likely accommodating deformation in different styles, and the NEBD may be experiencing a greater component of pure shear (Fossen & Tikoff, 1993).

It is important to note that these folds do not always record all the strain a unit has undergone, as veins are often emplaced later in deformation. Therefore, these folded veins may only be recording part of the strain path that was undertaken by the NEBD and therefore should be considered a minimum strain estimate for the gneiss.

*5.5: Transpression modeling*

In the RBD, eight stations had lineation data and could be compared to the models. For some stations (RBD 13-05, 13-10, 13-16) multiple models of varying shear

obliquity and extrusion fit. Most of these models were matches for the data at higher kinematic vorticity ($W_k$ = 0.89-0.99) (Appendix A).

Once strained mafic enclave data was included one consistent model of $\varphi = 20°$ and $\nu = 170°$ was a close fit for much of the data in the RBD. This model was a perfect match for station 13-17, and was a close match (save for the 2D sectional ellipses) for station 13-01, but did not fit station 13-11 (due to angle of elongation incompatibility). The Rs values were close matches, but the angle of elongation was not a good fit for the data, and was off by more than 30 degrees. Simple shear obliquity is present and occurs at a low angle. The extrusion angle for this model is subvertical ($\nu$ =170°). The strain magnitude for these models is low (Lode's ratio typically less than 0.3; Figure 25), indicating that they were not on this strain path for a considerable amount of time. The kinematic vorticity determined from this model was high and close to 1, indicating a high ratio of simple shear to pure shear ($W_k$ = 0.99). This kinematic vorticity estimate seems to be too high for the rest of the study area, given that shortening has been observed in the center of the dome (at station RBD 13-07). The RBD may be partitioning the strain differently within itself, however. The outer edge of the dome may yield vastly different strain magnitudes than the center of the dome.

This model is also a match for some of the stations lacking strain data. The lineation data at RBD 13-04 and 13-05 also fit this model at high kinematic vorticity ($W_k$ = 0.99). This suggests that this model is a reasonable model for the other stations in the RBD, as it agrees with five out of eight stations.

In the NEBD, several models were possible. There was no one single simple shear obliquity angle that worked for the assumed lineation orientation; models with φ of 160°, 0°, and 20° were all possible. Angles of extrusion, ν, were subvertical (0°, 10°, 170°), consistent with the assumed vertical to subvertical lineations. For the NEBD, the transpression modeling yielded lower kinematic vorticities (0.24-0.89, with considerable variation), indicating that there was a considerable amount of pure shear, and pure shear may have been more prominent in this dome. The data fit the models at low to medium strain magnitudes. It is not possible at this time to further narrow down the number of working models without additional field data to constrain the models. Based on field observations, these models should hold for all outcrops observed during this field study. No significant changes in foliation or fabric were observed, suggesting that this central portion of the dome behaved similarly. However, conclusions cannot be drawn for the margin of the NEBD due to a lack of direct observation.

The best-fit models for both domes are quite similar, despite the vastly different lineation orientations. This is likely because of the positions along the strain path that each lineation represents. These models also accommodate plane strain, which is dominant in both domes, for positions towards the beginning of the strain path. All parts of the RBD model (lineation data, 2D horizontal ellipses, and strain ellipsoid shape) agree for lower amounts of finite strain, while the NEBD has a major discrepancy between the lineation data and the other parts of the model. The assumed lineation data matches the model at high amounts of strain, while the 2D ellipse and 3D ellipsoid shape data matches the model at lower amounts of strain. It may be likely that the lineation direction in the NEBD is actually steeply plunging, rather than subvertical, as well. If the

NEBD is in fact dominated by pure shear, a steep subvertical lineation is expected, as lineations formed through pure shear are vertical. Lineations formed by simple shear, on the other hand, begin subhorizontally and progressively rotate towards vertical with increasing finite strain (Fossen & Tikoff 1993, Czeck & Hudleston 2003). Lineations from the NEBD match the pure shear dominant model, while lineations in the RBD match the simple shear dominant model.

The strongest parts of these models are the shear obliquity and extrusion angles. Both domes had very similar models fit them, indicating that these models are likely the best options.

However, the kinematic vorticity values are still points of uncertainty. The mafic enclave data may be an overestimation of strain, or the mafic enclaves could have a preexisting shape (meaning they had a primary preferred orientation), which could be a source of error for the modeling. Because shortening was clearly observed in other areas of the RBD, it is unlikely that this unit deformed through only simple shear. Likewise, in the NEBD, the dominance of dextral shear markers seems to indicate that simple shear played an immense role in deformation, but the models suggest that pure shear was actually dominant. More modeling and testing would be necessary to conclusively state the kinematic vorticities possible for these domes.

*5.6: Kinematics and strain partitioning of the gneiss domes*

All structures observed can be incorporated into a larger scale kinematic model for the domes. Most structures observed can be attributed to $D_2$ deformation, as the domes were emplaced at some point during $D_1$. Foliations of the RBD define an axial

trace produced during $D_2$ folding, as the $D_1$ axial trace is likely buried (Poulsen 2000). Lineations are also likely $D_2$ features. Lineations and cascading folds are some of the few structural features that can be used to determine emplacement mechanisms of gneiss domes. Radial emplacement lineations plunging away from the center of the dome would indicate diapiric emplacement. Unfortunately, in the RBD, all lineations present are deformational and cannot be used to determine emplacement.

In the RBD, most localized strain has accumulated in the central portion of the dome. This is marked by an abundance of shear zones and the increased presence of folds. The outer edge of the dome appears to be deformed more homogeneously as determined by the lack of shear zones, but deformation marked by the mafic enclaves. Tension gashes and quartz veins are also observed along the outer edge of the RBD, but these are late stage ($D_3$) features and have little to do with the main deformational event, $D_2$. From the limited sampling of the NEBD, it appears that the shear zones, folds and boudins are abundant throughout the dome. To confirm this, additional sampling would be required throughout.

Shear zones are prominent features in both domes. These features likely formed during the main transpressional event, $D_2$. In the RBD, obvious sinistral and dextral sets of shear zones accommodate shortening. Shear zones in the RBD also vary in size, from very small (less than half a centimeter) to large (greater than 10 centimeters) in width. In general, dextral shear zones have a greater width than sinistral shear zones. In the NEBD, only dextral shear zones were observed. These shear zones were small, but very abundant in outcrops. The conjugate shear zones in the RBD can be directly linked to

accommodating shortening and the dominance of dextral over sinistral sets indicate that a significant part of the dextral deformation was taken up on shear zones too.

Strain cannot generally be measured within the domes, but can be approximated in some locations using mafic enclaves in the RBD and folded/boudined dikes and veins in the NEBD. The mafic enclave strain data from the RBD is likely an overestimate of the overall strain in the gneiss because the enclaves are less competent than the gneiss. The strain data from the folded/boudined dikes in the NEBD is likely an underestimate of strain within the gneiss because 1) the veins and dikes were emplaced during $D_2$ deformation so they only record part of the strain, and 2) the veins and dikes are more competent than the rest of the gneiss. The strain magnitudes from both domes are similar, but the NEBD appears to be more strained than the RBD, and this disparity is only heightened by the likely overestimate of strain in the RBD and underestimate of strain in the NEBD. For these reasons, the gap between the NEBD and RBD strain magnitudes is likely slightly larger than observed.

The strain within both domes indicate a plane strain or, in some cases, flattening deformation. In both domes, the shortening was roughly N-S. In the RBD, the mafic enclaves strain data corroborates the conclusion from the subhorizontal lineations that stretching is subhorizontal in a roughly EW direction. In the NEBD, the presumed lineations are subvertical suggesting a vertical stretch.

Both units were likely accommodating both dextral motion and shortening, but were accommodating the strain in different ways. The RBD partitioned deformation along discrete shear zones for both the shortening component (conjugate sets) and the

dextral component (dominance of dextral shear strands) of the transpression. From the mafic enclave data, it seems that a significant amount of deformation was also accommodated within the main part of the RBD gneiss itself. Since the most likely $W_k$ was high and the lineations are subhorizontal, it seems like the main part of the gneiss was simple shear dominated. The NEBD likely accommodated a great deal of dextral strain along several small, localized shear zones, and the proximity to the Quetico Fault is likely the cause of this dominant dextral deformation. However, the presumed vertical lineations and the lower strain within the gneiss itself suggest that the main part of the gneiss within the NEBD accommodated more of the pure shear shortening component of the transpression. This scenario, where the discrete shear zones take up most of the strike-slip deformation and the lozenges between the shear zones accommodate little to no deformation or most of the shortening is hypothesized to be the most general case (e.g. Burg 1999; Butler et al. 2002), so it is interesting that the data support this interpretation for the NEBD but not for the RBD.

Based on the structures observed, it is likely that N-S shortening was occurring along with dextral strike-slip motion during $D_2$. The shear zones present in both domes strike roughly E-W, and the shortening direction is roughly perpendicular to that orientation due to continued rotation of the shear zones throughout deformation (Figure 33).

During the final stage of deformation, localized extension was recorded by late stage tension gashes. Each set of tension gashes has been emplaced and then rotated to the current orientation during late stage exhumation. In the RBD, quartz, K-feldspar, and

iron-rich tension gashes have intruded in multiple stages and rotated towards the shear plane with continued deformation. Tension gashes with a composite quartz and K-feldspar fill likely formed first, with quartz tension gashes occurring second. The timing of the K-feldspar tension gashes is unknown, due to the random orientation and no preferential orientation. The iron-rich tension gashes only occurred in one locality, and indicate two stages of emplacement, potentially coeval with the quartz tension gash emplacement. These iron-rich tension gashes were not observed anywhere else, and may be indicating mineral rich fluids were present during exhumation.

In the NEBD, we see similar relationships of tension gashes, but it appears the K-feldspar tension gashes intruded first, followed by quartz tension gashes. This indicates that tension gashes of varying fill may not have been coeval in both domes. Additionally, mineralization may not be as prominent in the NEBD as it is in the RBD. The tension gash orientations in the NEBD yielded inconclusive results. Two stations matched the orientation of the late stage stress field of the RBD, but one did not. More sampling points would be needed to fully constrain the extensional direction in the NEBD. The rotational component to these tension gashes indicates that the late stage deformation was largely noncoaxial.

These results are consistent with triclinic transpressional models proposed for the area. Only one model matched the strain data for the RBD, and was consistent across all stations with both lineation and strain data. This model ($\varphi = 20°$, $\nu = 170°$) invokes a shallow shear obliquity angle and a subvertical extrusion angle. This model also suggests that the RBD has not accumulated a considerable amount of strain, and deformed with

greater components of simple shear to pure shear. Coupled with the mafic enclave results indicating plane strain, this model suggests that simple shear is far more dominant over pure shear here (consistent with the subhorizontal lineations).

The NEBD has considerably more potential models which match the field data, one of which is the model that also matches the RBD. All models for the NEBD invoke low shear obliquity angles and subvertical to vertical extrusion angles. The data alignment with the models also suggests that the NEBD has accumulated more strain than the neighboring RBD. Despite its proximity to the large scale Quetico shear zone, the model predicts pure shear to be dominant in the NEBD (consistent with the subvertical lineations), but still with a considerable component of simple shear. This pure shear component is likely accommodated in the rock of the NEBD itself, while the dextral motion is accommodated in small shear zones.

Although these transpressional models work for the competent rock units, it is unlikely that they work for the other lithologies of the Rainy Lake area. Each lithology deforms in its own way and produces its own distinct set of structures. Although all units underwent the same large scale tectonic event during the Neo-Archean, each unit accommodated strain differently. Therefore, there is no single transpressional model that can fit the entire Rainy Lake wedge.

### *5.7 Comparisons of kinematics and strain to other lithological units within the Rainy Lake zone*

Several other researchers have studied different units of the Rainy Lake area to determine kinematics and strain partitioning. In the metagabbros nearby the RBD,

kinematics were determined from anastomosing shear zones (Carreras et al. 2010). These anastomosing shear zones are similar to those found within the RBD, and show a preference for dextral shear zones over sinistral. The dominance of one shear zone sense over the other indicates noncoaxial deformation. If the dextral shear zones outlasted the sinistral ones, which is hard to discern from the data here except through conjecture about shear zone thickness, the results are consistent with a tectonic model shifting from pure shear dominated deformation ($W_k = 0$) to simple shear dominated deformation ($W_k = 1$) similar to that found in the metagrabbros (Carreras et al. 2010). Coupled with the transpression modeling done for the RBD which indicates simple shear being dominant (high $W_k$), it is implied that the shear zones in the RBD formed in a similar strain regime as the shear zones from Carreras et al. (2010).

Folded and boudined leucocratic veins are abundant in the metavolcanic and metasedimentary schists surrounding the RBD (Druguet et al. 2008). These folds indicate stretching in a roughly E-W direction, as evidenced by the abundance of boudins in that orientation. An estimate of kinematic vorticity was also proposed for two of the sampling locations. The $W_k$ values for these locations indicate dominant pure shear with a component of simple shear (Druguet et al. 2008). Similar $D_2$ folds and boudins are also present in the NEBD. These folds and boudins are similar in orientation to the surrounding structures contained in the schists. From the criteria for high strain versus low strain zone classification set out by Druguet et al. 2008, the fold and boudin data indicate that the NEBD was a high strain zone because folds and boudins occur at low angles to the $S_2$ foliation (Druguet et al. 2008). The kinematic vorticity values ($W_k = 0.6$-$0.7$) proposed by Druguet et al. (2008) do not align with the preferred models for the

RBD, but do match the preferred models for the NEBD. This may be a reflection of the portion of deformation that the folds and boudins recorded, as folded and boudined veins were intruded during deformation: they are likely underestimates of strain and perhaps capture part of the strain history with different $W_k$ ($W_k$ did not necessarily remain constant throughout deformation). Alternatively, it is possible that the different pure shear and simple shear were partitioned differently within the different rock units.

The strain magnitudes for the NEBD and RBD are lower than those calculated for the schists (Druguet et al. 2008) (Table 3). However, it is important to note that strain magnitudes and ellipsoid shapes of the schists nearby the RBD are similar to those found in the gneisses. This may be due in part to a "strain shadow" effect that the gneisses are having on the softer schists, altering their deformation by deflecting strain around them. The further away from the RBD and NEBD traveled, the more flattening fabrics are present (Druguet et al. 2008).

This study has utilized the same methodology as Fernández et al. (2013) to estimate transpression conditions. Fernández et al. (2013) used the Seine metaconglomerates as an example case for this protocol. The Seine metaconglomerates display obliquely plunging lineations similar to those observed in the RBD, but generally with a much steeper plunge (Czeck & Hudleston 2003). The results for the transpression modeling of the metaconglomerates show that while shear obliquity angles were relatively constant between 0-20° east or west, extrusion direction and Wk varied significantly throughout the unit. Extrusion orientations were moderately to steeply plunging between 40° either east or west and vertical and kinematic vorticity values

varied between 0.35-0.95 (Fernández et al. 2013). This scenario is certainly not consistent with the models obtained for the RBD and NEBD, where there may be some variability, but where model matches can be found, generally speaking, the models have consistent subvertical extrusion orientations and kinematic vorticity does not vary much within an individual dome. The RBD and NEBD may have acted as more cohesive units, or may not have experienced as many local strain perturbations as the Seine metaconglomerates.

*5.8 Geochemical interpretations*

Geochemical signatures may be useful in determining the emplacement of the domes. Diapirism is the favored form of pluton emplacement in the Archean (Whitney et al. 2004; Chardon et al. 2009), but it is still undetermined if these domes were emplaced through the "bubbling up" of felsic plutonic material or through lateral folding (likely during $D_1$) (Whitney et al. 2004). Understanding the emplacement of these domes is critical for understanding ancient melting processes, as well. Due to the elevated temperature of the Archean mantle, melting and tectonics did not occur in the same way we observe today. Trace element geochemistry will be key in determining which elements are depleted and which are enriched. Enrichment and depletion of particular elements (Sr, Cr, Ni, Y, La, Yb) can indicate sources for the pluton (Martin et al. 2005), be it a slab or crustal melt, or a shallow mantle melt. If a pluton is depleted in Sr, then it has not interacted significantly with the shallow mantle and may indicate a deeper source (Martin et al. 2005). These interpretations will be possible with ICP-MS data.

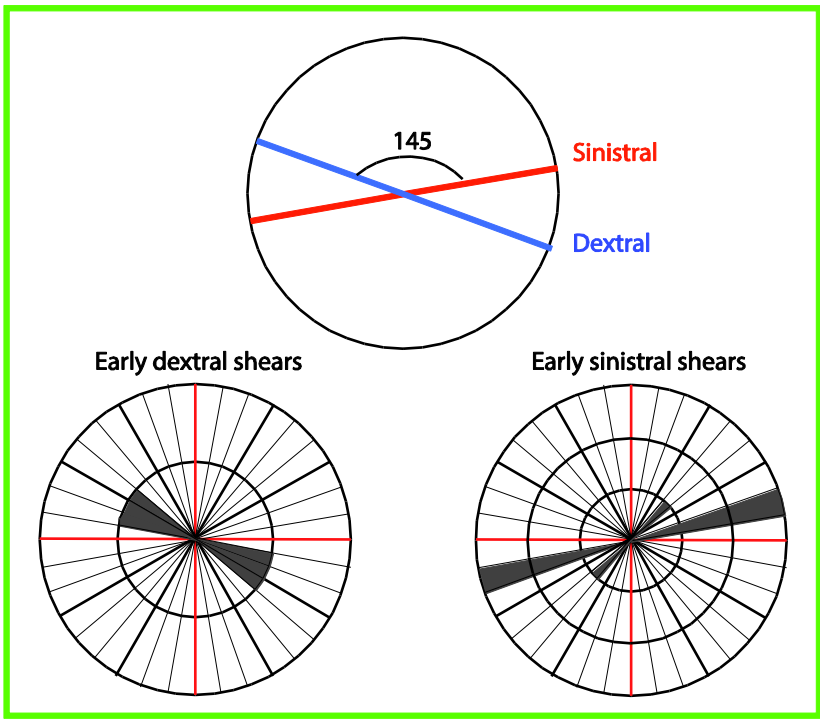


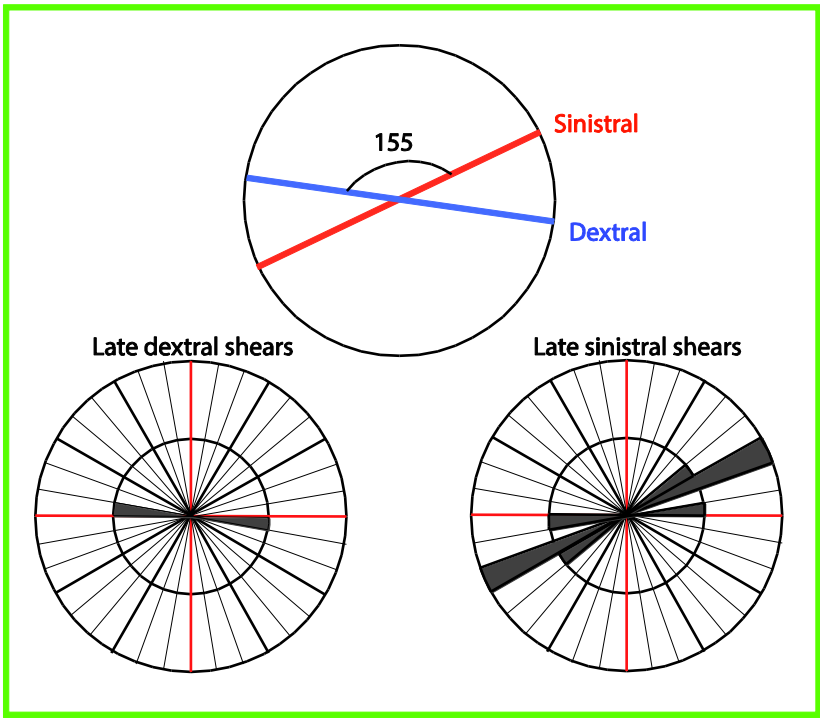


**Figure 33:** Early and late orientations of shear zones at the anastomosing outcrop at RBD 13-07. Timing of shear zone activity inferred from the width of the shear zones. Both early and late sets are rotated almost even with the shear plane, indicating that these sets may have formed nearly at the same time. Shortening direction is nearly north-south in both early and late sets of shear zones.


**Figure 34:** Mineralization in a small quartz vein. This occurrence was observed at station RBD 13-10.

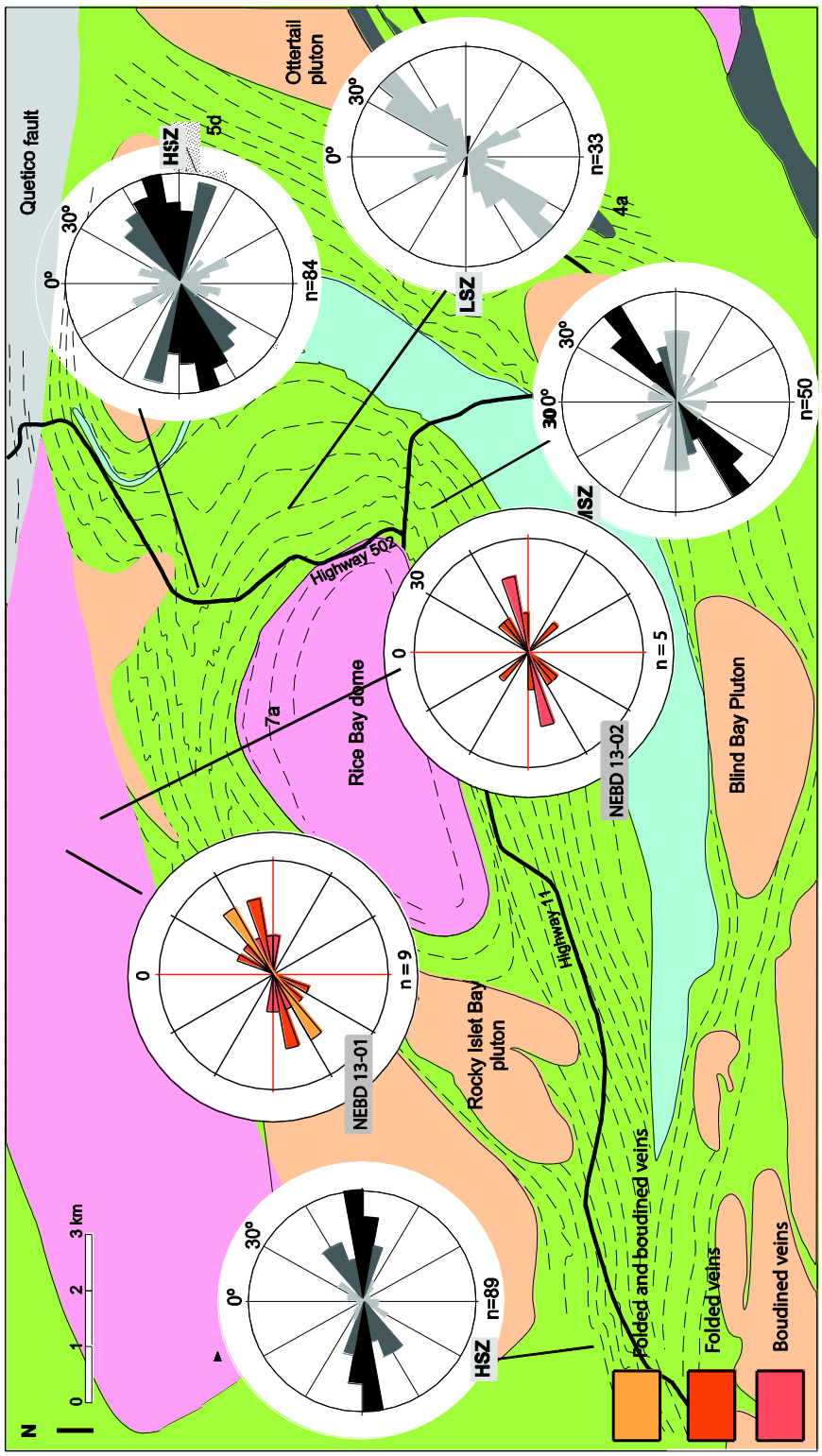


**Figure 35:** Folded and boudined veins from the NEBD (red) compared to Druguet et al. (2008) estimates from surrounding schists (gray). Note similarity to the surrounding strain data.

| Sample | X | Y | Z |
|---|---|---|---|
| 13-17 run 2 | 1.59 | 0.92 | 0.71 |
| 13-17 run 1 | 1.16 | 1.02 | 0.85 |
| 13-11 run 3 | 1.75 | 1.2 | 0.48 |
| 13-11 run 2 | 1.67 | 1.27 | 0.47 |
| 13-11 run 1 | 1.3 | 1.09 | 0.71 |
| 13-01 run 4 | 1.23 | 0.94 | 0.87 |
| 13-01 run 3 | 1.23 | 1.08 | 0.75 |
| 13-01 run 2 | 1.16 | 0.99 | 0.87 |
| 13-01 run 1 | 1.15 | 1 | 0.88 |
| NEBD 13-01 | 1.85 | 1.05 | 0.51 |
| NEBD 13-02 | 1.64 | 0.99 | 0.62 |
| | | | |
| Druguet A | 1.13 | 1.08 | 0.82 |
| Druguet B | 1.22 | 1.01 | 0.81 |
| Druguet C | 1.29 | 1.02 | 0.76 |
| Druguet D | 1.43 | 0.96 | 0.73 |
| Druguet E | 2.19 | 1.15 | 0.4 |
| Druguet F | 1.75 | 1.55 | 0.37 |
| Druguet G | 2.56 | 1.21 | 0.32 |

**Table 3**: Principal axes magnitudes of strain ellipsoids from the RBD and NEBD compared to Druguet et al. (2008). Values highlighted in orange are not nearby the study area, and show significantly higher strain.

## Chapter 6: Conclusions

The Rice Bay and Northeast Bay gneiss domes underwent significant deformation during the Neo-Archean Kenoran orogeny. This deformation can be quantified and assessed through detailed field studies, and compared to the deformation in neighboring units, as undertaken here.

1: The Rice Bay and Northeast Bay domes accommodated strain in different ways. Shear zone evidence points to the RBD partitioning the shortening along discrete shear bands, while in the NEBD, any shortening must have been accommodated in the rock itself. Both units accommodated the dextral motion associated with transpression through shear zones as well; 70% of shear zones within the RBD were dextral, while all shear zones in the NEBD were dextral. The difference between the two domes is likely related to proximity with the Quetico Shear Zone.

2: Data from mafic enclave analyses in the RBD indicate plane strain was occurring and the strain magnitude was low. Some local strain perturbations were present, which yielded strain ellipsoid shapes of flattening. This is consistent with the dominance of foliation over lineation (S>L fabrics) in the area.

3: Data from folded and boudined vein analyses in the NEBD yielded similar strain ellipsoid shapes as the RBD. Plane strain was a dominant process with local strain perturbations. The magnitude of strain in the NEBD was greater than the strain magnitude in the RBD, however.

4: The lineations directly observed in the RBD were shallow to subhorizontal and obliquely plunging. Although no lineations were observed in the NEBD (due to poor outcrop exposure), it is inferred from the strain analysis from folded and boudined veins that the lineation is subvertical. The different lineation orientations may be a result of different kinematics. Units undergoing transpression in which pure shear is dominant will display vertical to subvertical lineations, while units in areas where simple shear is dominant will display subhorizontal to shallowly plunging lineations in low strain (Fossen & Tikoff 1993; Lin et al. 1999; Fernández et al. 2013).

5: To test the transpression conditions in each unit, modeling was employed to determine the shear obliquity angle, the extrusion angle, the kinematic vorticity, and the amount of finite strain in a rock. The models were matched to lineation orientations and strain ellipsoid data. In the RBD, only one model was mostly consistent with the three stations having both strain and lineation data. This model invokes a simple shear obliquity angle of 20°E and a subvertical extrusion angle. The estimated kinematic vorticities from this model suggest the RBD underwent noncoaxial deformation with simple shear being dominant ($W_k$ approximately 0.99). These rocks had accumulated a considerable amount of finite strain as well. In this case, while many of the discrete shear zones were accommodating shortening, the bulk rock and other shear zone sets were accommodating the dextral shear.

6: In the NEBD, several models fit the field data observed. These models varied in shear obliquity angle, but the extrusion angles were fairly consistent at subvertical angles. Unlike the RBD, these models suggested a lower kinematic vorticity value ($W_k$

approximately 0.24-0.89). This indicates pure shear was a dominant process here. In this case, while all of the discrete shear zones were accommodating dextral shear, the bulk rock was accommodating the shortening.

7: The differences between the matching transpression models for the two domes could explain the difference in lineation orientation between the two domes. If the NEBD is undergoing pure shear dominated deformation, then the lineations should be subvertical (Fossen & Tikoff 1993). Conversely, if the RBD is undergoing simple shear dominated deformation, the lineations should be subhorizontal and approach subvertical orientations with progressive finite strain accumulation (Fossen & Tikoff 1993).

8: Compared to the surrounding region, the RBD and NEBD accommodated deformation very differently. Within the units that have been extensively studied, these gneisses are the most competent of them all. Folded and boudined vein orientations from the NEBD match those documented in Druguet et al. 2008, and anastomosing shear zones are operating similarly to those in the metagabbros documented by Carreras et al. 2010. The $W_k$ values for the NEBD are consistent with the values determined for the surrounding schists (Druguet et al. 2008) and the Seine metaconglomerates (Fernández et al. 2013). The RBD's kinematic vorticity values appear to be too high to fit with the surrounding field data.

9: No emplacement structures appear to be intact. All lineations and foliations can be attributed to $D_2$ transpressive deformation. This means that other means will need to be utilized to determine emplacement of the domes, such as geochemical analysis or AMS techniques. AMS techniques have been successful in the nearby Ash Bay Dome

(Borradaile et al. 2003) and could prove useful in these two units. Geochemical analyses seem to indicate that there are key differences in the petrology of the center of the dome, such as an enrichment of heavier elements.

10: Lastly, this study has proven that this method of modeling is a practical method for determining transpressional conditions in rocks that have undergone considerable deformation. It can be applied to nearly any deformed rock with lineations and strain markers, and can yield results that can be compared to vastly different rock units with different deformation mechanisms.

## References

Allmendinger, R., 2012. Stereonet 8 computer program. http://www.geo.cornell.edu/geology/faculty/RWA/programs/stereonet-7-for-windows/

Bauer, R., Czeck, D., Hudleston, P., & Tikoff, B., 2011. Structural geology of the subprovince boundaries in the Archean Superior Province of Northern Minnesota and adjacent Ontario. GSA Field Guides. DOI:10.1130/2011.0024(10).

Borradaile, G.J., Gauthier, D., 2002. Emplacement of an Archean gneiss dome, northern Ontario, Canada: Inflation inferred from magnetic fabrics. Tectonics 22, 6.1-6.8.

Burg, J.-P. 1999. Ductile structures and instabilities; their implication for Variscan tectonics in the Ardennes. Tectonophysics 309, 1-25.

Butler, R. W. H., Casey, M., Lloyd, G. E., Bond, C. E., McDade, P., Shipton, Z., Jones, R., 2002. Vertical stretching and crust thickening at Nanga Parbat, Pakistan Himalaya; a model for distributed continental deformation during mountain building. Tectonics 21, 9.1-9.17.

Carreras, J., Czeck, D., Druguet, E., Hudleston, P., 2010. Structure and Development of an anastomosing network of ductile shear zones. Journal of Structural Geology 32, 655-666.

Chardon, D., Gapais, D., Cagnard, F., 2009. Flow of ultra-hot orogens: a view from the Precambrian, clues for the Phanerozoic. Tectonophysics 477, 105-118.

Condie, K., 2005. TTGs and adakites: are they both slab melts? Lithos 80, 33-44.
Czeck, D. & Hudleston, P., 2003. Testing models for obliquely plunging lineations in transpression: a natural example and theoretical discussion. Journal of Structural Geology 25, 959-982.

Czeck, D., Fissler, D., Horsman, E., Tikoff, B., 2009. Strain analysis and rheology contrasts in polymictic conglomerates; an example from the Seine metaconglomerates, Superior Province, Canada. Journal of Structural Geology 31, 1365-1376.

Czeck, D., Maes, S., Sturm, C., Fein, E., 2006. Assessment of the relationship between emplacement of the Algoman plutons and regional deformation in the Rainy Lake region, Ontario. Canadian Journal of Earth Sciences 43, 1653-1671.

Czeck, D. M. and Poulsen, K. H., 2010. Field trip guide: Deformation in the Rainy Lake Region: A Fabulous Display of Structures Controlled by Rheological Contrasts. Institute on Lake Superior Geology 56th Annual Meeting, International Falls, MN, 2010; 56 Part 2, 47-75.

Davis, DW., Poulsen, KH., Kamo, KL., 1989. New insights into Archean crustal development from geochronology in the Rainy Lake area, Superior Province, Canada. The Journal of Geology 97, 379-398.

Druguet, E., Castaño, L., Czeck, D., Hudleston, P., Carreras, J., 2012. The tectonic significance of dikes of irregular fold-like shape. Geology 40, 579-582.

Druguet, E., Czeck, D., Carreras, J., Castaño, L., 2008. Emplacement and deformation features of syntectonic leucocratic veins from Rainy Lake zone (Western Superior Province, Canada). Precambrian Research 163, 384-400.

Fernández, C., Díaz Azpiroz, M., 2009. Triclinic transpression zones with inclined extrusion. Journal of Structural Geology 31, 1255-1269.

Fernández, C., Czeck, D., Díaz-Azpiroz, M., 2013. Testing the model of oblique transpression with oblique extrusion in two natural cases: Steps and consequences. Journal of Structural Geology 54, 85-102.

Flinn, D., 1965. On the symmetry principle and the deformation ellipsoid. Geological magazine 102, 36-45.

Fossen, H. & Tikoff, B., 1993. The deformation matrix for simultaneous simple shearing, pure shearing and volume change, and its application to transpression-transtension tectonics. Journal of Structural Geology 15, 413-422.

Gerya, T., Perchuk, L., Maresch, W., Willner, A., 2004. Inherent gravitational instability of hot continental crust; implications for doming and diapirism in granulite facies terrains. Special paper—Geological Society of America 380, 97-115.

Goodwin, L., & Williams, P., 1996. Deformation path partitioning within a transpressive shear zone, Marble Cove, Newfoundland. Journal of Structural Geology 18, 975-990.

Harland, W.B., 1971, Tectonic transpression in Caledonian Spitsbergen. Geological Magazine 108, p. 27–42

Hobbs, B.E., Means, W.D., Williams, P.F., 1978. An Outline of Structural Geology. Wiley & Sons, 1978.

Hossack, J., 1968. Pebble deformation and thrusting in the Bygdin region (southern Norway). Tectonophysics 5, 315-339.

King, D. S., Klepeis, K. A., Goldstein, A. G., Gehrels, G. E., Clarke, G. L., 2008. The initiation and evolution of the transpressional Straight River shear zone, central Fiordland, New Zealand. Journal of Structural Geology 30, 410-430.

Lin, S., Jiang, D., Williams, P. F., 1998. Transpression (or transtension) zones of triclinic symmetry: natural example and theoretical modeling. In: Holdsworth, R. E., Strachran, R. A. & Dewey, J. F. (Ed.), Continental Transpressional and Transtensional Tectonics. Geological Society of London, Special Publications 135. Geological Society of London, London, 41-57.

Lisle, R. J., 1985. Geological Strain Analysis: A Manual for the Rf/φ Method. Pergamon Press, Oxford.

Lowell, J.D., 1972. Spitsbergen Tertiary orogenic belt and the Spitsbergen fracture zone. Geological Society of America Bulletin 83, 3091-3102.

Mancktelow, N.S., 2002. Finite-element modelling of shear zone development in viscoelastic materials and its implications for localisation of partial melts. Journal of Structural Geology 24, 1045-1053.

Marquis, R., 2004. Towards a better understanding of the Superior Province. Quebec Mines, Mining information bulletin. http://www.mrnf.gouv.qc.ca/english/mines/quebec-mines/2004-10/superior.asp.

Martin, H., Smithies, R.H., Rapp, R., Moyen, J.-F., Champion, D., 2005. An overview of adakite, tonalite-trondjhemite-granodiorite (TTG), and sanukitoid: relationships and some implications for crustal evolution. Lithos 79, 1-24.

Mitra, G., 1979. Ductile deformation zones in Blue Ridge basement rocks and estimation of finite strains. Geological Society of America Bulletin 10, 935-951.

Mookerjee, M., 2013. Rose diagram program. Geological Programs for Mathematica.

Mulchrone, K.F., O'Sullivan, F., Meer, P.A., 2003. Finite strain estimation using the mean radial length of elliptical objects with bootstrap confidence intervals. Journal of Structural Geology 25, 529-539.

Owens, W.H., 1984. The calculation of a best-fit ellipsoid from elliptical sections on arbitrarily oriented planes. Journal of Structural Geology 6, 571-578.

Paterson, S., Pignotta, G., Vernon, R., 2004. The significance of microgranitoid enclave shapes and orientations. Journal of Structural Geology 26, 1465-1481.

Poulsen, 2000. Archean Metallogeny of the Mine Center-Ft. Frances area. Ontario Geological Survey Report 266.

Poulsen, K.H., 2000b. Geological Setting of Mineralization in the Mine Centre–Fort Frances Area: Ontario Geological Survey Mineral Deposits Circular 29, 78 p.

Ramsay,J.G., Huber,M.I.,1987. The Techniques of Modern Structural Geology. Folds and Fractures, vol. 2 Academic Press, London.

Richards, J. & Kerrich, R., 2007. Special paper: Adakite-like rocks: Their diverse origins and questionable role in metallogenesis. Bulletin of the Society of Economic Geologists 102, 537-576.

Sanderson, D. & Marchini, R.D., 1984. Transpression. Journal of Structural Geology 6, 449-458.

Saintot, A., Stephenson, R., Brem, A., 2003. Paleostress field reconstruction and revised tectonic history of the Donbas fold and thrust belt (Ukraine and Russia). Tectonics 22, doi:10.1029/2002TC001366.

Shimamoto, T., Ikeda, Y., 1976. A simple algebraic method for strain estimation from deformed ellipsoidal objects. 1. Basic theory. Tectonophysics 36, 315-337.

Stone, D., Halle, J., & Murphy, R., 1997a. Precambrian Geology, Mine Center area: Ontario Geological Survey preliminary map p. 3372.

Stone D., Halle, J., & Murphy, R., 1997b. Precambrian Geology, Mine Center area: Ontario Geological Survey preliminary map p. 3373.

Sullivan, W. A., Law, R. D., 2007. Deformation path partitioning within the transpressional White Mountain shear zone, California and Nevada. Journal of Structural Geology 29, 583-598.

Talbot, C.J., 1970. The minimum strain ellipsoid using deformed quartz veins. Tectonophysics 9, 47-67.

Tikoff, B., Greene, D., 1997. Stretching lineations in transpressional shear zones: an example from the Sierra Nevada Batholith, California. Journal of Structural Geology 19, 29-39.

Vollmer, F., 2013. EllipseFit computer program.

Whitney, D., Teyssier, C. & Vanderhaege, O., 2004. Gneiss domes and crustal flow. Geological Society of America Special Paper 380, 15-34.

Wood, J., Dekker, J., Jansen, J.G., Keay, J.P., Panagapko, D., 1980a. Mine Centre (Eastern half), District of Rainy River: Ontario Geological Survey preliminary map p. 2202.

Wood, J., Dekker, J., Jansen, J.G., Keay, J.P., Panagapko, D., 1980b. Mine Centre (Western half), District of Rainy River: Ontario Geological Survey preliminary map p. 2201.

Yonkee, A., 2005. Strain patterns within part of the Willard thrust sheet, Idaho-Utah-Wyoming thrust belt. Journal of Structural Geology 27, 1315-1343.

Yonkee, A., 2013. Rfphi & Strain3D computer programs.

Yonkee, W. A., Czeck, D. M., Nachbor, A., Barszewski, C. B., Pantone, S., Balgord, E., Johnson, K. R., 2013. Strain accumulation and fluid-rock interaction in a naturally deformed diamictite, Willard thrust system, Utah (USA): Implications for crustal rheology and strain softening. Journal of Structural Geology 50, 91-118.

## **Appendix A:** Transpression modeling

This appendix outlines the protocols used during the transpression modeling portion of this study. Included here are the model outputs from the Microsoft Excel spreadsheet (Fernández et al. 2013) and the matching models from field observations.

For the model outputs, both Flinn plots and equal angle stereonets containing the X axis orientations for the output strain ellipsoid are shown for shear obliquity angles of 0°, 20°E, and 20° W (0, 20, and 160, on models). Extrusion angles vary from 0° to 180°. Each colored dot on the stereonet correlates to a kinematic vorticity ratio, shown below:

| | $\dot{\gamma} / \dot{\varepsilon}$ | $W_k$ |
|---|---|---|
| ● | .5 | 0.24 |
| ● | 1 | 0.45 |
| ● | 2 | 0.71 |
| ● | 4 | 0.89 |
| ● | 6 | 0.95 |
| ● | 20 | 0.99 |

In the transpression model comparison charts, fields of matching data are highlighted in gray. The "Lineation" column corresponds to matching lineation for that $\frac{\dot{\gamma}}{\dot{\varepsilon}}$ value (shown in the far left hand columns), the "Ellipse" column refers to matching angles of elongation angles and axial ratios of 2D sectional ellipses on the horizontal plane, and the "Flinn plot" column refers to matching strain ellipsoid data. For stations that did not have observations regarding the latter two data, a red X is drawn through

those columns. Models that were considered a good fit have a solid blue box drawn around the $\frac{\dot{\gamma}}{\dot{\varepsilon}}$ values for which the data matched, while models considered a poor fit have dashed boxes drawn around the most likely $\frac{\dot{\gamma}}{\dot{\varepsilon}}$ value for the model.

The data compared to these models is shown on the following page. The top stereonets are lineation measurements for the RBD. Lineations in the NEBD are assumed to be vertical. The Flinn plots from the RBD and NEBD are also shown.

| | |
|---|---|
| RBD 13-01 | 24°→122° |
| RBD 13-01 | 8°→290° |
| RBD 13-04 | 33°→96° |
| RBD 13-05 | 30°→90° |
| RBD 13-08 | 68°→315° |
| RBD 13-10 | 13°→259° |
| RBD 13-11 | 20°→315° |
| RBD 13-16 | 25°→240° |
| RBD 13-17 | 12°→95° |
| RBD 13-17 | 20°→97° |
| RBD 13-20 | 24°→46° |
| RBD 13-26 | 10°→100° |

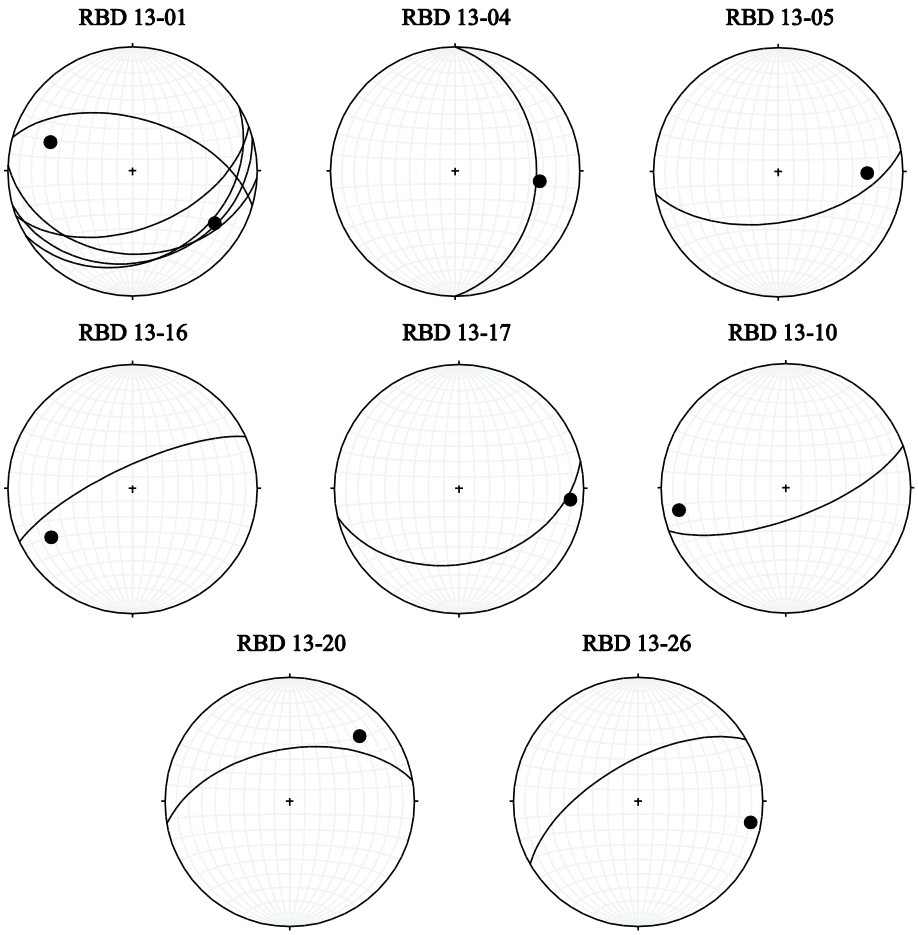


Lineation orientations for the RBD. Numerical orientations shown in table at top, stereonet representations at bottom.

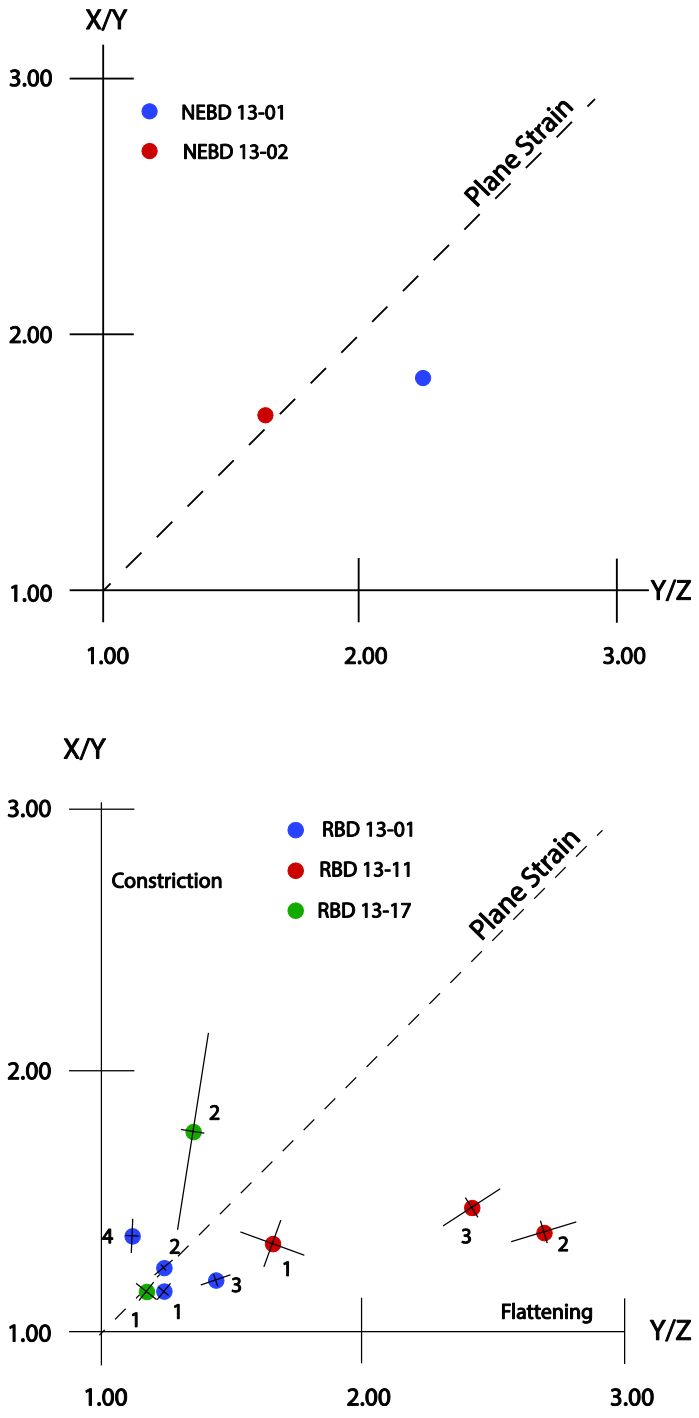


Flinn plots for the NEBD strained dikes and veins (top) and RBD mafic enclaves (bottom).

Shown below are model outputs for all models with a shear obliquity angle of 0°. Flinn plots on left for different values of φ and ν, as indicated, plotted for an array of $\frac{\dot{\gamma}}{\dot{\varepsilon}}$ with increasing strain. Corresponding equal area stereonets for the long axis of the strain ellipsoid (lineation) on right; different $W_k$ values shown in colors given in table on page 120 plotted along a strain path. In all cases, the lineations approach the extrusion orientation with increasing strain.

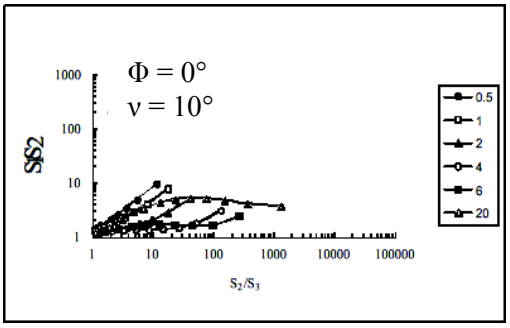


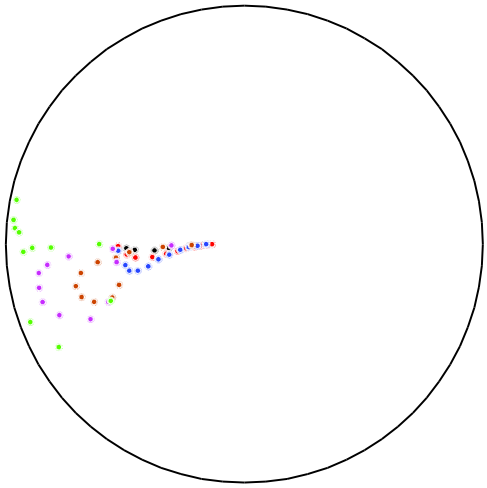

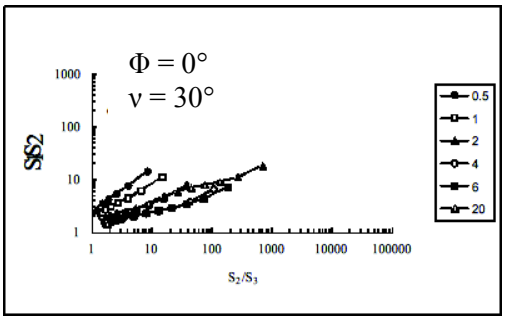


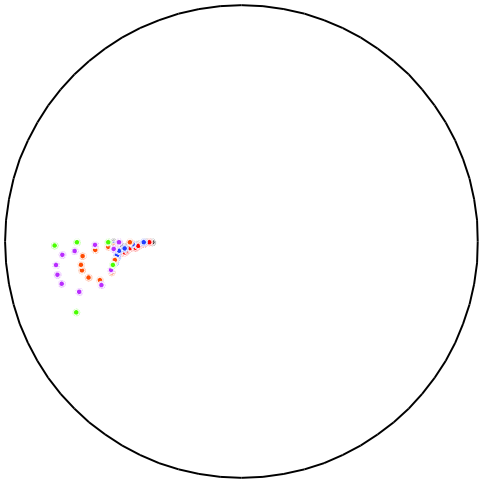

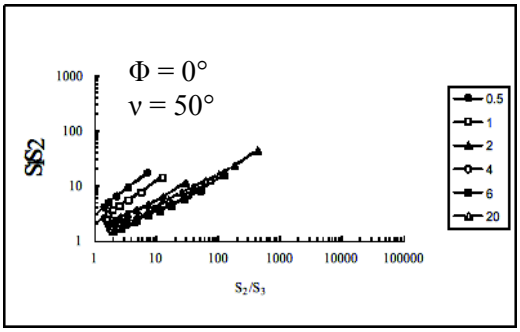
Φ = 0°
ν = 50°
SS2
1000
100
10
1
1
10
100
1000
10000
100000
S2/S3
0.5
1
2
4
6
20

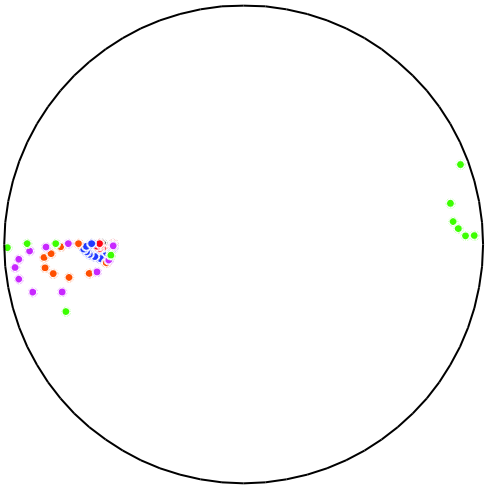

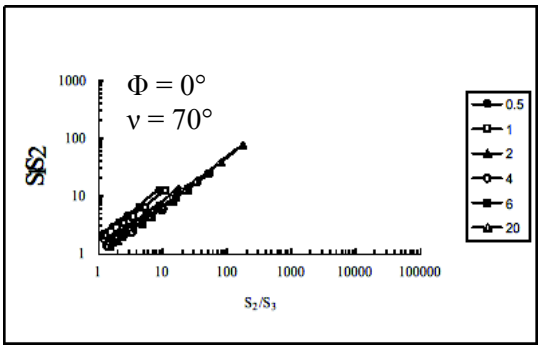
Φ = 0°
ν = 70°
SS2
1000
100
10
1
1
10
100
1000
10000
100000
S2/S3
0.5
1
2
4
6
20

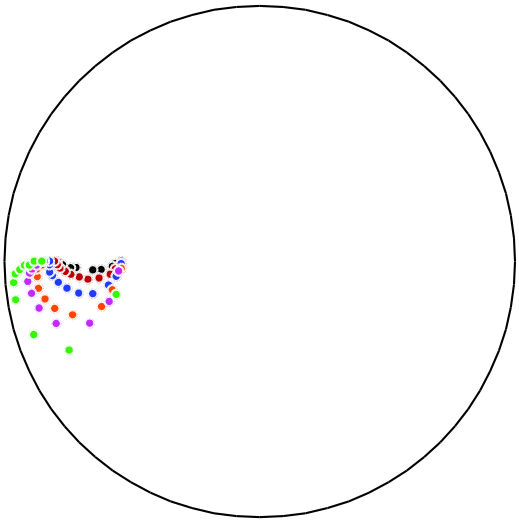

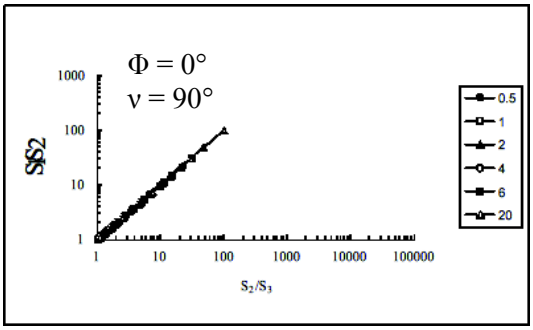
Φ = 0°
ν = 90°
SS2
1000
100
10
1
1
10
100
1000
10000
100000
S2/S3
0.5
1
2
4
6
20

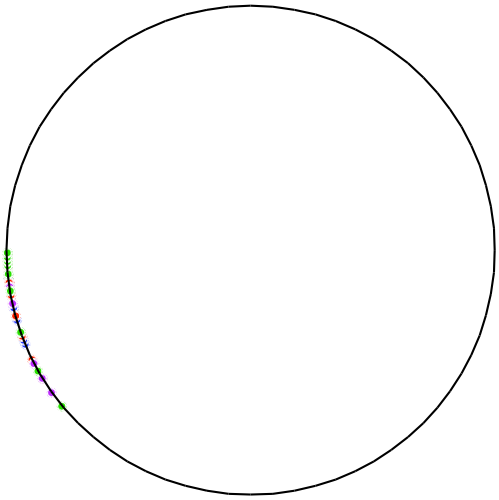

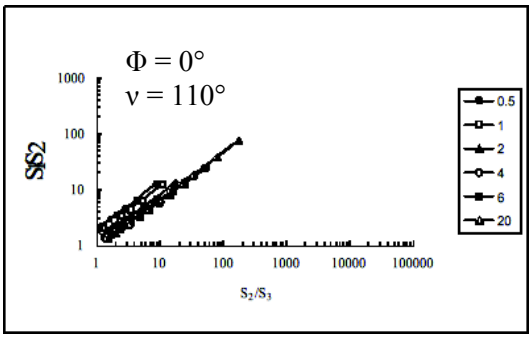
Φ = 0°
ν = 110°
SS2
1000
100
10
1
1
10
100
1000
10000
100000
S2/S3
0.5
1
2
4
6
20

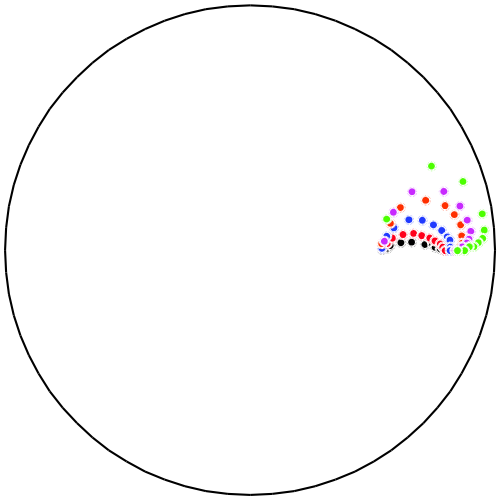

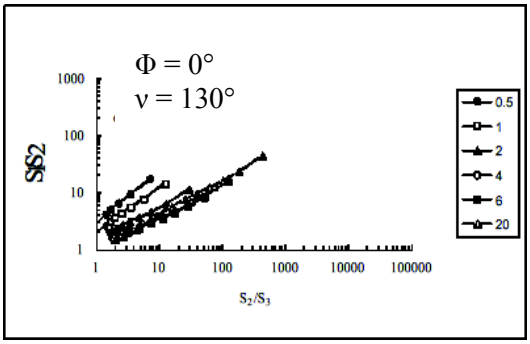
Φ = 0°
ν = 130°
SS2
1000
100
10
1
1
10
100
1000
10000
100000
S2/S3
0.5
1
2
4
6
20

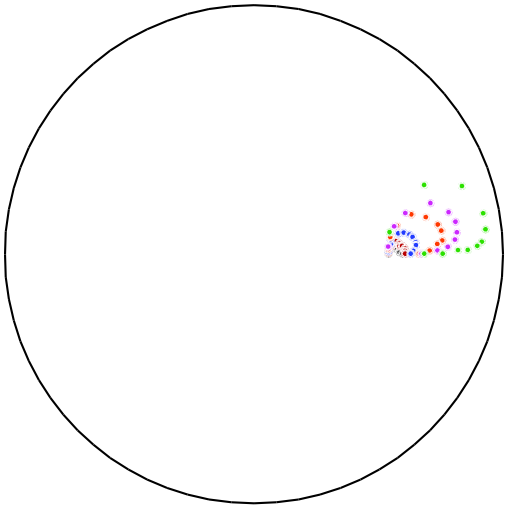

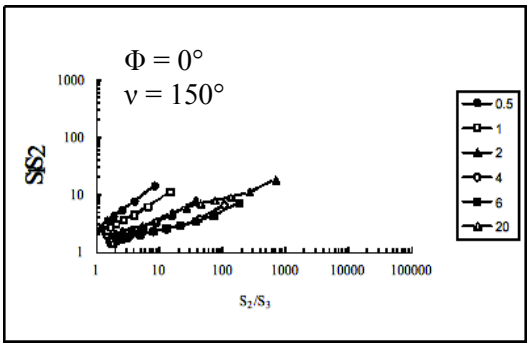
Φ = 0°
ν = 150°
SS2
1000
100
10
1
1
10
100
1000
10000
100000
S2/S3
0.5
1
2
4
6
20

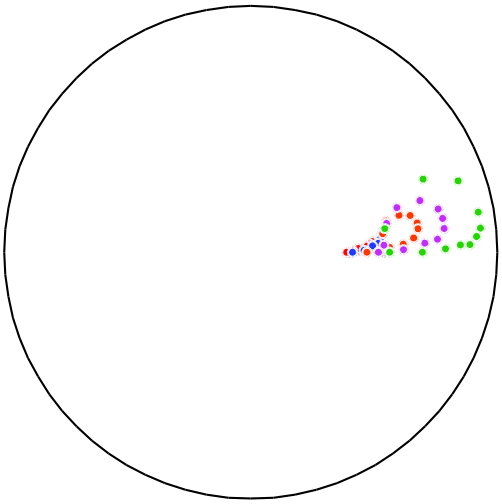

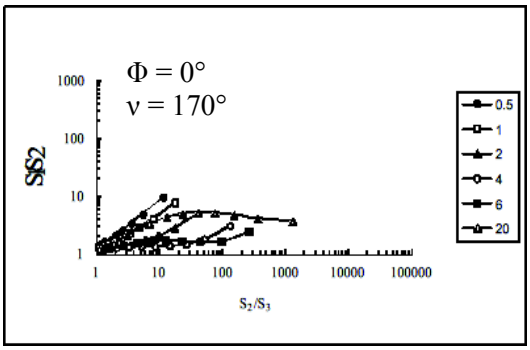
Φ = 0°
ν = 170°
SS2
1000
100
10
1
1
10
100
1000
10000
100000
S2/S3
0.5
1
2
4
6
20

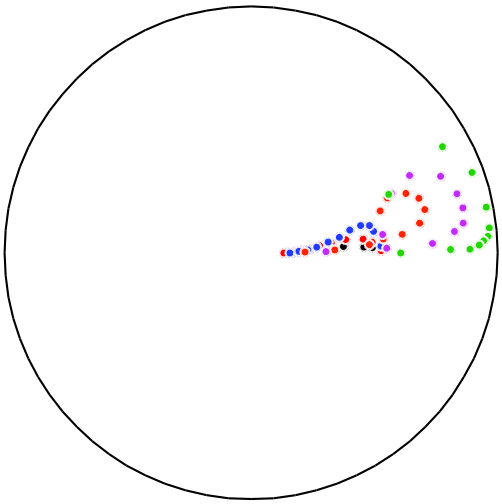

Shown below are model outputs for all models with a shear obliquity angle of 20°. Flinn plots on left for different values of φ and ν, as indicated, plotted for an array of $\frac{\dot{\gamma}}{\dot{\varepsilon}}$ with increasing strain. Corresponding equal area stereonets for the long axis of the strain ellipsoid (lineation) on right; different $W_k$ values shown in colors given in table on page 120 plotted along a strain path. In all cases, the lineations approach the extrusion orientation with increasing strain.

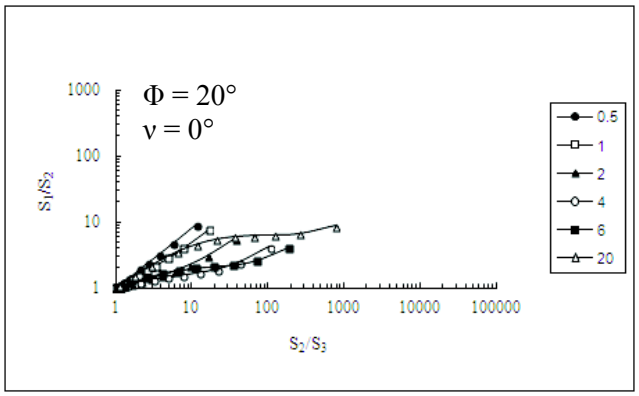


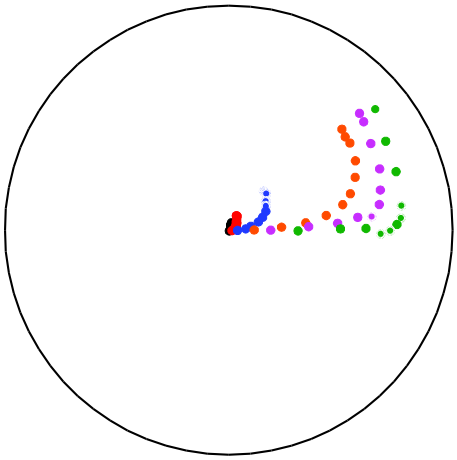

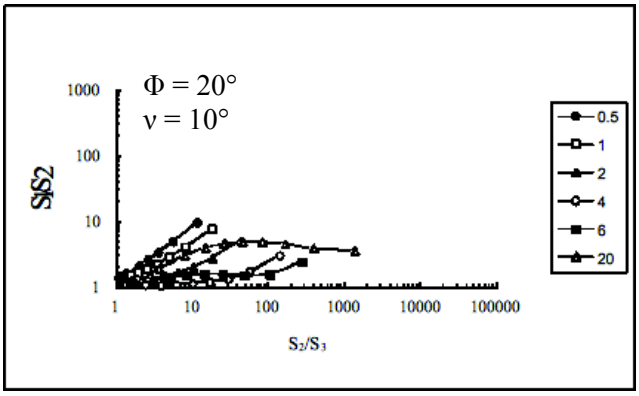


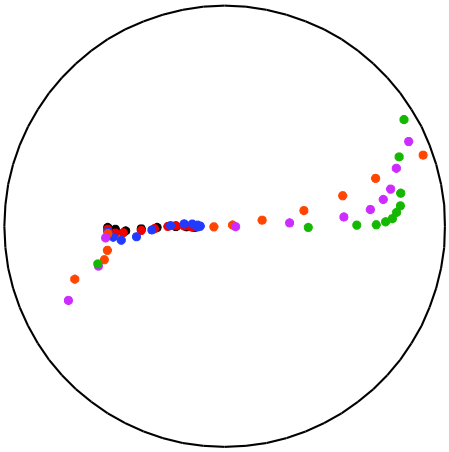

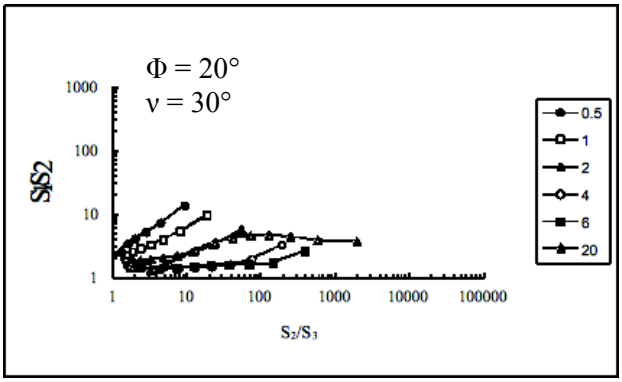
Φ = 20°
ν = 30°
S/S2
1000
100
10
1
1
10
100
1000
10000
100000
S2/S3
0.5
1
2
4
6
20

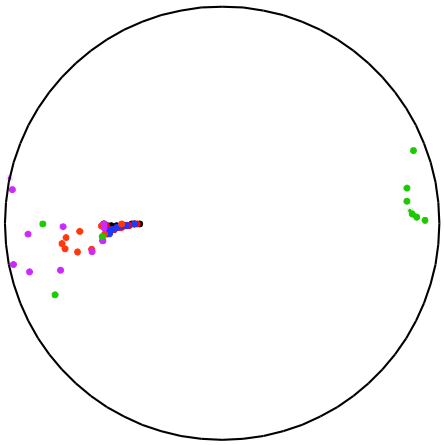

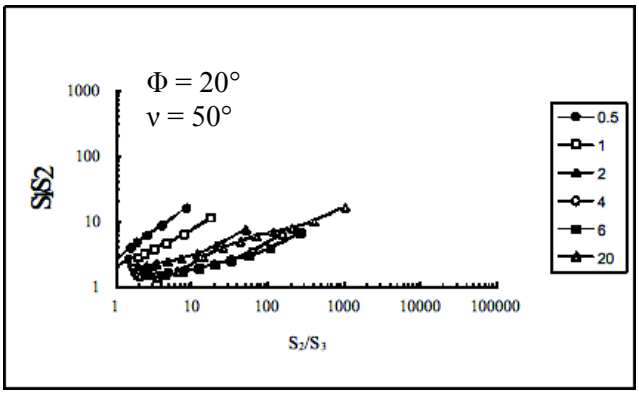
Φ = 20°
ν = 50°
S/S2
1000
100
10
1
1
10
100
1000
10000
100000
S2/S3
0.5
1
2
4
6
20

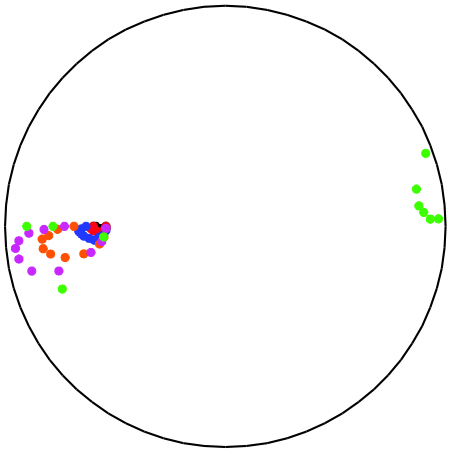

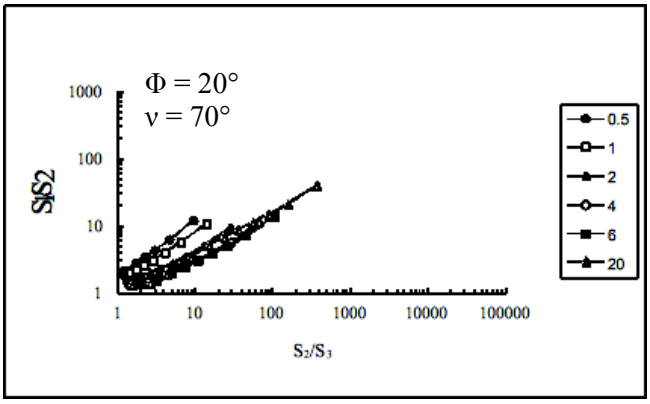
Φ = 20°
ν = 70°
S/S2
1000
100
10
1
1
10
100
1000
10000
100000
S2/S3
0.5
1
2
4
6
20

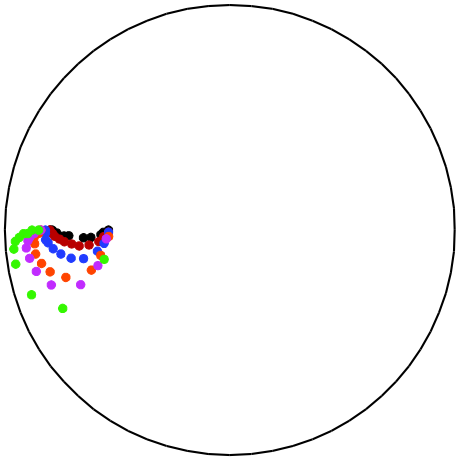

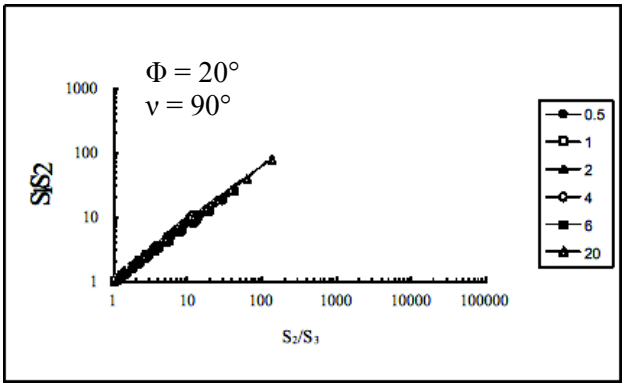
Φ = 20°
ν = 90°
S/S2
1000
100
10
1
1
10
100
1000
10000
100000
S2/S3
0.5
1
2
4
6
20

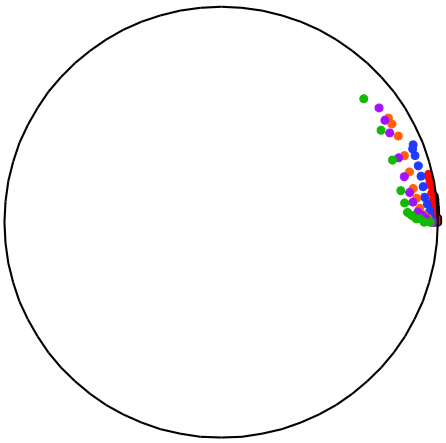

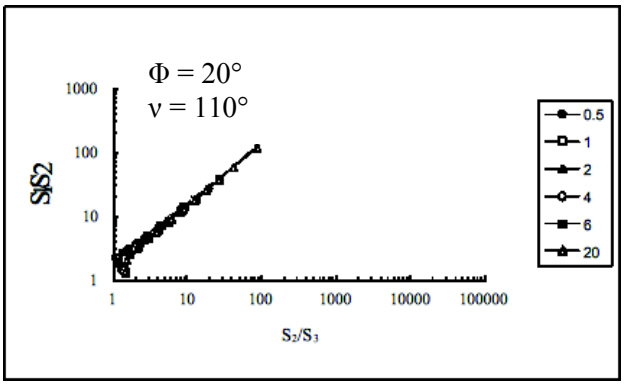
Φ = 20°
ν = 110°
S/S2
1000
100
10
1
1
10
100
1000
10000
100000
S2/S3
0.5
1
2
4
6
20

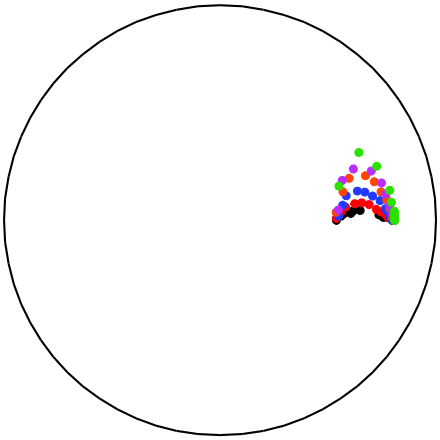

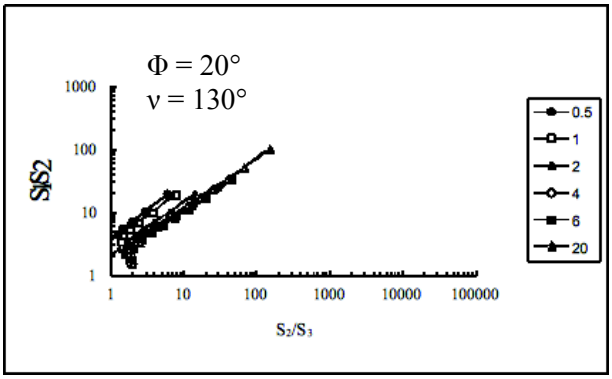
Φ = 20°
ν = 130°
S/S2
1000
100
10
1
1
10
100
1000
10000
100000
S2/S3
0.5
1
2
4
6
20

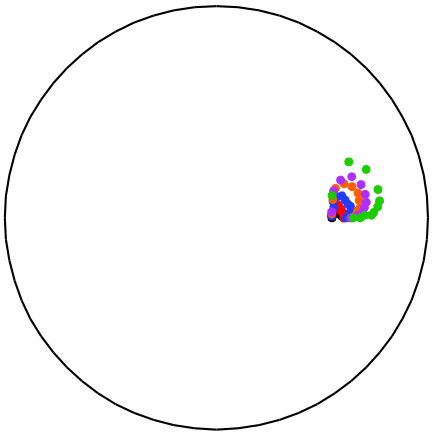

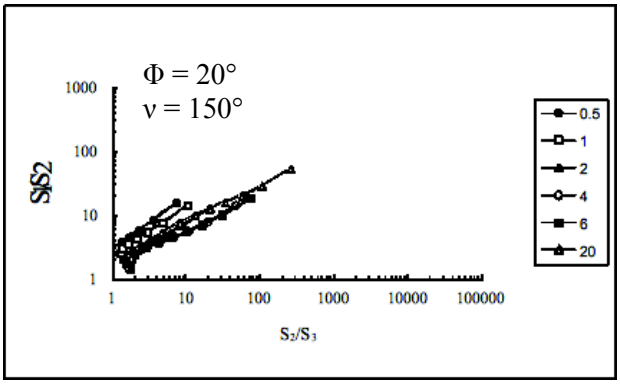
Φ = 20°
ν = 150°
S/S2
1000
100
10
1
1
10
100
1000
10000
100000
S2/S3
0.5
1
2
4
6
20

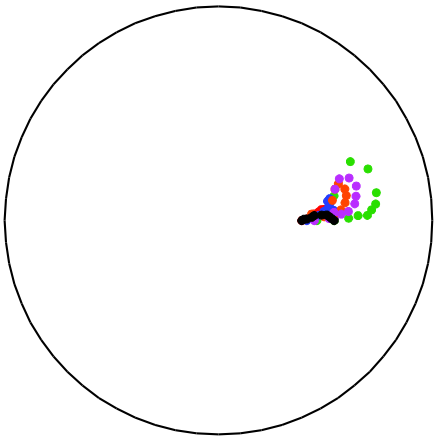

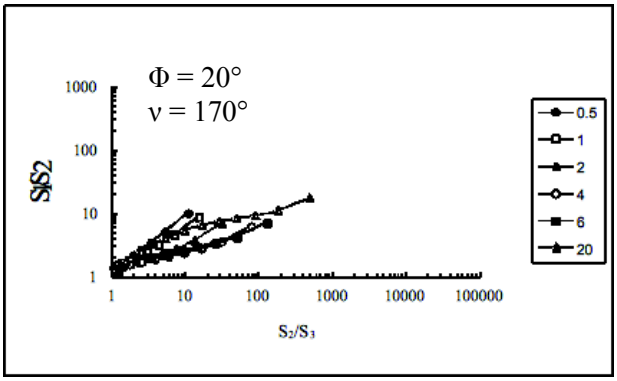
Φ = 20°
ν = 170°
S/S2
1000
100
10
1
1
10
100
1000
10000
100000
S2/S3
0.5
1
2
4
6
20

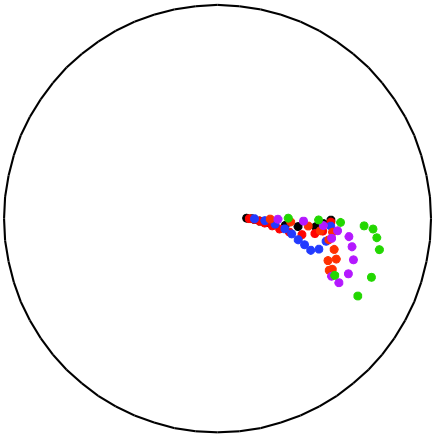

Shown below are model outputs for all models with a shear obliquity angle of 160°. Flinn plots on left for different values of φ and ν, as indicated, plotted for an array of $\frac{\dot{\gamma}}{\dot{\varepsilon}}$ with increasing strain. Corresponding equal area stereonets for the long axis of the strain ellipsoid (lineation) on right; different $W_k$ values shown in colors given in table on page 120 plotted along a strain path. In all cases, the lineations approach the extrusion orientation with increasing strain.

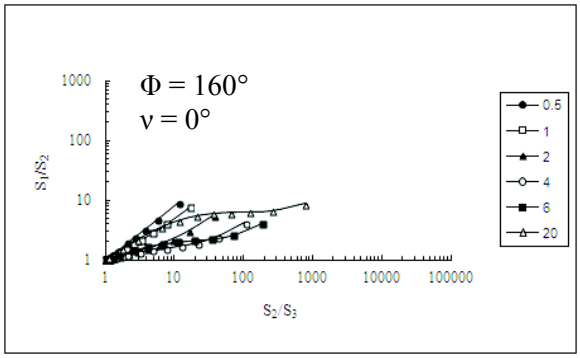


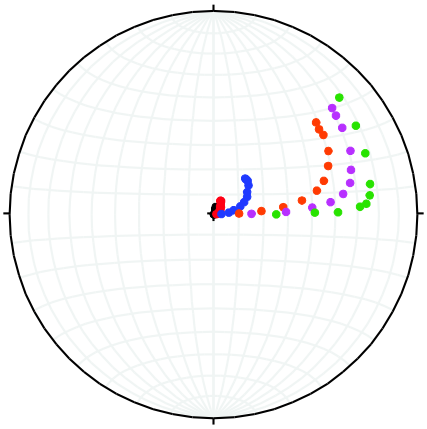

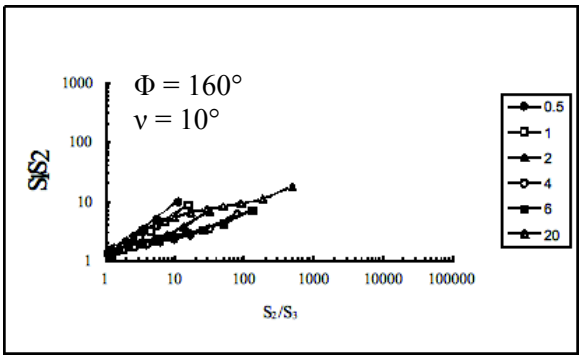


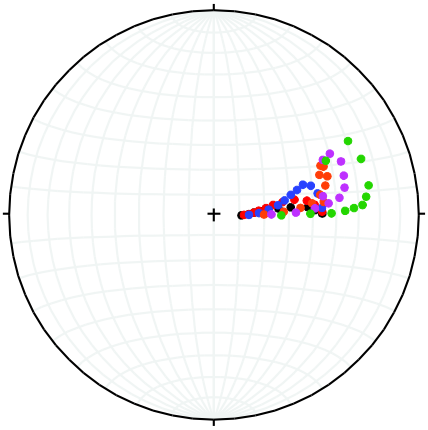

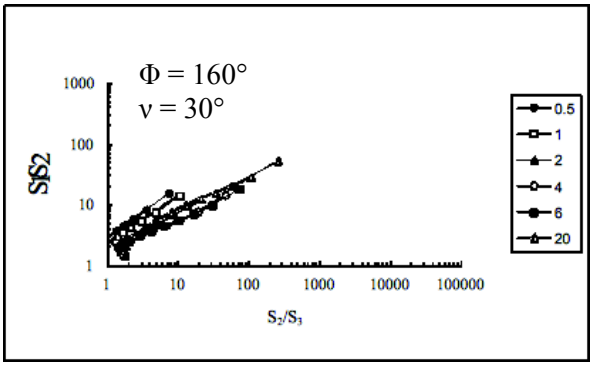


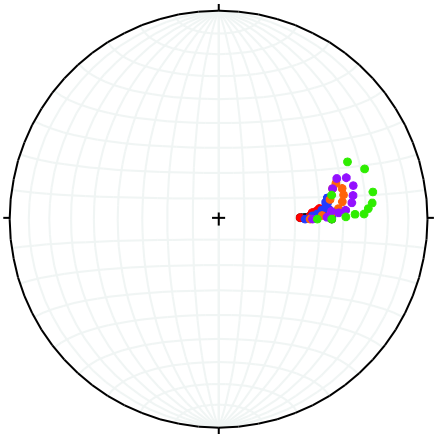

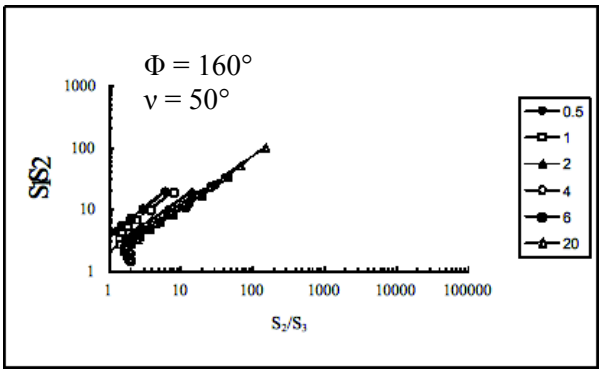
Φ = 160°
ν = 50°
S/S2
1000
100
10
1
1
10
100
1000
10000
100000
S2/S3
0.5
1
2
4
6
20

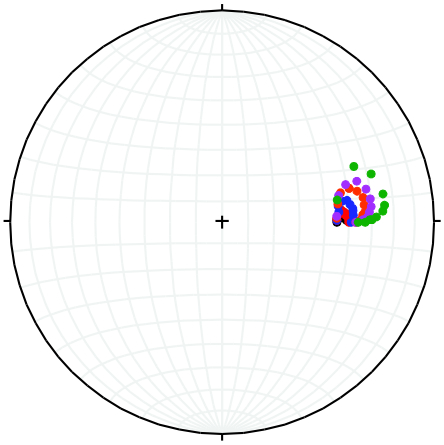

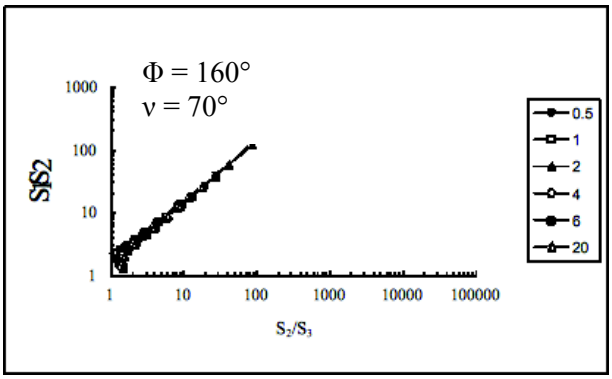
Φ = 160°
ν = 70°
S/S2
1000
100
10
1
1
10
100
1000
10000
100000
S2/S3
0.5
1
2
4
6
20

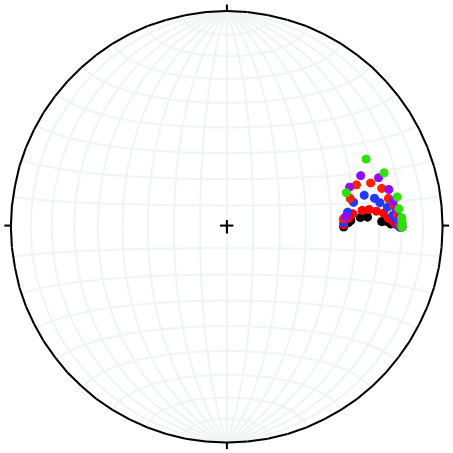

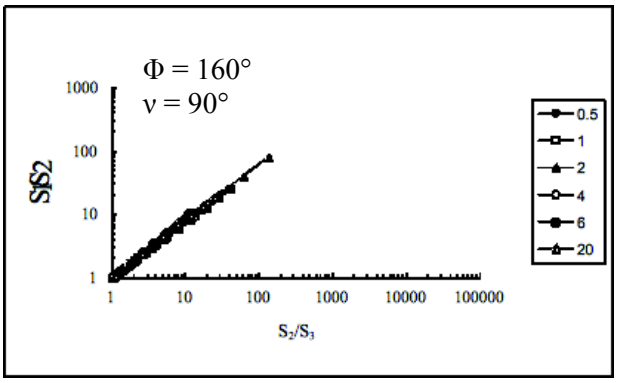
Φ = 160°
ν = 90°
S/S2
1000
100
10
1
1
10
100
1000
10000
100000
S2/S3
0.5
1
2
4
6
20

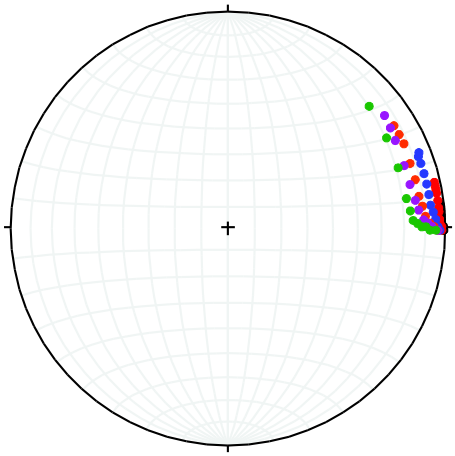

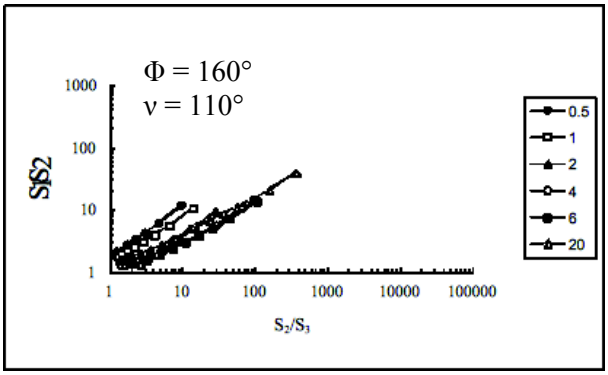
Φ = 160°
ν = 110°
S/S2
1000
100
10
1
1
10
100
1000
10000
100000
S2/S3
0.5
1
2
4
6
20

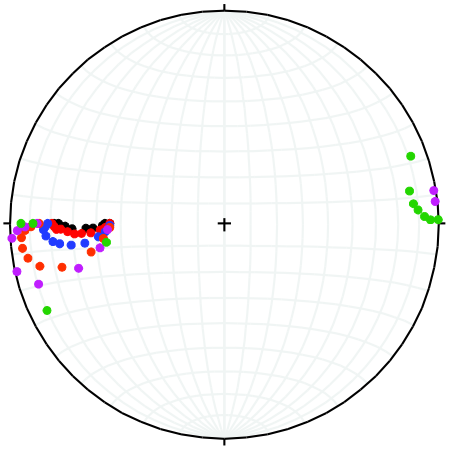

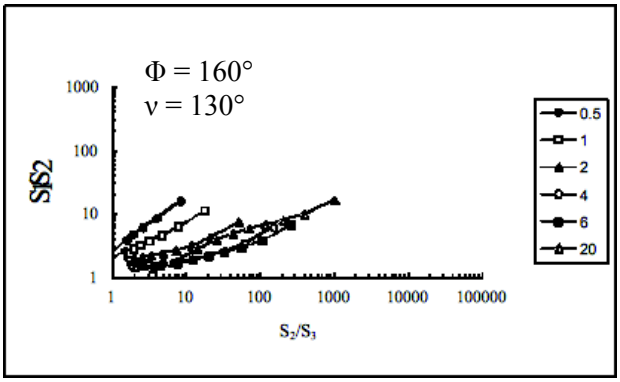
Φ = 160°
ν = 130°
S/S2
1000
100
10
1
1
10
100
1000
10000
100000
S2/S3
0.5
1
2
4
6
20

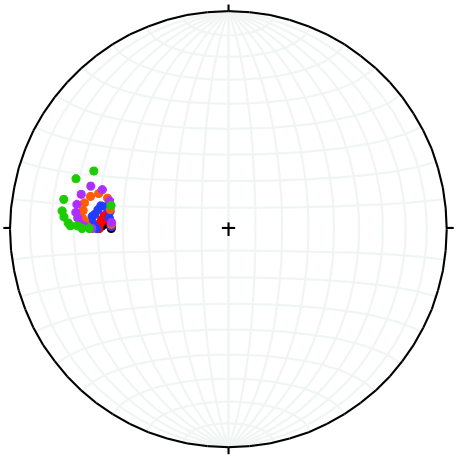

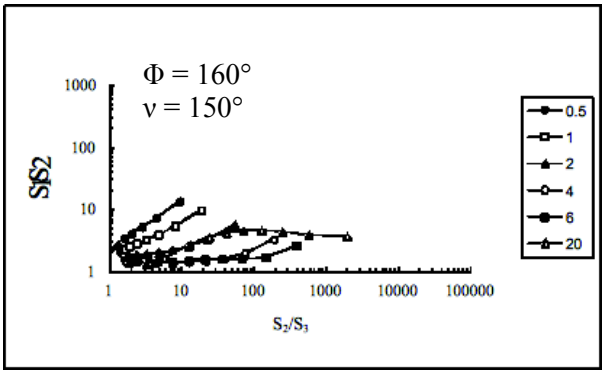
Φ = 160°
ν = 150°
S/S2
1000
100
10
1
1
10
100
1000
10000
100000
S2/S3
0.5
1
2
4
6
20

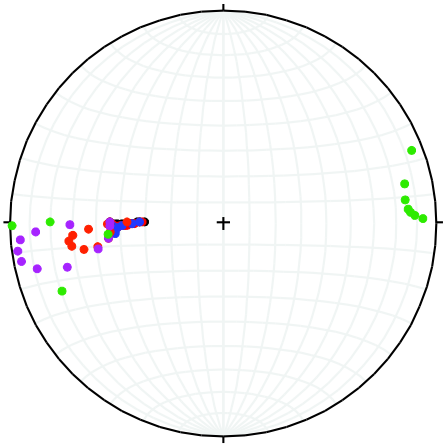

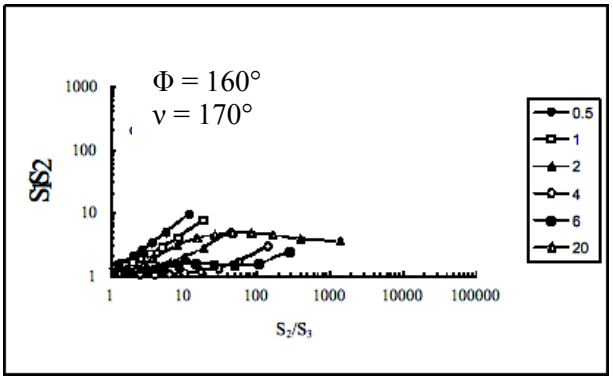
Φ = 160°
ν = 170°
S1/S2
1000
100
10
1
1
10
100
1000
10000
100000
S2/S3
0.5
1
2
4
6
20

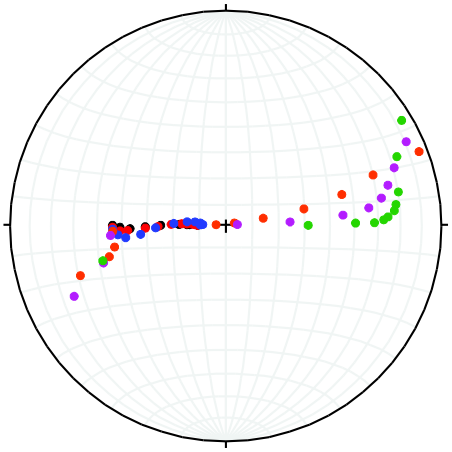

Below are tables showing which parts of each model match the field data. "Lineation refers to the lineation orientation for any point along the overall strain path. "Ellipse" refers to the ratio and orientation of a horizontal ellipse cut through the strain ellipsoid. "Flinn plot" refers to the 3D strain shape. For RBD 13-01, 13-11, and 13-17, matches are listed for different "Runs" which refer to the different combinations of 2D mafic enclave data used to determine a 3D ellipsoid in the Strain3D program. For all other stations in the RBD, no strain data was available, so a red "X" was drawn through the part of the model that was not used for matching. For NEBD locations, the "Lineation," "Ellipse," and "Flinn plot" were similarly matched to the data derived from the folded and boudined veins.

RBD 13-01

Run 1 φ = 20, ν = 170

| $\dot{\gamma}/\dot{\varepsilon}$ | Lineation | Ellipse | Flinn plot |
|---|---|---|---|
| 0.5 | | | |
| 1 | | | |
| 2 | | | |
| 4 | | | |
| 6 | | | |
| 20 | | | |

Run 2 φ = 20, ν = 170

| $\dot{\gamma}/\dot{\varepsilon}$ | Lineation | Ellipse | Flinn plot |
|---|---|---|---|
| 0.5 | | | |
| 1 | | | |
| 2 | | | |
| 4 | | | |
| 6 | | | |
| 20 | | | |

Run 3 φ = 20, ν = 170

| $\dot{\gamma}/\dot{\varepsilon}$ | Lineation | Ellipse | Flinn plot |
|---|---|---|---|
| 0.5 | | | |
| 1 | | | |
| 2 | | | |
| 4 | | | |
| 6 | | | |
| 20 | | | |

Run 4 φ = 20, ν = 170

| $\dot{\gamma}/\dot{\varepsilon}$ | Lineation | Ellipse | Flinn plot |
|---|---|---|---|
| 0.5 | | | |
| 1 | | | |
| 2 | | | |
| 4 | | | |
| 6 | | | |
| 20 | | | |

RBD 13-04

φ = 20, ν = 170

| $\dot{\gamma}/\dot{\varepsilon}$ | Lineation | Ellipse | Flinn plot |
|---|---|---|---|
| 0.5 | | | |
| 1 | | | |
| 2 | | | |
| 4 | | | |
| 6 | | | |
| 20 | | | |

RBD 13-05

φ = 0, ν = 110

| γ̇ / ε̇ | Lineation | Ellipse | Flinn plot |
|---|---|---|---|
| 0.5 | | | |
| 1 | | | |
| 2 | | | |
| 4 | | | |
| 6 | | | |
| 20 | | | |

φ = 0, ν = 130

| γ̇ / ε̇ | Lineation | Ellipse | Flinn plot |
|---|---|---|---|
| 0.5 | | | |
| 1 | | | |
| 2 | | | |
| 4 | | | |
| 6 | | | |
| 20 | | | |

φ = 0, ν = 150

| γ̇ / ε̇ | Lineation | Ellipse | Flinn plot |
|---|---|---|---|
| 0.5 | | | |
| 1 | | | |
| 2 | | | |
| 4 | | | |
| 6 | | | |
| 20 | | | |

φ = 0, ν = 170

| γ̇ / ε̇ | Lineation | Ellipse | Flinn plot |
|---|---|---|---|
| 0.5 | | | |
| 1 | | | |
| 2 | | | |
| 4 | | | |
| 6 | | | |
| 20 | | | |

φ = 20, ν = 0

| γ̇ / ε̇ | Lineation | Ellipse | Flinn plot |
|---|---|---|---|
| 0.5 | | | |
| 1 | | | |
| 2 | | | |
| 4 | | | |
| 6 | | | |
| 20 | | | |

φ = 20, ν = 10

| γ̇ / ε̇ | Lineation | Ellipse | Flinn plot |
|---|---|---|---|
| 0.5 | | | |
| 1 | | | |
| 2 | | | |
| 4 | | | |
| 6 | | | |
| 20 | | | |

φ = 20, ν = 110

| γ̇ / ε̇ | Lineation | Ellipse | Flinn plot |
|---|---|---|---|
| 0.5 | | | |
| 1 | | | |
| 2 | | | |
| 4 | | | |
| 6 | | | |
| 20 | | | |

φ = 20, ν = 130

| γ̇ / ε̇ | Lineation | Ellipse | Flinn plot |
|---|---|---|---|
| 0.5 | | | |
| 1 | | | |
| 2 | | | |
| 4 | | | |
| 6 | | | |
| 20 | | | |

φ = 20, ν = 150

| γ̇ / ε̇ | Lineation | Ellipse | Flinn plot |
|---|---|---|---|
| 0.5 | | | |
| 1 | | | |
| 2 | | | |
| 4 | | | |
| 6 | | | |
| 20 | | | |

φ = 20, ν = 170

| γ̇ / ε̇ | Lineation | Ellipse | Flinn plot |
|---|---|---|---|
| 0.5 | | | |
| 1 | | | |
| 2 | | | |
| 4 | | | |
| 6 | | | |
| 20 | | | |

φ = 160, ν = 0

| $\dot{\gamma}/\dot{\varepsilon}$ | Lineation | Ellipse | Flinn plot |
|---|---|---|---|
| 0.5 | | | |
| 1 | | | |
| 2 | | | |
| 4 | | | |
| 6 | | | |
| 20 | | | |

φ = 160, ν = 10

| $\dot{\gamma}/\dot{\varepsilon}$ | Lineation | Ellipse | Flinn plot |
|---|---|---|---|
| 0.5 | | | |
| 1 | | | |
| 2 | | | |
| 4 | | | |
| 6 | | | |
| 20 | | | |

φ = 160, ν = 30

| $\dot{\gamma}/\dot{\varepsilon}$ | Lineation | Ellipse | Flinn plot |
|---|---|---|---|
| 0.5 | | | |
| 1 | | | |
| 2 | | | |
| 4 | | | |
| 6 | | | |
| 20 | | | |

φ = 160, ν = 50

| $\dot{\gamma}/\dot{\varepsilon}$ | Lineation | Ellipse | Flinn plot |
|---|---|---|---|
| 0.5 | | | |
| 1 | | | |
| 2 | | | |
| 4 | | | |
| 6 | | | |
| 20 | | | |

φ = 160, ν = 70

| $\dot{\gamma}/\dot{\varepsilon}$ | Lineation | Ellipse | Flinn plot |
|---|---|---|---|
| 0.5 | | | |
| 1 | | | |
| 2 | | | |
| 4 | | | |
| 6 | | | |
| 20 | | | |

φ = 160, ν = 170

| $\dot{\gamma}/\dot{\varepsilon}$ | Lineation | Ellipse | Flinn plot |
|---|---|---|---|
| 0.5 | | | |
| 1 | | | |
| 2 | | | |
| 4 | | | |
| 6 | | | |
| 20 | | | |

RBD 13-10

φ = 0, ν = 10

| $\dot{\gamma}$ / $\dot{\varepsilon}$ | Lineation | Ellipse | Flinn plot |
|---|---|---|---|
| 0.5 | | | |
| 1 | | | |
| 2 | | | |
| 4 | | | |
| 6 | | | |
| 20 | | | |

φ = 0, ν = 30

| $\dot{\gamma}$ / $\dot{\varepsilon}$ | Lineation | Ellipse | Flinn plot |
|---|---|---|---|
| 0.5 | | | |
| 1 | | | |
| 2 | | | |
| 4 | | | |
| 6 | | | |
| 20 | | | |

φ = 0, ν = 50

| $\dot{\gamma}$ / $\dot{\varepsilon}$ | Lineation | Ellipse | Flinn plot |
|---|---|---|---|
| 0.5 | | | |
| 1 | | | |
| 2 | | | |
| 4 | | | |
| 6 | | | |
| 20 | | | |

φ = 0, ν = 70

| $\dot{\gamma}$ / $\dot{\varepsilon}$ | Lineation | Ellipse | Flinn plot |
|---|---|---|---|
| 0.5 | | | |
| 1 | | | |
| 2 | | | |
| 4 | | | |
| 6 | | | |
| 20 | | | |

φ = 20, ν = 30

| $\dot{\gamma}$ / $\dot{\varepsilon}$ | Lineation | Ellipse | Flinn plot |
|---|---|---|---|
| 0.5 | | | |
| 1 | | | |
| 2 | | | |
| 4 | | | |
| 6 | | | |
| 20 | | | |

φ = 20, ν = 50

| $\dot{\gamma}$ / $\dot{\varepsilon}$ | Lineation | Ellipse | Flinn plot |
|---|---|---|---|
| 0.5 | | | |
| 1 | | | |
| 2 | | | |
| 4 | | | |
| 6 | | | |
| 20 | | | |

φ = 20, ν = 70

| $\dot{\gamma}$ / $\dot{\varepsilon}$ | Lineation | Ellipse | Flinn plot |
|---|---|---|---|
| 0.5 | | | |
| 1 | | | |
| 2 | | | |
| 4 | | | |
| 6 | | | |
| 20 | | | |

φ = 160, ν = 110

| $\dot{\gamma}$ / $\dot{\varepsilon}$ | Lineation | Ellipse | Flinn plot |
|---|---|---|---|
| 0.5 | | | |
| 1 | | | |
| 2 | | | |
| 4 | | | |
| 6 | | | |
| 20 | | | |

φ = 160, ν = 150

| $\dot{\gamma}$ / $\dot{\varepsilon}$ | Lineation | Ellipse | Flinn plot |
|---|---|---|---|
| 0.5 | | | |
| 1 | | | |
| 2 | | | |
| 4 | | | |
| 6 | | | |
| 20 | | | |

RBD 13-11

Run 1 $\varphi = 20, \nu = 170$

| $\dot{\gamma} / \dot{\varepsilon}$ | Lineation | Ellipse | Flinn plot |
|---|---|---|---|
| 0.5 | | | |
| 1 | | | |
| 2 | | | |
| 4 | | | |
| 6 | | | |
| 20 | | | |

RBD 13-16

φ = 0, ν = 10

| $\dot{\gamma}/\dot{\varepsilon}$ | Lineation | Ellipse | Flinn plot |
|---|---|---|---|
| 0.5 | | | |
| 1 | | | |
| 2 | | | |
| 4 | | | |
| 6 | | | |
| 20 | | | |

φ = 0, ν = 30

| $\dot{\gamma}/\dot{\varepsilon}$ | Lineation | Ellipse | Flinn plot |
|---|---|---|---|
| 0.5 | | | |
| 1 | | | |
| 2 | | | |
| 4 | | | |
| 6 | | | |
| 20 | | | |

φ = 0, ν = 50

| $\dot{\gamma}/\dot{\varepsilon}$ | Lineation | Ellipse | Flinn plot |
|---|---|---|---|
| 0.5 | | | |
| 1 | | | |
| 2 | | | |
| 4 | | | |
| 6 | | | |
| 20 | | | |

φ = 0, ν = 70

| $\dot{\gamma}/\dot{\varepsilon}$ | Lineation | Ellipse | Flinn plot |
|---|---|---|---|
| 0.5 | | | |
| 1 | | | |
| 2 | | | |
| 4 | | | |
| 6 | | | |
| 20 | | | |

φ = 20, ν = 10

| $\dot{\gamma}/\dot{\varepsilon}$ | Lineation | Ellipse | Flinn plot |
|---|---|---|---|
| 0.5 | | | |
| 1 | | | |
| 2 | | | |
| 4 | | | |
| 6 | | | |
| 20 | | | |

φ = 20, ν = 30

| $\dot{\gamma}/\dot{\varepsilon}$ | Lineation | Ellipse | Flinn plot |
|---|---|---|---|
| 0.5 | | | |
| 1 | | | |
| 2 | | | |
| 4 | | | |
| 6 | | | |
| 20 | | | |

φ = 20, ν = 50

| $\dot{\gamma}/\dot{\varepsilon}$ | Lineation | Ellipse | Flinn plot |
|---|---|---|---|
| 0.5 | | | |
| 1 | | | |
| 2 | | | |
| 4 | | | |
| 6 | | | |
| 20 | | | |

φ = 20, ν = 70

| $\dot{\gamma}/\dot{\varepsilon}$ | Lineation | Ellipse | Flinn plot |
|---|---|---|---|
| 0.5 | | | |
| 1 | | | |
| 2 | | | |
| 4 | | | |
| 6 | | | |
| 20 | | | |

φ = 160, ν = 110

| $\dot{\gamma}/\dot{\varepsilon}$ | Lineation | Ellipse | Flinn plot |
|---|---|---|---|
| 0.5 | | | |
| 1 | | | |
| 2 | | | |
| 4 | | | |
| 6 | | | |
| 20 | | | |

φ = 160, ν = 150

| $\dot{\gamma}/\dot{\varepsilon}$ | Lineation | Ellipse | Flinn plot |
|---|---|---|---|
| 0.5 | | | |
| 1 | | | |
| 2 | | | |
| 4 | | | |
| 6 | | | |
| 20 | | | |

φ = 160, ν = 170

| $\dot{\gamma}$ / $\dot{\varepsilon}$ | Lineation | Ellipse | Flinn plot |
|---|---|---|---|
| 0.5 | | | |
| 1 | | | |
| 2 | | | |
| 4 | | | |
| 6 | | | |
| 20 | | | |

RBD 13-17

Run 1 φ = 20, ν = 170

| $\dot{\gamma}$ / $\dot{\varepsilon}$ | Lineation | Ellipse | Flinn plot |
|---|---|---|---|
| 0.5 | | | |
| 1 | | | |
| 2 | | | |
| 4 | | | |
| 6 | | | |
| 20 | | | |

Run 2

| $\dot{\gamma}$ / $\dot{\varepsilon}$ | Lineation | Ellipse | Flinn plot |
|---|---|---|---|
| 0.5 | | | |
| 1 | | | |
| 2 | | | |
| 4 | | | |
| 6 | | | |
| 20 | | | |

RBD 13-20

φ = 160, ν = 10

| $\dot{\gamma}$ / $\dot{\varepsilon}$ | Lineation | Ellipse | Flinn plot |
|---|---|---|---|
| 0.5 | | | |
| 1 | | | |
| 2 | | | |
| 4 | | | |
| 6 | | | |
| 20 | | | |

φ = 160, ν = 90

| $\dot{\gamma}$ / $\dot{\varepsilon}$ | Lineation | Ellipse | Flinn plot |
|---|---|---|---|
| 0.5 | | | |
| 1 | | | |
| 2 | | | |
| 4 | | | |
| 6 | | | |
| 20 | | | |

φ = 20, ν = 90

| $\dot{\gamma}$ / $\dot{\varepsilon}$ | Lineation | Ellipse | Flinn plot |
|---|---|---|---|
| 0.5 | | | |
| 1 | | | |
| 2 | | | |
| 4 | | | |
| 6 | | | |
| 20 | | | |

NEBD 13-01

φ = 0, ν = 10

| $\dot{\gamma}/\dot{\varepsilon}$ | Lineation | Ellipse | Flinn plot |
|---|---|---|---|
| 0.5 | | | |
| 1 | | | |
| 2 | | | |
| 4 | | | |
| 6 | | | |
| 20 | | | |

φ = 0, ν = 170

| $\dot{\gamma}/\dot{\varepsilon}$ | Lineation | Ellipse | Flinn plot |
|---|---|---|---|
| 0.5 | | | |
| 1 | | | |
| 2 | | | |
| 4 | | | |
| 6 | | | |
| 20 | | | |

φ = 20, ν = 0

| $\dot{\gamma}/\dot{\varepsilon}$ | Lineation | Ellipse | Flinn plot |
|---|---|---|---|
| 0.5 | | | |
| 1 | | | |
| 2 | | | |
| 4 | | | |
| 6 | | | |
| 20 | | | |

φ = 20, ν = 10

| $\dot{\gamma}/\dot{\varepsilon}$ | Lineation | Ellipse | Flinn plot |
|---|---|---|---|
| 0.5 | | | |
| 1 | | | |
| 2 | | | |
| 4 | | | |
| 6 | | | |
| 20 | | | |

φ = 20, ν = 170

| $\dot{\gamma}/\dot{\varepsilon}$ | Lineation | Ellipse | Flinn plot |
|---|---|---|---|
| 0.5 | | | |
| 1 | | | |
| 2 | | | |
| 4 | | | |
| 6 | | | |
| 20 | | | |

φ = 160, ν = 0

| $\dot{\gamma}/\dot{\varepsilon}$ | Lineation | Ellipse | Flinn plot |
|---|---|---|---|
| 0.5 | | | |
| 1 | | | |
| 2 | | | |
| 4 | | | |
| 6 | | | |
| 20 | | | |

φ = 160, ν = 10

| $\dot{\gamma}/\dot{\varepsilon}$ | Lineation | Ellipse | Flinn plot |
|---|---|---|---|
| 0.5 | | | |
| 1 | | | |
| 2 | | | |
| 4 | | | |
| 6 | | | |
| 20 | | | |

Φ = 160, ν = 170

| $\dot{\gamma}/\dot{\varepsilon}$ | Lineation | Ellipse | Flinn plot |
|---|---|---|---|
| 0.5 | | | |
| 1 | | | |
| 2 | | | |
| 4 | | | |
| 6 | | | |
| 20 | | | |

NEBD 13-02

φ = 0, ν = 10

| $\dot{\gamma}/\dot{\varepsilon}$ | Lineation | Ellipse | Flinn plot |
|---|---|---|---|
| 0.5 | | | |
| 1 | | | |
| 2 | | | |
| 4 | | | |
| 6 | | | |
| 20 | | | |

φ = 0, ν = 170

| $\dot{\gamma}/\dot{\varepsilon}$ | Lineation | Ellipse | Flinn plot |
|---|---|---|---|
| 0.5 | | | |
| 1 | | | |
| 2 | | | |
| 4 | | | |
| 6 | | | |
| 20 | | | |

φ = 20, ν = 0

| $\dot{\gamma}/\dot{\varepsilon}$ | Lineation | Ellipse | Flinn plot |
|---|---|---|---|
| 0.5 | | | |
| 1 | | | |
| 2 | | | |
| 4 | | | |
| 6 | | | |
| 20 | | | |

φ = 20, ν = 10

| $\dot{\gamma}/\dot{\varepsilon}$ | Lineation | Ellipse | Flinn plot |
|---|---|---|---|
| 0.5 | | | |
| 1 | | | |
| 2 | | | |
| 4 | | | |
| 6 | | | |
| 20 | | | |

φ = 20, ν = 170

| $\dot{\gamma}/\dot{\varepsilon}$ | Lineation | Ellipse | Flinn plot |
|---|---|---|---|
| 0.5 | | | |
| 1 | | | |
| 2 | | | |
| 4 | | | |
| 6 | | | |
| 20 | | | |

φ = 160, ν = 0

| $\dot{\gamma}/\dot{\varepsilon}$ | Lineation | Ellipse | Flinn plot |
|---|---|---|---|
| 0.5 | | | |
| 1 | | | |
| 2 | | | |
| 4 | | | |
| 6 | | | |
| 20 | | | |

φ = 160, ν = 10

| $\dot{\gamma}/\dot{\varepsilon}$ | Lineation | Ellipse | Flinn plot |
|---|---|---|---|
| 0.5 | | | |
| 1 | | | |
| 2 | | | |
| 4 | | | |
| 6 | | | |
| 20 | | | |

Φ = 160, ν = 170

| $\dot{\gamma}/\dot{\varepsilon}$ | Lineation | Ellipse | Flinn plot |
|---|---|---|---|
| 0.5 | | | |
| 1 | | | |
| 2 | | | |
| 4 | | | |
| 6 | | | |
| 20 | | | |